Abstract of "**Recursive Auxiliary Field Quantum Monte Carlo: From Simulations in the Canonical Ensemble to Entanglement Measures**" by Tong Shen, Ph.D., Brown University, October 2023.

The complicated ways in which electrons interact in many-body systems such as most molecules and materials have long been studied without accounting for the effects of conservation laws. Resolving symmetries associated with these conservation laws can not only provide complementary and clarifying lens on electronic behavior but is also sometimes essential for obtaining correct results. In this thesis, I present studies that perform symmetry resolution in many-body simulations for two different contexts: i) finite temperature electronic structure calculations, and ii) zero temperature entanglement measures.

In Part I, I introduce a recursive Auxiliary Field Quantum Monte Carlo (AFQMC) algorithm that can directly simulate systems in the canonical ensemble. We apply the method to the fermion Hubbard model and find improved performance over existing approaches including rapid convergence to ground state expectation values. The effects of excitations above the ground state are quantified using an estimator-agnostic approach including studying the temperature dependence of the purity and overlap fidelity of the canonical and grand canonical density matrices. As an important application, we show that thermometry approaches often exploited in ultra-cold atoms that employ the analysis in the grand canonical ensemble may lead to an under-estimation of extracted temperatures with respect to the Fermi temperature.

In Part II, I combine the recursive AFQMC with a modified swap algorithm to measure the accessible entanglement, the entanglement available to a system subject to fixed particle number due to superselection rules, for strongly interacting fermion systems for the first time. The combined algorithm is applied to characterize the phase transitions in the bilayer Hubbard model and the Su–Schrieffer–Heeger-Hubbard model. Here, we utilize

these entanglement measures alongside the corresponding particle and spin probability distributions and demonstrate that these quantum informational metrics more clearly resolve around the phase transitions and crossovers than the unresolved entanglement entropy and even certain local order parameters. Overall, this thesis provides new means of characterizing the electronic behavior within quantum systems, potentially deepening our comprehension of the intricate interplay between many-body correlations and conservation laws that underlie quantum phase transitions and crossovers.

Recursive Auxiliary Field Quantum Monte Carlo: From Simulations in the Canonical Ensemble to Entanglement Measures

by

Tong Shen

B.S., Materials Physics, University of Science and Technology of China, 2018

Sc.M., Applied Mathematics, Brown University, 2020

A dissertation submitted in partial fulfillment of the requirements for the Degree of Doctor of Philosophy in the Department of Chemistry at Brown University

Providence, Rhode Island

October 2023

This dissertation by Tong Shen is accepted in its present form by the Department of Chemistry as satisfying the dissertation requirement for the degree of Doctor of Philosophy.

Date _____ _____

Brenda M. Rubenstein, Advisor

Recommended to the Graduate Council

Date _____ _____

Richard M. Stratt, Reader

Date _____ _____

John B. Marston, Reader

Approved by the Graduate Council

Date _____ _____

Thomas A. Lewis, Dean of the Graduate School

Curriculum Vitae

Education

2018–2023 Ph.D., Chemistry
Brown University (Providence, RI, USA)

2019-2021
M.Sc., Applied Mathematics
Brown University (Providence, RI, USA)

2014–2018
B.Sc., Materials Physics
University of Science and Technology of China (Hefei, Anhui, China)

Awards

- Open Graduate Fellowship, Brown University Graduate School
- Lenovo Poster Award, International Conference on Recent Progress in Many-Body Theories XXI

Publications

in preparation

- **Tong Shen**, Hatem Barghathi, Adrian del Maestro, Brenda M. Rubenstein, Auxiliary Field Quantum Monte Carlo Algorithm for Operationally Accessible Entanglement of Lattice Fermions, in preparation (2023)

peer-reviewed

- **Tong Shen**, Jiangyong Yu, Hatem Barghathi, Adrian del Maestro, Brenda M. Rubenstein, A Stable, Recursive Auxiliary Field Quantum Monte Carlo Algorithm in the Canonical Ensemble: Applications to Thermometry and the Hubbard Model, *Physical Review E*, 107,055302 (2023)
- **Tong Shen**, Yuan Liu, Yang Yu, Brenda M. Rubenstein, Finite Temperature Auxiliary Field Quantum Monte Carlo in the Canonical Ensemble, *The Journal of Chemical Physics*, 153, 204108 (2020)
- Yuan Liu, **Tong Shen**, Hang Zhang, Brenda Rubenstein, Unveiling the Finite Temperature Physics of Hydrogen Chains via Auxiliary Field Quantum Monte Carlo, *Journal of Chemical Theory and Computation*, 16, 7, 4298-4314, (2020)

Preface

Within the broad spectrum of modern physical sciences, two principal branches stand out to deal with phenomena occurring at the quantum mechanical level (microscopic, low-temperature, low-dimensional), namely, quantum chemistry and condensed matter physics. On one hand, the objectives and priorities of these two fields diverge: quantum chemists prioritize resolving the electronic structure of molecules with exceptionally high precision to describe and predict chemical phenomena, while condensed matter physicists focus more on studying solids and reduced model systems to discern the macroscopic properties of matter from its quantum states at the microscopic level, rather than aiming for atomic-level precision. On the other hand, they converge at the methodological level, as both of them aim to solve the Schrödinger equation in a simple yet generalizable manner, such that simulations can be performed on a wide range of systems within a realistic amount of time. Nevertheless, having discussed with many experts from both areas, it is clear to me that although the boundary between these two disciplines is quite fluid, researchers from one field are often times indifferent to the other field. Despite their substantial overlap in theory and application, the insights and interpretations are often found to come from a singular perspective rather than a fusion of both. Studying the intersection of perspectives between quantum chemistry and condensed matter physics thus underpins my primary research interest as a theorist.

The core focus of my research is the study of *symmetry* at this intersection. Although it is generally true that symmetry can help reduce the analytical and computational

effort required to solve quantum mechanical problems, it turns out that enforcing a certain symmetry on a system can be more computationally challenging than releasing it. Nonetheless, conservation laws and selection rules stemming from symmetry play a pivotal role in shaping our understanding of molecules and solids. This encompasses their structural, electronic, and spectroscopic properties, as well as the phases and phase transitions that connect them. Understanding how a specific symmetry influences these properties is therefore vital in both quantum chemistry and condensed matter physics. This underscores the need for innovative methods that enable imposing symmetries to solve quantum mechanical problems without drastically increasing the computational cost. In this regard, I developed a novel Recursive Auxiliary Field Quantum Monte Carlo method for efficiently performing finite temperature simulations in the canonical ensemble, which necessitates imposing particle number conservation (U(1) symmetry) [T. Shen *et al.* J. Chem. Phys. (2020)]. I then improved the stability of this method and applied it to study the thermometry of cold atom systems using the Hubbard model as an example [T. Shen *et al.* Phys. Rev. E (2023)]. Furthermore, I generalized this method to enable charge and spin resolution of the entanglement measures for a system under charge and spin conservation [T. Shen *et al.* in preparation (2023)].

In this thesis, I introduce my novel algorithm for finite-temperature simulations in the canonical ensemble, alongside an exploration of entanglement measures in the ground state. These two points illustrate the interplay between many-body interactions and conservation laws (symmetry) from the quantum mechanical and quantum information perspectives, respectively.

Tong Shen

Providence, Rhode Island

Acknowledgments

I would like to begin by expressing my deepest gratitude to my advisor, Prof. Brenda Rubenstein. Choosing to apply to Brown and subsequently working with Brenda is among the best decisions I made so far. I am truly grateful for the opportunity to learn her scientific philosophy and contribute to her research. I would like to thank Brenda for teaching me how to be an independent scientist and how to assess research ideas. I also want to thank Brenda for giving me exceptional freedom to explore various problems across multiple disciplines at the early stage of my Ph.D. This experience introduced me to a diverse scientific community and steered me towards research topics that truly resonate with me. Despite the demands of leading a large interdisciplinary research team, Brenda has always been accessible for project and scientific discussions. I must thank Brenda once again for giving me invaluable career advice throughout my Ph.D. journey.

I am also grateful to my committee members, Prof. Richard Stratt and Prof. Brad Marston. I truly appreciate Prof. Stratt's invaluable insights and constructive feedback on my Ph.D. milestones. Anticipating his questions during my preparations for presentations significantly improved the quality of my work. I also enjoyed his questions in every seminar and gained a deep respect for his scientific perspective during our discussions over the course of my Ph.D. I am grateful to Prof. Brad Marston for his outstanding theoretical mechanics class, which is easily the best I have taken at Brown. I also value the insights and suggestions he offered during our conversations. Similarly, my thanks go to Prof. Kavita Ramanan. Her passion for teaching was captivating, and it facilitated my

integration into math classes, despite being the only non-math student for three straight semesters. Besides, her unique mathematician's view on various physical problems has significantly inspired me. I want to thank Prof. Sarah Delaney and Prof. Jerome Robinson for their advice and help. Moreover, I am grateful to Prof. Dean Lee, Prof. Shiwei Zhang, Prof. Garnet Chan and Dr. Scott Jensen for comments and suggestions on my research work.

I must thank Dr. Yuan Liu for always being approachable whenever I needed his help in learning QMC and seeking research advice in my junior years. His patience in addressing my numerous questions was instrumental in my understanding of the QMC code. I am also grateful for his career insights and recommendations. I extend my best wishes to him as he embarks on his independent career at NCSU. I furthermore want to acknowledge the whole Rubenstein group. I am grateful to Dr. Hongxia Hao, Dr. Ravindra Nanguneri, Dr. Matthew Church, and Dr. Eshan Barati for their helpful discussions. I would like to extend my heartfelt thanks to the staff of the Brown Chemistry department for their dedication. I am also grateful to the Graduate School for their financial support through the Open Graduate Fellowship and to the Center for Computation and Visualization for providing computing resources and assistance.

I would like to express my gratitude to my collaborators, Prof. Adrian del Maestro and Dr. Hatem Barghathi. Engaging in discussions with Adrian on physics and computer science has been enlightening, and I have gained immensely from his insights. I am thankful for the warm hospitality he generously offered during my two-week stay at UTK; our collaboration during this period was incredibly productive. I am fortunate to collaborate with Hatem. His expertise in quantum information has been invaluable, and I have learned a great deal from him. I deeply appreciate his consistent availability and willingness to assist whenever I encountered challenges. Additionally, my thanks go to Dr. Benjamin Cohen-Stead for his invaluable advice on QMC coding. His Julia packages have been instrumental in shaping my QMC code. Lastly, I am grateful to Dr. Jonathan

d'Emidio for his generous assistance and guidance regarding the entanglement code.

I would like to express my gratitude to those in Providence who supported me throughout my Ph.D. journey at Brown. Special thanks to Dawei Si, Darryl (Xiaoyu) Xie, Tianmin Yu and Xiaozhou Fan, my best friends, for their unwavering support. The moments we shared have been invaluable. Dawei's expertise in coding with Julia was indispensable; his assistance accelerated my understanding of scientific programming. I am also appreciative of Darryl and Tianmin's guidance in math.

Lastly, my deepest gratitude goes to my family for their unwavering support and patience. Words cannot capture the depth of my appreciation for my parents' unconditional love and encouragement throughout my academic journey.

To my parents

Contents

List of Figures

List of Tables

Part I

Recursive Auxiliary Field Quantum Monte Carlo for Finite Temperature Simulations in the Canonical Ensemble

CHAPTER 1

Introduction

1.1 Quantum Statistical Mechanics

For decades, chemical physicists have focused on developing a constellation of electronic structure methods, from mean field[1, 2] to perturbation[1, 2] to coupled cluster theories,[2, 3] to describe the ground and low-lying excited states of molecules and solids. While it is undoubtedly true that many phenomena involve electrons that reside in their ground states, it is becoming increasingly apparent that there are a wealth of phenomena for which this assumption does not hold: atoms and molecules in the centers of large planets and stars can experience GPa of pressure and temperatures of over 10,000 K[4, 5], and lasers can be used to heat and thereby steer chemical reactions along different mechanistic pathways to facilitate processes such as catalysis[6, 7, 8]. Furthermore, the thermal distribution of electrons competes with their quantum correlations, playing a crucial role in determining finite temperature phase transitions, including structural[9], metal-insulator[10], superconducting[11], and magnetic[12] transitions. Temperature is moreover one of the key parameters that can be used to tune the electronic properties of the materials that make up many of modern society's most important technologies[10, 13, 14] and is responsible for the pernicious loss of coherence in physical realizations of qubits[15].

Studying the properties of electrons at finite temperature necessitates using concepts and methodologies from quantum statistical mechanics. While classical statistical mechanics provides a good approximation for macroscopic systems where quantum effects are negligible often at high temperatures, quantum statistical mechanics is essential for accurately describing the behavior of systems at the microscopic level and at low temperatures. The key differences between the classical and the quantum description can be revealed by examining the most important quantity in statistical mechanics, the partition function. In classical mechanics, the state of a system is described by points in phase space, with each point representing a possible state of the system given by a particular set of position and momentum coordinates for each particle. Classical statistical mechanics also assumes that energy levels are continuous, and a system can take any energy values within a given range. As such, the partition function of an N-particle system is given as

$$Z_N = \int d\Gamma e^{-\beta E_N(\Gamma)}, \tag{1.1}$$

where E_N is the energy of a microstate of the system, $\beta = 1/k_B T$ is the inverse temperature and k_B is the Boltzmann constant, and $\Gamma = (\vec{p}, \vec{q})$ represents a point in the phase space with canonical position and momentum vectors $\vec{p}$ and $\vec{q}$, respectively. The integral is taken over all possible microstates in the phase space.

Quantum statistical mechanics, however, uses a different state space, namely, the Hilbert space, where states are represented as vectors whose evolutions are governed by the Schrödinger equation. Particles in quantum statistical mechanics can be either distinguishable (Boltzmannons) or indistinguishable (fermions or bosons), which significantly changes the statistical properties of a system (Fermi-Dirac or Bose-Einstein statistics). Energy levels are quantized and can only take certain discrete values. The partition function is therefore defined differently to reflect the quantum nature of the states, particles, and energy levels:

$$Z_N = \mathrm{tr}_N[e^{-\beta \hat{H}}], \tag{1.2}$$

where tr_N represents the trace over the N-particle Hilbert space, $\mathcal{H}_N$, and $\hat{H}$ is the Hamiltonian operator that can be represented by a matrix expanded in $\mathcal{H}_N$ (hence the exponential above is a matrix exponential).

While the partition functions are defined differently in classical and quantum contexts, they are connected to various important observables of a physical system in the same manner. To list a few, the expectation value of the energy of the system can be derived from the partition function as

$$\langle E \rangle = -\frac{\partial \ln Z_N}{\partial \beta}, \tag{1.3}$$

and the free energy and entropy can be obtained by

$$F = -k_B T \ln Z_N, \tag{1.4}$$

$$S = -\frac{\partial F}{\partial T}. \tag{1.5}$$

More general quantities like the correlation functions between two physical quantities (operators) A and B ($\hat{A}$ and $\hat{B}$) can be formulated in terms of partition functions as[16, 17]

$$\langle A(t)B(0)\rangle = \int d\Gamma A(t)B(0)p(\Gamma), \text{ with } p(\Gamma) = \frac{e^{-\beta E(\Gamma)}}{Z_N}, \tag{1.6}$$

and

$$\left\langle \hat{A}(t)\hat{B}(0)\right\rangle = \mathrm{tr}_N(\hat{A}(t)\hat{B}(0)\rho), \text{ with } \rho = \frac{e^{-\beta \hat{H}}}{Z_N}, \tag{1.7}$$

in the classical and quantum cases, respectively. Here, $p(\Gamma)$ is the canonical probability distribution and ρ is the density matrix. With these equations, the partition function provides connections between the microscopic (like energy levels) and macroscopic properties (like temperature and pressure) of a system.

It is important to note that the above formulas are given for the canonical ensemble where the particle number is fixed. One can work in the grand canonical ensemble by coupling the system to a particle reservoir. Then, the particle number is allowed to

fluctuate, which results in a modification of Equation 1.2 to

$$\mathcal{Z}_\mu = \mathrm{tr}\Big[e^{-\beta(\hat{H}-\mu\hat{N})}\Big]. \tag{1.8}$$

Here, μ is the chemical potential, $\hat{N}$ is the number operator, and the trace is now taken over the whole Fock space, $\mathcal{F} = \oplus_N \mathcal{H}_N$. Thermodynamic relations, namely Eqs.(1.3)-(1.7), hold in the grand canonical ensemble when Z_N is replaced by $\mathcal{Z}_\mu$, but these equations could yield significantly different results in different ensembles. Indeed, investigating such differences due to the choice of ensembles forms a key theme in Part I of this thesis. For the remainder of the thesis, we use Z to denote the partition function in general scenarios where the working ensemble does not need to be specified.

Path Integral Formulation of the Partition Function

Since the partition function is the most fundamental quantity in finite temperature many-body physics, one needs a way of computing it. One direct strategy for quantum partition functions involves diagonalizing the matrix corresponding to the Hamiltonian operator to obtain all energy levels, after which the Boltzmann factors of these energy eigenvalues are summed, yielding $Z = \sum_\lambda e^{-\beta E_\lambda}$, where E_λ denotes the energy of the λth eigenstate (assuming non-degenerate energy levels). This method, while exact, is limited to small systems due to the exponential growth of the Hilbert space, and thus the matrix to be diagonalized, with increasing system size and particle number.

The path integral formulation of the partition function, put forward by Mastubara[18] based on the initial idea from Feymann[19], offers a powerful tool for addressing the above problem. It expresses the partition function in terms of imaginary-time evolutions along classical paths. The key idea is to view the Boltzmann operator as a time evolution operator in imaginary time

$$\rho \propto e^{-\beta\hat{H}} = U(-i\hbar\beta), \tag{1.9}$$

where $U(t) = e^{-i\hat{H}t/\hbar}$ is the real-time evolution operator at zero temperature. A substitution, $\frac{it}{\hbar} \to \tau$, is made such that the time-dependent Schrödinger equation

$$i\hbar\frac{\partial}{\partial t}|\psi\rangle = \hat{H}|\psi\rangle \tag{1.10}$$

becomes

$$-\frac{\partial}{\partial \tau}|\psi\rangle = \hat{H}|\psi\rangle \tag{1.11}$$

whose solution is exactly Eq.(1.9) over the interval from $\tau = 0$ to $\tau = \beta$[1]. With this single substitution, one can generalize almost everything in zero-temperature quantum mechanics into finite-temperature quantum statistical mechanics[20]. The difference is the real-time evolution is unbounded and can be carried out in a space that extends infinitely from $t = -\infty$ to $t = \infty$, while the imaginary time evolution at finite temperature is confined to a finite interval $[0, \beta]$.

Using this notion, the partition function can be reformulated as a path integral in terms of a set of basis $|x\rangle$[2]

$$Z = \int \mathcal{D}[\mathbf{x}(\tau)] e^{-\mathcal{T}\int_0^\beta d\tau H[\mathbf{x}(\tau)]} \tag{1.12}$$

Here, $\mathcal{T}$ is the time ordering and $\mathcal{D}[\mathbf{x}(\tau)]$ denotes the path integral measure over all possible paths $\mathbf{x}(\tau)$ the system can take in the imaginary time τ. For an infinitesimal interval $\Delta\tau$, the integrand is the matrix element of the exponentiated Hamiltonian:

$$e^{-\Delta\tau H[\mathbf{x}(\tau+\Delta\tau)]} = \langle x_\tau | e^{-\Delta\tau\hat{H}} | x_{\tau+\Delta\tau}\rangle. \tag{1.13}$$

An integration from $\tau = 0$ to $\tau = \beta$ thus specifies a path in the state space spanned by $|x\rangle$: $\{x_0, x_{\Delta\tau}, \ldots, x_{\beta-\Delta\tau}, x_0\}$. Note that the starting and ending points of any path must

[1] $\hbar = 1$ is assumed in the thesis.

[2] The choice of such a basis is arbitrary; it may be represented in real space coordinates or in abstract spaces such as Slater determinant space or auxiliary-field space.

be the same as enforced by the trace operation.

The path integral formulation provides a bridge between classical and quantum statistical mechanics, making it possible to employ powerful methods from the former to solve problems in the latter. This concept has served as a cornerstone for the development of a plethora of finite temperature electronic structure theories. In the context of quantum Monte Carlo, the integrand of Eq.(1.12), $e^{-\mathcal{T}\int_0^\beta d\tau H[\mathbf{x}(\tau)]}$, can be viewed as statistical weights, thereby allowing a Monte Carlo integration to numerically evaluate the path integral. Different choices for the basis $|x\rangle$ result in different flavors of Monte Carlo algorithms, with real space corresponding to Path Integral Monte Carlo and auxiliary-field space corresponding to Auxiliary Field Quantum Monte Carlo.

1.2 Finite Temperature Electronic Structure Theories

1.2.1 Deterministic and Stochastic Methods

Reflecting the growing list of applications at finite temperature, there has been a recent surge in the development of methods to study them. One of the most straightforward ways of determining the finite temperature properties of quantum systems is by diagonalizing the system's Hamiltonian to determine all of its many eigenvalues and weighting them to compute its partition function and related observables in a process termed exact diagonalization (ED)[21]. While this technique is numerically exact, as its name implies, its computational cost scales exponentially with system size. On the other end of the spectrum, finite temperature mean field theories, including finite temperature Hartree Fock[22, 23] and Density Functional (DFT) theories,[24, 25] trade accuracy for computational expediency by approximating the many-body problem as a one-body problem in which an electron is coupled to an average or "mean" field of the other electrons. While such mean field theories continue to improve and hold great promise, they still struggle to achieve the

accuracy often needed to correctly capture many-body physics. Between these two poles lie a variety of techniques that are generalizations of their ground state counterparts. The past few years, for example, have seen a resurgence of interest in finite temperature coupled cluster techniques[26, 27, 28, 29, 30] and perturbation theories.[31, 32, 33, 34, 35, 36] Closer to the mean field end of the spectrum, finite temperature embedding theories that partition systems into correlated regions embedded within uncorrelated baths[37] such as Dynamical Mean Field Theory (DMFT)[38, 39] and the finite temperature SEET and GF2 methods[40, 41, 42] are distinctively capable of directly obtaining the full frequency-dependent spectra of the systems they model. Nevertheless, all of these methods struggle to balance computational cost with the need to account for the numerous electronic states that contribute to finite temperature expectation values.

Finite temperature Quantum Monte Carlo (FT-QMC) methods are particularly advantageous in this regard because they have the exceptional ability to access numerous states without the exponential or high polynomial costs of other techniques by randomly sampling multidimensional state spaces for the most important states.[43, 44, 45, 46] One of the most successful of these techniques is Determinant Quantum Monte Carlo (DQMC)[47, 48, 49] and its more recent extension, FT Auxiliary Field Quantum Monte Carlo (FT-AFQMC)[50, 51, 52]. DQMC has a long history of being employed to study a wide variety of lattice models. One of the key reasons why DQMC has been so widely adopted is because, for certain important classes of problems[47, 53], it does not suffer from the infamous sign or phase problems[54] that limit the practical utility of many other stochastic methods. AFQMC methods grew out of DQMC methods and were developed with the aim of being able to accurately model systems with clear sign problems by leveraging its more sophisticated sampling techniques and phaseless approximation.[46, 55, 56, 57] These methods have since shed light on such sign- and phaseful systems as the Hubbard model off of half-filling[54, 58, 59] and many different *ab initio* molecular[52, 60, 61, 62] and solid state systems[63, 64, 65, 66]. Furthermore, these QMC techniques are versatile –

they can be applied to virtually any second-quantized Hamiltonian – and, by sampling the overcomplete space of non-orthogonal determinants, they are able to sample large portions of Fock space with high accuracy, yet comparatively mild computational cost of $\mathcal{O}(N_s^3)$-$\mathcal{O}(N_s^4)$, where N_s denotes the number of basis functions[46].

1.2.2 The Need to Fix the Particle Number

This said, one of the Janus-faced features of the methods introduced above is that they are formulated in the grand canonical ensemble, in which a system's internal energy and particle number are allowed to fluctuate according to its fixed temperature and chemical potential[67]. In many systems, the grand canonical ensemble is the ensemble of choice for modeling systems at finite temperature. This is a natural framework due to the approach to the thermodynamic limit for electrons in solids, or the existence of a particle (or quasi-particle) reservoir in transport geometries, heterostructures, and superconductors. Having a fluctuating particle number is moreover beneficial from the numerical perspecitve, as it enables one to trace over the particle number degrees of freedom, leaving an average particle number that is tunable with a Lagrangian multiplier identified with the chemical potential, μ. Any particle filling can in principle be achieved by selecting an appropriate μ, thereby eliminating the need to explicitly account for the particle number distribution for each microstate.

However, there are a growing number of important scenarios in which the number of particles is fixed and small, including trapped atom systems comprised of a finite number of atoms confined in box-style traps[68, 69, 70], nuclear systems with a fixed number of nucleons[71], and molecules containing a fixed number of electrons[52, 72]. All such systems are more accurately described by the canonical ensemble in which the number of particles cannot fluctuate. Moreover, many ground state algorithms in condensed matter are formulated in the canonical ensemble[73, 74, 75, 56] and finite temperature algorithms that can converge to these algorithms' ground state results

without spurious particle number fluctuations can shed a brighter light on the mechanisms behind low-temperature quantum phase transitions and crossovers[72, 63]. Other examples where systems need to be treated within the canonical ensemble include determining the operationally-accessible entanglement in indistinguishable many-body systems in the presence of a $U(1)$ superselection rule limiting physically-allowable operations[76, 77, 78] and the determination of thermonuclear rates for astrophysics[79].

Even from the simulation standpoint, sampling in the GCE may not be efficient as the process of pinpointing the correct chemical potential to reach a desired particle filling can be cumbersome. In current auxiliary field techniques that work in the grand canonical ensemble, practitioners are often required to scan through tens to hundreds of potential chemical potentials in order to identify the appropriate one for each Hamiltonian under study[52, 80]. This procedure can be both time-consuming and resource-intensive.

Thus, efficiently describing interacting systems in the canonical ensemble has nevertheless been a longstanding challenge, particularly for second-quantized algorithms. Unlike in the grand canonical ensemble, in which partition functions and other quantities can be evaluated without placing any constraints on the number of particles[67], evaluating quantities in the canonical ensemble requires an explicit consideration of particle-number constraints. At a physical level, these constraints give rise to interesting, nontrivial correlations among the occupations of different states – higher order expectation values of occupation numbers do not factorize, even in the non-interacting limit[81]. However, at a numerical level, these constraints can make the analytical and computational evaluation of canonical ensemble quantities substantially more cumbersome[82].

1.2.3 Modeling Finite Temperature Physics in the Canonical Ensemble

One approach for modeling interacting systems in the canonical ensemble that circumvents the imposition of direct constraints is the use of projection techniques[83, 84].

In these algorithms, canonical ensemble quantities are projected out from the grand canonical partition function at a suitably tuned chemical potential[85]. This approach has been fruitfully employed to study a wide variety of problems in nuclear physics[83, 86], and more recently, condensates[87, 88]. Nonetheless, because this algorithm relies upon projecting out of the grand canonical ensemble, it is accompanied by the same computational overhead as typical finite temperature grand canonical simulations and can develop numerical instabilities for large particle numbers or when reasonable chemical potentials cannot be identified, for example near first order phase transitions[89]. Recently, techniques for rapidly determining a chemical potential where it can be readily identified have been proposed, but these techniques still do not inherently operate in the canonical ensemble[85, 90, 91]. Approaches that directly take physical constraints into account therefore have the potential to lead to methods that are not only more stable, but also more computationally efficient.

To meet these challenges, in Part I, we present a new, highly stable recursive algorithm for the simulation of interacting systems in the canonical ensemble. This algorithm marries the finite temperature Auxiliary Field Quantum Monte Carlo (AFQMC) algorithm [47, 50], which has long been used to model finite temperature interacting systems, with the new Auxiliary Partition Function (APF) formalism [81], which has previously only been applied to non-interacting systems. The key realization that enables this marriage is that the Hubbard-Stratonovich (HS) Transformation [92, 93, 94], which reconstructs the properties of interacting systems by integrating over an appropriately-weighted ensemble of non-interacting systems [95], can be exploited to construct interacting partition functions and related observables in the canonical ensemble by integrating over non-interacting APF partition functions. Our algorithm can therefore stably describe interacting systems in the canonical ensemble by sampling non-interacting partition functions and other finite temperature quantities generated using the APF formalism and then integrating over those samples. This markedly improves upon our previous work which was built upon the

significantly less stable Borrmann recursion algorithm for non-interacting gases [82, 96]. To highlight the stability of our new algorithm, we show that: (1) our new interacting algorithm is stable down to substantially lower temperatures than previous algorithms and (2) it has a lower computational scaling than previous projection algorithms.

With this highly stable algorithm, we proceed to analyze differences in the convergence of the energy, sign, and information theoretic measures such as the purity and fidelity [97, 98] to the ground state between the grand canonical and canonical ensembles. To do so, we focus on the Hubbard model of interacting fermions in one and two dimensions as an instructive example because it manifests the strong correlation often resulting in a sign problem that is hardest to model via modern simulation techniques. We find that because higher-energy states are more readily accessed in the grand canonical ensemble, grand canonical energies tend to be higher and purities lower at any given temperature, meaning that the grand canonical ensemble converges more slowly to the ground state. We substantiate these findings with analytical expressions describing how these quantities should converge to the ground state in both the interacting and non-interacting limits. We furthermore demonstrate that these differences have substantial practical implications for the thermometry of cold atom systems: if the temperature of cold atom systems containing a fixed number of particles is estimated based on the grand canonical ensemble, this leads to temperature predictions that can be as much as 53.2% lower than in the more realistic canonical ensemble picture according to the analysis we present below.

1.3 Outline of Part I

The rest of Part I is organized as follows. We begin in Chapter 2 by presenting the conventional FT-AFQMC algorithm that works in the grand canonical ensemble, where many technical features introduced are maintained in our canonical ensemble extension. These features include recasting the *ab inito* Hamiltonian into Monte Carlo form (Section 2.4), discretizing the imaginary time propagation (Section 2.5), and employing the

Hubbard-Stratononvich transformation for decomposing many-body correlations (Section 2.6). Moving on to Chapter 3, we present our new algorithm along with its underlying formalism, showing how recursive relations for the partition function and one- and two-body quantities can be determined using the APF method and subsequently integrated into the FT-AFQMC algorithm. In Chapter 4, we first demonstrate the formal relationship between our recursive algorithm and the previously used Projection algorithm in Section 4.2.1. Then, we present our results regarding the increased stability of our algorithm (Section 4.2.2), before illustrating the differences in system energies (Section 4.3), purities, and fidelities (Section 4.4) as measured in the two ensembles using the Hubbard model as a salient example. We exemplify the practical consequences of these differences for thermometry in Section 4.6. We lastly conclude in Chapter 5 by discussing further applications of our algorithm and its straightforward extension to studying nuclear matter and bosons, for which it has the potential to show even greater efficiency gains.

CHAPTER 2

The Auxiliary Field Quantum Monte Carlo Method

2.1 Introduction

As discussed in Section 1.1, the finite temperature properties of a quantum system can be accessed using the imaginary-time path integral formalism, which expresses the partition function as a high-dimensional functional integral. However, directly integrating out paths in imaginary time becomes increasingly challenging for complex systems. In this regard, Quantum Monte Carlo (QMC) methods offer an approximation by statistically sampling paths, or configurations, from a probability distribution. By averaging over these sampled configurations, QMC provides estimations for the partition function, enabling the computation of various properties such as energy and correlation functions. One advantage of QMC methods is that their computational cost does not exponentially increase with system size. Additionally, the error convergence rate of QMC estimations is independent of the integral dimension, typically scaling as $\mathcal{O}(1/\sqrt{N})$. As a result, QMC is well-suited for investigating complex many-body systems where other methods may become computationally infeasible.

In this section and the following section, we present the fundamental components of standard classical Monte Carlo (MC) techniques that are crucial in the formulation of QMC. Consider an integral of a function $f(\mathbf{x})$ over a d-dimensional domain Ω, where $\mathbf{x}$ is distributed according to a normalized function $p(\mathbf{x})$:

$$I = \int_{\Omega} d\mathbf{x} p(\mathbf{x}) f(\mathbf{x}). \tag{2.1}$$

To compute I using MC, we generate a sequence of samples $\mathbf{x}_1, \mathbf{x}_2, \ldots, \mathbf{x}_i, \ldots$ by sampling from the probability density function $p(\mathbf{x})$. This means that each $\mathbf{x}_i$ is chosen in such a way that the probability of it falling within the sub-domain $(\mathbf{x}, \mathbf{x} + d\mathbf{x})$ is $p(\mathbf{x})d\mathbf{x}$. The approximation of I is then obtained by averaging over the accumulated sequence of samples

$$I \approx I_N = \frac{1}{N} \sum_{\mathbf{x}_i} f(\mathbf{x}_i) := \langle f \rangle , \tag{2.2}$$

and the convergence is ensured by the law of large numbers

$$\lim_{N \to \infty} I_N = I. \tag{2.3}$$

Given the estimation of I from I_N, the error bars of I_N can be estimated by the sample variance using the unbiased estimate of the variance

$$\mathrm{Var}(I_N) = \frac{1}{N-1} \sum_{\mathbf{x}_i} (f(\mathbf{x}_i) - \langle f \rangle)^2 = \frac{\sigma_N^2}{N}, \tag{2.4}$$

which decreases asymptotically to zero as $1/N$. The error bar is then given as

$$\delta I_N = \frac{\sigma_N}{\sqrt{N}}. \tag{2.5}$$

It is important to note that Equation (2.5) assumes a sequence of *independent* Monte Carlo samples. However, in cases where direct sampling from the probability distribution

$p(\mathbf{x})$ is not possible, as discussed in the next section, Markov chain Monte Carlo methods are employed, and the generated samples are correlated. In such cases, the actual error is given by:

$$\delta I_N = \frac{\tau_f \sigma_N}{\sqrt{N}}, \tag{2.6}$$

where τ_f represents the integrated autocorrelation time of the Markov chain that can be computed by averaging the correlation functions between samples[99]. In other words, N/τ_f corresponds to the effective number of independent samples, while τ_f denotes the number of steps required for the chain to "forget" its initial state.

2.2 The Metropolis-Hastings Algorithm

In many cases, the probability distribution function $p(\mathbf{x})$ cannot be expressed in closed form and is defined in terms of a weight function $g(\mathbf{x})$

$$p(\mathbf{x}) = \frac{g(\mathbf{x})}{\int_\Omega d\mathbf{x} g(\mathbf{x})}. \tag{2.7}$$

Here, we assume that $g(\mathbf{x})$ is positive in the domain Ω and is normalizable, i.e., $\int_\Omega g(\mathbf{x}) < \infty$. An example of such a weight function $g(\mathbf{x})$ arises in statistical mechanics, where $g(\mathbf{x})$ corresponds to the Boltzmann factor, with $g(\mathbf{x}) \sim e^{-\beta E(\mathbf{x})}$. Directly sampling from $p(\mathbf{x})$ becomes challenging because $p(\mathbf{x})$ is proportional to an unnormalized density function $g(\mathbf{x})$, but computing the normalization (denominator) is often computationally infeasible (if it were easy to compute, the entire integration could be performed directly without Monte Carlo sampling). In such cases, the Metropolis-Hastings algorithm can be employed to generate a sequence of random samples distributed according to $p(\mathbf{x})$, without knowledge of the normalization.

The Metropolis-Hastings algorithm is a Markov chain Monte Carlo (MCMC) method that generates a sequence of samples governed by the principles of a Markov chain. As the number of samples increases, the distribution of these samples incrementally converges

to the target distribution. The general scheme for the Metropolis-Hastings algorithm consists of the following steps:

- Initialization: Randomly choose an initial state $\mathbf{x}_0$ as the starting point for the Markov chain.
- Update: Generate a new candidate state $\mathbf{x}_1$ based on $\mathbf{x}_0$ by randomly change its components. Evaluate the acceptance ratio $\alpha = \min(1, g(\mathbf{x}_1)/g(\mathbf{x}_0))$. A uniform random number is then generated $u \in [0, 1]$. The proposed state $\mathbf{x}_1$ is accepted if $u < \alpha$. Otherwise, keep the current state unchanged.
- Iteration: Repeat step 2 for a desired number of iterations or until a convergence criterion is met. Each iteration generates a new state based on the previous state and the chain is updated accordingly.
- Sampling: Collect the states generated by the Markov chain once it has reached equilibrium, after a suitable "burn-in" period.

The average value can therefore be obtained as the standard approach in Eq.(2.2). In the ensuing sections, we enumerate the steps essential for deriving the weight function $g(\mathbf{x})$ that encodes the essence of many-body correlations at finite temperature, tailored for quantum MCMC sampling.

2.3 *Ab Initio* Hamiltonians

Through the scope of our discussion, we focus on the model systems described by the *Ab Initio* Hamiltonian[1]

$$\hat{H} = \hat{T} + \hat{V} = \sum_{ij} (h_{ij} \hat{c}_i^\dagger \hat{c}_j + \text{h.c.}) + \frac{1}{2} \sum_{ijkl} V_{ijkl} \hat{c}_i^\dagger \hat{c}_j^\dagger \hat{c}_k \hat{c}_l, \tag{2.8}$$

[1]While our applications mainly focus on lattice Hamiltonians, the formalism is built upon general cases. Therefore our discussion revolves around *Ab Initio* Hamiltonians to maintain generality.

where i, j, k and l denote site/orbital indices, $\hat{c}_i^\dagger$ is the creation operator that adds one electron to the ith site/orbital, and $\hat{c}_j$ is the annihilation operator that removes one electron from the jth site/orbital. h_{ij} and V_{ijkl} represent the collection of one-body and two-body electron integrals[1], respectively

$$h_{ij} = \int d\mathbf{r}\phi_i^*(\mathbf{r})\hat{h}(\mathbf{r})\phi_j(\mathbf{r}), \tag{2.9}$$

$$V_{ijkl} = \int d\mathbf{r}\phi_i^*(\mathbf{r_1})\phi_j^*(\mathbf{r_2})\frac{1}{|\mathbf{r_1}-\mathbf{r_2}|}\phi_k(\mathbf{r_1})\phi_l(\mathbf{r_2}). \tag{2.10}$$

Several things to note:

- $\hat{h}(\mathbf{r})$ is the one-body operator. In molecular systems, it is defined (assuming no relativistic effects) as $\hat{h}(\mathbf{r}) = -\frac{1}{2}\nabla^2 - \sum_A \frac{Z_A}{\mathbf{r}_A}$.
- We omit the spin component in the Hamiltonian because, as will be shown in the following, spin-up and spin-down components can be treated separately in the AFQMC framework. Hence, ϕ denotes the spatial site/orbital. Typically, the spin orbital is written as a product of the spatial part and a spin function, i.e., $\chi(\mathbf{x}) = \phi(\mathbf{r})\alpha(\omega)$ or $\chi(\mathbf{x}) = \phi(\mathbf{r})\beta(\omega)$.
- Physicists' notation is used here for the two-body integrals. In chemists' notation, it is written $\int d\mathbf{r}\phi_i^*(\mathbf{r_1})\phi_j(\mathbf{r_1})\frac{k}{|\mathbf{r_2}-\mathbf{r_2}|}\phi_k^*(\mathbf{r_2})\phi_l(\mathbf{r_2})$. Clearly the integral remains the same if the dummy indices of integration are permuted. It is easy to further verify that V_{ijkl} has an overall eightfold permutational symmetry[2] in the case of real orbitals.

2.4 Hamiltonians in Monte Carlo Form

For Hamiltonians represented in the form of Eq.(2.8), the one-body term, $\hat{T}$, proves to be relatively straightforward to handle. For instance, within the framework of Exact Diagonalization, it necessitates a matrix of dimensions $\mathcal{O}(N_s N)$ to express $\hat{T}$ for systems

[2] $V_{ijkl} = V_{jilk} = V_{klij} = V_{lkji} = V_{kjil} = V_{lijk} = V_{ilkj} = V_{jkli}$

encompassing N_s sites and N electrons. However, the inclusion of the two-body term, $\hat{V}$, causes the matrix dimensions to escalate to the order of $\binom{N_s}{N}$ due to the many-body correlations. As a result, finding a proper, approximate way of reducing the complexity of treating $\hat{V}$ is in fact the central part of contemporary electronic structure methods. In the framework of AFQMC, one decomposes the two-body term into integrals of one-body terms through the Hubbard-Stratonovich (HS) transformation, which will be introduced in the later section. The original form of $\hat{V}$ is ill-suited for the HS transformation and we need to rewrite it into the linear combination of squared one-body operators that leads to the Hamiltonian in the "Monte Carlo form"

$$\hat{H} = \hat{T} + \frac{1}{2}\sum_{\gamma} \hat{L}_{\gamma}^2, \tag{2.11}$$

where $\hat{L}_\gamma$ denotes a set of one-body operators. We now show one way to factorize $\hat{V}$ into the form of $\sum_\gamma \hat{L}_\gamma^2$, which begins with casting V_{ijkl} in the form of a Hermitian supermatrix by introducing two indices $\alpha = (i,l)$ and $\beta = (k,j)$ such that $\mathcal{V}_{\alpha\beta} = V_{ijkl}$. An eigendecomposition is then applied to the supermatrix as

$$\mathcal{V}_{\alpha\beta} = \sum_{\gamma} R_{\alpha\gamma}\lambda_\gamma R^*_{\beta\gamma}, \tag{2.12}$$

where λ_γ are eigenvalues and $R_{\alpha\gamma}$ are eigenvectors. The two-body operator $\hat{V}$ can thus be reordered as

$$\hat{V} = \frac{1}{2}\sum_{\gamma}^{(2N)^2}[\sum_{il} R_{(i,l)\gamma}\hat{c}_i^\dagger \hat{c}_l]\lambda_\gamma[\sum_{jk} R_{(k,j)\gamma}\hat{c}_k^\dagger \hat{c}_j] - \sum_{ik}(\sum_j V_{ijkj})\hat{c}_i^\dagger \hat{c}_k, \tag{2.13}$$

which can be further recast into the symmetric form by defining $\hat{\rho}_\gamma := \sum_{il} R_{(i,l)\gamma}\hat{c}_i^\dagger \hat{c}_l$, $\hat{\rho}_\gamma^\dagger := \sum_{jk} R_{(k,j)\gamma}\hat{c}_k^\dagger \hat{c}_j$ and $\hat{\rho}_0 := -\sum_{ik}(\sum_j V_{ijkj})\hat{c}_i^\dagger \hat{c}_k$

$$\hat{V} = \frac{1}{2}\sum_{\gamma}^{(2N)^2} \lambda_\gamma\{\hat{\rho}_\gamma, \hat{\rho}_\gamma^\dagger\} + \hat{\rho}_0, \tag{2.14}$$

where the anti-commutator $\{\hat{\rho}_\gamma, \hat{\rho}_\gamma^\dagger\}$ in the above equation can be expressed as a quadratic form

$$\sum_\gamma \{\hat{\rho}_\gamma, \hat{\rho}_\gamma^\dagger\} = \frac{1}{2}\sum_\gamma [(\hat{\rho}_\gamma + \hat{\rho}_\gamma^\dagger)^2 - (\hat{\rho}_\gamma - \hat{\rho}_\gamma^\dagger)^2] \equiv \sum_\gamma \hat{L}_\gamma^2. \tag{2.15}$$

We have therefore succeeded in factorizing $\hat{V}$ into the desired form.

Different flavors of such factorizations exist and for a given basis set, many techniques can be employed to reduce the number of factorization terms that is originally $2N^2$. As an example, for molecular systems with a Gaussian basis set where the matrix elements are all real, terms with small λ_γ that are below a threshold can be neglected. A modified Cholesky decomposition has also been proposed to reduce the number of factorized terms to $\mathcal{O}(N)$[100].

2.5 The Trotter Decomposition

When evaluating (finite temperature) or applying (zero temperature) operator exponentials $e^{-\beta\hat{H}}$ where $\hat{H}$ takes the form shown in Eq.(2.8), one cannot directly break the operator exponentials up into two separate parts, $e^{-\beta\hat{H}} \neq e^{-\beta\hat{T}}e^{-\beta\hat{V}}$, as $\hat{H}$ is a sum of two non-commuting terms. The Suzuki-Trotter decomposition allows us to express the imaginary time propagator as a series of infinitesimal time propagations. This decomposition enables us to write it as the product of repeated exponential operators:

$$e^{-\beta\hat{H}} = \lim_{\Delta\tau\to 0}[e^{-\Delta\tau\hat{T}}e^{-\Delta\tau\hat{V}}]^L = [e^{-\Delta\tau\hat{T}}e^{-\Delta\tau\hat{V}}]^L + \mathcal{O}(\Delta\tau), \tag{2.16}$$

where $L\Delta\tau = \beta$. A more generalized, m-order decomposition takes the form

$$e^{-\Delta\tau\hat{H}} = e^{x_1\Delta\tau\hat{T}}e^{x_2\Delta\tau\hat{V}}\cdots e^{x_m\Delta\tau\hat{T}}e^{x_m\Delta\tau\hat{V}} + \mathcal{O}(\Delta\tau^m), \tag{2.17}$$

and by coarse-graining the graph of interacting lattice models[101], it is possible to achieve any desired approximation order m systematically, but the increased computational over-

head would limit the practical use of high-order truncations. In our work, all simulations truncate the decomposition at the second order to balance speed and accuracy:

$$e^{-\Delta\tau\hat{H}} = e^{-\Delta\tau\hat{T}/2}e^{-\Delta\tau\hat{V}}e^{-\Delta\tau\hat{T}/2} + \mathcal{O}(\Delta\tau^2), \tag{2.18}$$

and the corresponding Trotter decomposition errors are typically smaller than statistical errors[102] and can be mitigated by performing a $\Delta\tau \to 0$ extrapolation. The Suzuki-Trotter decomposition is an important tool in all path-integral-based quantum Monte Carlo methods, as elaborated in the next section. However, it is also widely employed in other contexts, such as tensor network algorithms[103, 104] and quantum simulations on quantum computers[105, 106].

2.6 The Hubbard-Stratonovitch Transformation

After transforming the Hamiltonian into the "Monte Carlo form" and applying the Suzuki-Trotter decomposition, the many-body propagator is now composed of two parts. The kinetic exponential, $e^{-\Delta\tau\hat{T}/2}$, is typically straightforward to handle, while the potential exponential, $e^{-\Delta\tau\hat{V}}$, captures the many-body correlations and acts in a huge vector space that grows factorially with the system size. In the context of AFQMC, one reconstructs the properties of the many-body correlations in $e^{-\Delta\tau\hat{V}}$ through integration over a suitably weighted ensemble of non-interacting systems, accomplished via the Hubbard-Stratonovitch (HS) transformation. The generic HS transformation is based on the Gaussian integral

$$\int_{-\infty}^{\infty} d\phi e^{-\frac{(\phi+A)^2}{2}} = \sqrt{2\pi}, \tag{2.19}$$

which may be inverted as

$$e^{A^2/2} = \frac{1}{\sqrt{2\pi}} \int_{-\infty}^{\infty} d\phi e^{-\frac{\phi^2}{2}-\phi A}. \tag{2.20}$$

Hence, if A is a one-body operator, the two-body operator $e^{A^2/2}$ may be split into the integral of one-body operators interacting with a scalar field ϕ that is called auxiliary field[3]. Applying Eq.(2.20) to the γ-term of potential part in Eq.(2.11) yields

$$e^{-\frac{\Delta\tau}{2}\hat{L}_\gamma^2} = \int_{-\infty}^{\infty} d\phi_\gamma p(\phi_\gamma) e^{\sqrt{-\Delta\tau}\phi_\gamma \hat{L}_\gamma}, \tag{2.21}$$

with $p(\phi_\gamma)$ being the standard Gaussian distribution. Accumulating all terms in the two-body propagator and assembling them with the one-body, kinetic propagator, one arrives at an effective one-body propagator within a small imaginary time interval

$$e^{-\Delta\tau\hat{H}} \approx \int d\vec{\phi}_\tau p(\vec{\phi}_\tau) e^{-\Delta\tau\hat{T}/2} e^{\sum_\gamma \sqrt{-\Delta\tau}\phi_\gamma \hat{L}_\gamma} e^{-\Delta\tau\hat{T}/2} := \int d\vec{\phi}_\tau p(\vec{\phi}_\tau)\hat{B}(\vec{\phi}_\tau). \tag{2.22}$$

Here, all one-body propagators can be merged into a single, effective one-body propagator $\hat{B}(\vec{\phi}_\tau)$[107], where we denote the vector field at this time slice as $\vec{\phi}_\tau$. A propagation over the entire imaginary time from 0 to β can then be written as

$$e^{-\beta\hat{H}} \approx \int d\vec{\phi} p(\vec{\phi}) \hat{B}(\vec{\phi}_L)\cdots\hat{B}(\vec{\phi}_\tau)\cdots\hat{B}(\vec{\phi}_1), \tag{2.23}$$

where $\vec{\phi}$ represents a time-ordered auxiliary field of scalar values, $\vec{\phi} = \{\vec{\phi}_L, \ldots, \vec{\phi}_\tau, \ldots, \vec{\phi}_1\}$. The importance of (2.23) in the Monte Carlo approach lies in the fact that for a fixed field, $\vec{\phi}$, the one-body problem consists of a string of propagators $\hat{B}(\vec{\phi}_L)\cdots\hat{B}(\vec{\phi}_\tau)\cdots\hat{B}(\vec{\phi}_1)$ may be solved exactly. The integral over the field $\vec{\phi}$ can then be carried out with Monte Carlo methods.

Eq. (2.23) represents a generic transformation applicable to both fermionic and bosonic propagators[108, 109]. Notably, integration over the set of fields whose values are distributed as a high-dimensional joint Gaussian is typically cumbersome. Given the constraint on fermion occupation number, which can only be 0 or 1 due to the Pauli exclusion principle, it becomes apparent that a fluctuating field that only takes two

[3]In quantum field theory, people call it bosonic field as it is a scalar value with zero spin

discrete values could suffice to remove the fermionic many-body correlations, for a system with N_s sites/orbitals, such a discrete HS transform leads to

$$e^{-\beta\hat{H}} \approx \sum_{\vec{s}\in\{0,1\}^{N_s L}} \hat{B}(\vec{s}_L)\cdots\hat{B}(\vec{s}_\tau)\cdots\hat{B}(\vec{s}_1), \tag{2.24}$$

which clearly boosts the computational efficiency[110]. To obtain the exact form for one-body propagators at any imaginary-time step, $\hat{B}(\vec{s}_\tau)$, Hirsch introduced a discrete variant of the HS transformation, tailored for $\hat{V}$ consisting of merely density-density interactions, such as the Hubbard-type interaction[111, 112]. For elucidation, consider the Hubbard interaction for a single site:

$$\hat{V} = \hat{H}_U = U(\hat{n}_\uparrow - \frac{1}{2})(\hat{n}_\downarrow - \frac{1}{2}). \tag{2.25}$$

Hirsch proposed such an identity

$$e^{-\Delta\tau\hat{H}_U} = \gamma \sum_{s=\pm1} e^{\alpha s(\hat{n}_\uparrow - \hat{n}_\downarrow)}, \tag{2.26}$$

with $\gamma = \frac{1}{2}e^{-\Delta\tau U/4}$ and $\cosh\alpha = e^{\Delta\tau U/2}$, which can be easily verified by applying the propagator to each state vector of a single site:

$$\begin{aligned} e^{-\Delta\tau U/4}|0\rangle &= 2\gamma|0\rangle \\ e^{-\Delta\tau U/4}|\uparrow\downarrow\rangle &= 2\gamma|\uparrow\downarrow\rangle \\ e^{\Delta\tau U/4}|\uparrow\rangle &= 2\gamma\cosh\alpha|\uparrow\rangle \\ e^{\Delta\tau U/4}|\downarrow\rangle &= 2\gamma\cosh\alpha|\downarrow\rangle. \end{aligned} \tag{2.27}$$

The imaginary-time propagator is then decoupled for spin species $\hat{B}(\vec{s}_\tau) = \hat{B}_\uparrow(\vec{s}_\tau)\hat{B}_\downarrow(\vec{s}_\tau)$

with

$$\begin{aligned}\hat{B}_\uparrow(\vec{s}_\tau) &= e^{-\Delta\tau\hat{T}_\uparrow/2}e^{\alpha\sum_i s_{i,\tau}\hat{n}_{i\uparrow}}e^{-\Delta\tau\hat{T}_\uparrow/2},\\ \hat{B}_\downarrow(\vec{s}_\tau) &= e^{-\Delta\tau\hat{T}_\downarrow/2}e^{-\alpha\sum_i s_{i,\tau}\hat{n}_{i\downarrow}}e^{-\Delta\tau\hat{T}_\downarrow/2},\end{aligned} \tag{2.28}$$

whose matrix representation consists of only diagonal elements when expanded to the single-particle basis:

$$\begin{aligned}\boldsymbol{B}_\uparrow(\vec{s}_\tau) &= e^{-\Delta\tau\boldsymbol{T}_\uparrow/2}\begin{bmatrix} e^{+\alpha s_{1,\tau}} & & & \\ & e^{+\alpha s_{2,\tau}} & & \\ & & \ddots & \\ & & & e^{+\alpha s_{N_s,\tau}}\end{bmatrix}e^{-\Delta\tau\boldsymbol{T}_\uparrow/2},\\ \boldsymbol{B}_\downarrow(\vec{s}_\tau) &= e^{-\Delta\tau\boldsymbol{T}_\downarrow/2}\begin{bmatrix} e^{-\alpha s_{1,\tau}} & & & \\ & e^{-\alpha s_{2,\tau}} & & \\ & & \ddots & \\ & & & e^{-\alpha s_{N_s,\tau}}\end{bmatrix}e^{-\Delta\tau\boldsymbol{T}_\downarrow/2}.\end{aligned} \tag{2.29}$$

This choice of HS transformation leads to an efficient Monte Carlo algorithm for Hubbard-type models. However, the auxiliary fields are coupled to z-component spin degrees of freedom and break $SU(2)$ spin symmetry. For a fixed auxiliary field, the measured observables lack $SU(2)$ symmetry, which can only be recovered after integration over the entire field ensemble, potentially resulting in undesirable outcomes in certain scenarios[113, 114]. To avoid symmetry breaking, one can use alternative HS transformations that couple to the density degrees of freedom:

$$e^{-\Delta\tau\hat{H}_U} = \gamma'\sum_{s=\pm1}e^{i\alpha' s(\hat{n}_\uparrow+\hat{n}_\downarrow-1)}, \tag{2.30}$$

with $\gamma' = \frac{1}{2}e^{\Delta\tau U/4}$ and $\cosh\alpha' = e^{-\Delta\tau U/2}$. Clearly, this choice of HS transformation conserves the $SU(2)$ symmetry for each realization of the field. The trade-off is that one

has to work with complex numbers (assuming $U > 0$). It turns out that when the sign problem is absent, the above choice of the HS transformation is generally more efficient in terms of convergence rate[113, 115].

For general fermionic two-body interactions that exhibit long-range correlations, such as those in Eq.(2.8), a discrete decomposition is theoretically possible as one can always find a basis where all two-body operations are local, but to date, a general scheme is still absent with only a few special cases having been reported[116]. It is worth noting that an approximate general discrete HS transformation exists, which introduces an overall systematic error and allows a single scalar field to fluctuate in a larger manifold $\{\pm 1, \pm 2\}$ instead of $\{0, 1\}$[117, 118]. When applied to the Hamiltonians in the form of Eq.(2.11), the following identity holds for small imaginary time step $\Delta\tau$:

$$e^{-\Delta\tau \hat{L}^2} = \sum_{s=\pm 1,\pm 2} \gamma(s) e^{\sqrt{-\Delta\tau}\eta(s)L} + \mathcal{O}(\Delta\tau^4), \tag{2.31}$$

with

$$\begin{aligned} \gamma(\pm 1) &= 1 + \sqrt{6}/3, \gamma(\pm 2) = 1 - \sqrt{6}/3, \\ \eta(\pm 1) &= \pm\sqrt{2(3 - \sqrt{6})}, \eta(\pm 2) = \pm\sqrt{2(3 + \sqrt{6})}. \end{aligned}$$

Although this transformation is not exact and introduces an overall systematic error proportional to $\Delta\tau^3$ in the Monte Carlo estimation of observables, it is important to note that the Suzuki-Trotter decomposition already leads to a systematic error proportional to $\Delta\tau^2$. Therefore, this approximate transformation is essentially as accurate as an exact one.

2.7 Monte Carlo Sampling in the Grand Canonical Ensemble

After introducing all the necessary prerequisites for performing an MCMC sampling within the AFQMC framework, we now revisit the grand canonical ensemble (GCE) partition function at a chemical potential μ and decompose it using the HS transformation. The imaginary-time path integral can be written as:

$$\begin{aligned} \mathcal{Z}_\mu = \mathrm{tr}\Big[e^{-\beta(\hat{H}-\mu\hat{N})}\Big] &\approx \mathrm{tr}\Big[\int d\vec{\phi} p(\vec{\phi}) \hat{B}(\vec{\phi}_L)\cdots\hat{B}(\vec{\phi}_\tau)\cdots\hat{B}(\vec{\phi}_1)\Big] \\ &= \int d\vec{\phi} p(\vec{\phi})\, \mathrm{tr}\Big[\hat{B}(\vec{\phi}_L)\cdots\hat{B}(\vec{\phi}_\tau)\cdots\hat{B}(\vec{\phi}_1)\Big]. \end{aligned} \tag{2.32}$$

Without loss of generality, the continuous HS transformation is adopted here[4] and for all of the following derivations. By denoting $\mathcal{Z}_\mu(\vec{\phi}) := \mathrm{tr}\Big[\hat{B}(\vec{\phi}_L)\cdots\hat{B}(\vec{\phi}_\tau)\cdots\hat{B}(\vec{\phi}_1)\Big]$, we obtain a field-dependent function that can be interpreted as a probability density corresponding to $g(\mathbf{x})$ introduced in Section 2.2. Once $\mathcal{Z}_\mu(\vec{\phi})$ is solved for each field realization, the standard Metropolis algorithm can be used to sample the field $\vec{\phi}$ whose distribution is proportional to $\mathcal{Z}_\mu(\vec{\phi})$. In the GCE, the trace of one-body propagators over the entire Fock space leads to a significant mathematical simplification, often referred to as tracing out all fermion degrees of freedom:

$$\mathcal{Z}_\mu(\vec{\phi}) = \det\Big[I + \boldsymbol{B}(\vec{\phi}_L)\cdots\boldsymbol{B}(\vec{\phi}_1)\Big] = \det\Big[I + \boldsymbol{B}_{\vec{\phi}}(\beta,0)\Big], \tag{2.33}$$

Here, $\boldsymbol{B}(\vec{\phi}_\tau)$ is the matrix representations of $\hat{B}(\vec{\phi}_\tau)$ measured in the single-particle basis, and $\boldsymbol{B}_{\vec{\phi}}(\beta,0)$ is the aggregated matrix from imaginary time 0 to β. The rigorous proof of Eq.(2.33) can be found in various literature sources[112, 119, 120]. Here, we provide informal proof to provide an intuitive understanding of the concept and motivate the derivations for Recursive AFQMC in the next chapter. Consider the eigendecomposition

[4]Within the scope of this thesis, the majority of simulations focus on model systems, and therefore employ the discrete HS transformation.

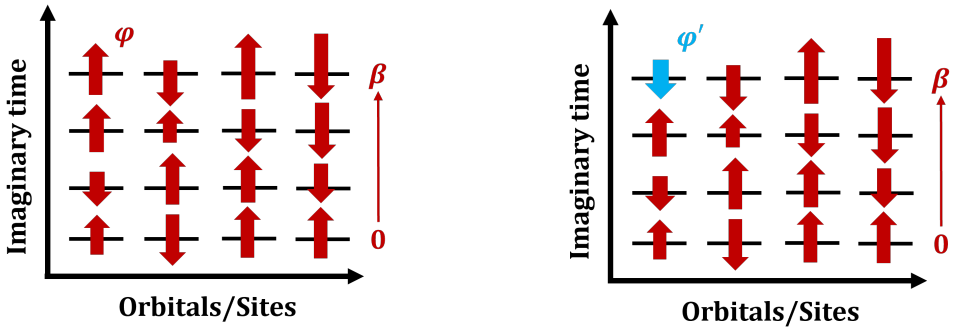

Figure 2.1: Schematic representation of the MCMC sampling process within the AFQMC framework. Each horizontal line denotes an orbital or a site, with arrows representing the auxiliary fields. The direction and length of the arrows depict the sign and magnitude of the auxiliary field, respectively. For each step in the sampling process, a perturbation is introduced to a single site, altering the field configuration from φ to φ', as illustrated by the blue arrow.

of $\boldsymbol{B}_{\vec{\phi}}(\beta, 0) = \boldsymbol{U}^{-1}\boldsymbol{\Lambda}\boldsymbol{U}$, where the spectrum $\{e^{-\epsilon_k}\} = \mathrm{diag}(\boldsymbol{\Lambda})$. The trace over the entire Fock space can be expressed as:

$$\begin{aligned}
\mathrm{tr}\Big[\hat{B}(\vec{\phi}_L)\cdots\hat{B}(\vec{\phi}_1)\Big] &= \sum_{n_k=0,1}\prod_k e^{-n_k\epsilon_k} \\
&= \prod_k\sum_{n_k=0,1} e^{-n_k\epsilon_k} \\
&= \prod_k(1+e^{\epsilon_k}) \\
&= \det\Big[I+\boldsymbol{B}_{\vec{\phi}}(\beta,0)\Big], \qquad (2.34)
\end{aligned}$$

The last equality arises from the similarity transformation. The mathematical advantage of working in the GCE is that there are no constraints on the total particle number, allowing for the reordering of operations in the second equality.

Finite temperature properties in the GCE are obtained by evaluating

$$\begin{aligned}
\left\langle\hat{O}\right\rangle &= \frac{\mathrm{tr}\left[e^{-\beta(\hat{H}-\mu\hat{N})}\hat{O}\right]}{\mathrm{tr}\left[e^{-\beta(\hat{H}-\mu\hat{N})}\right]} \\
&= \frac{1}{\mathcal{Z}_\mu}\int d\vec{\phi}p(\vec{\phi})\mathcal{Z}_\mu(\vec{\phi})\left\langle\hat{O}\right\rangle_{\vec{\phi}}. \qquad (2.35)
\end{aligned}$$

The MCMC sampling can be carried out by initializing and perturbing the field configuration $\vec{\phi}$ according to the joint Gaussian $p(\vec{\phi})$, and performing the Metropolis test by computing the ratio of $\mathcal{Z}_\mu(\vec{\phi})$ before and after a perturbation:

$$r = \frac{\det\Big[I + \boldsymbol{B}_{\vec{\phi}'}(\beta, 0)\Big]}{\det\Big[I + \boldsymbol{B}_{\vec{\phi}}(\beta, 0)\Big]} \tag{2.36}$$

to decide if we accept the perturbation or keep the field unchanged. A schematic diagram illustrating the Metropolis test in AFQMC is presented in Fig.2.1. The measurement can be made after several steps of such perturbation and test, to yield a field-dependent sample of observables, denoted as $\left\langle \hat{O} \right\rangle_{\vec{\phi}}$. The estimation of $\left\langle \hat{O} \right\rangle$ is obtained by averaging all $\left\langle \hat{O} \right\rangle_{\vec{\phi}}$s:

$$\left\langle \hat{O} \right\rangle \approx \frac{1}{N_{\text{sample}}} \sum_{\vec{\Phi}} \left\langle \hat{O} \right\rangle_{\vec{\Phi}}, \Phi \sim \frac{\mathcal{Z}_\mu(\vec{\Phi})}{\mathcal{Z}_\mu}, \tag{2.37}$$

and the sampling process would be repeated until the estimated results converge.

2.8 Observables and Wick's Theorem

In this section, we present a general scheme of physical measurements. Assume the observable of interest is a one-body operator, $\hat{O} = \hat{c}^\dagger \boldsymbol{A} \hat{c} \equiv \sum_{i,j} \hat{c}_i^\dagger A_{ij} \hat{c}_j$, defined at the imaginary time τ ($\tau = 0$ for typical equal-time measurements). We can measure its value

for a specified field configuration $\vec{\phi}$ as

$$\begin{aligned}
\left\langle \hat{O} \right\rangle_{\vec{\phi}} &= \left. \frac{\partial \ln \mathrm{tr}\left[\vec{B}_{\vec{\phi}}(\beta,\tau) e^{\eta \hat{O}} \vec{B}_{\vec{\phi}}(\tau,0) \right]}{\partial \eta} \right|_{\eta=0} \\
&= \left. \frac{\partial \ln \det\left[I + \boldsymbol{B}_{\vec{\phi}}(\beta,\tau) e^{\eta \boldsymbol{A}} \boldsymbol{B}_{\vec{\phi}}(\tau,0) \right]}{\partial \eta} \right|_{\eta=0} \\
&= \left. \frac{\partial \,\mathrm{Tr} \ln[I + \boldsymbol{B}_{\vec{\phi}}(\beta,\tau) e^{\eta \boldsymbol{A}} \boldsymbol{B}_{\vec{\phi}}(\tau,0)]}{\partial \eta} \right|_{\eta=0} \\
&= \mathrm{Tr}\Big[(I - (I + \boldsymbol{B}_{\vec{\phi}}(\tau,0) \boldsymbol{B}_{\vec{\phi}}(\beta,\tau))^{-1}) \boldsymbol{A} \Big],
\end{aligned} \tag{2.38}$$

and the equal-time Green's function at time τ is given by

$$G_{\vec{\phi}}(\tau) = (I + \boldsymbol{B}_{\vec{\phi}}(\tau,0) \boldsymbol{B}_{\vec{\phi}}(\beta,\tau))^{-1}. \tag{2.39}$$

One can therefore reexpress $\left\langle \hat{O} \right\rangle_{\vec{\phi}}$ in terms of elements of Green's function as

$$\left\langle \hat{O} \right\rangle_{\vec{\phi}} = \sum_{i,j} \left\langle \hat{c}_i^\dagger \hat{c}_j \right\rangle_{\vec{\phi}} A_{ij} = \sum_{i,j} (I - G_{\vec{\phi}}(\tau)_{ji}) A_{ij}. \tag{2.40}$$

One major advantage of AFQMC is its capability to measure arbitrary observables. This stems from the fact that, when considering a given Hubbard-Stratonovitch field, we solve a problem involving non-interacting fermions subjected to this time-and-space-dependent field. As a result, Wick's theorem is applicable to each instantiation of the auxiliary field:

$$\left\langle \hat{c}_i^\dagger \hat{c}_j \hat{c}_k^\dagger \hat{c}_l \right\rangle_{\vec{\phi}} = \left\langle \hat{c}_i^\dagger \hat{c}_j \right\rangle_{\vec{\phi}} \left\langle \hat{c}_k^\dagger \hat{c}_l \right\rangle_{\vec{\phi}} + \left\langle \hat{c}_i^\dagger \hat{c}_l \right\rangle_{\vec{\phi}} \left\langle \hat{c}_j \hat{c}_k^\dagger \right\rangle_{\vec{\phi}}. \tag{2.41}$$

Therefore, when evaluating a many-body operator $\hat{O}$, it is feasible to decompose the measurement into combinations of products of two-point correlation functions, which can be represented using equal-time Green's functions. For example, a generic two-body

operator, $\hat{O} = \sum_{i,j,k,l} \hat{c}_i^\dagger \hat{c}_k^\dagger A_{ijkl} \hat{c}_j \hat{c}_l$, can be measured as

$$\begin{aligned} \left\langle \hat{O} \right\rangle_{\vec{\phi}} &= \sum_{i,j,k,l} \left\langle \hat{c}_i^\dagger \hat{c}_j \hat{c}_k^\dagger \hat{c}_l \right\rangle_{\vec{\phi}} A_{ijkl} \\ &= \sum_{i,j,k,l} (D_{\vec{\phi},ij} D_{\vec{\phi},kl} + D_{\vec{\phi},il}(\delta_{jk} - D_{\vec{\phi},kj})) A_{ijkl}, \end{aligned} \tag{2.42}$$

where $D_{\vec{\phi},ij}$ is the (i,j)th element of the one-body density matrix: $D_{\vec{\phi},ij} = I - G_{\vec{\phi}}(\tau)_{ji}$.

2.9 The Sign Problem

In ideal scenarios, the AFQMC sampling process involves matrix multiplications and determinant computations, resulting in a scaling of $\mathcal{O}(N_s^3)$ for systems with N_s sites/orbitals. These operations are repeated along the imaginary time interval from 0 to β. Consequently, the overall scaling is $\mathcal{O}(\beta N_s^3)$. However, achieving such favorable polynomial scaling is often unattainable, particularly for realistic systems like molecules and solids. Like all existing fermion quantum Monte Carlo methods, AFQMC is plagued by the notorious sign problem[121]. Specifically, the integrand of the partition function is not always positive, i.e., $\mathcal{Z}_\mu(\vec{\phi}) < 0$. In such cases, $\mathcal{Z}_\mu(\vec{\phi})$ can no longer be viewed as a probability density, necessitating the use of a reweighting technique for statistically accurate estimations. By considering magnitude of the original weight $\mathcal{Z}_\mu(\vec{\phi}) = |\mathcal{Z}_\mu(\vec{\phi})| \cdot \mathrm{sgn}(\vec{\phi})$ as the new weight, we have

$$\left\langle \hat{O} \right\rangle = \frac{1}{\mathcal{Z}_\mu} \int d\vec{\phi} p(\vec{\phi}) |\mathcal{Z}_\mu(\vec{\phi})| \cdot \mathrm{sgn}(\vec{\phi}) \left\langle \hat{O} \right\rangle_{\vec{\phi}} = \frac{\left\langle \hat{O} \cdot \mathrm{sgn} \right\rangle_{\vec{\phi}}}{\langle \mathrm{sgn} \rangle_{\vec{\phi}}}. \tag{2.43}$$

This approach doesn't resolve the sign problem but rather reformulates it. The average sign over the Monte Carlo sampling appears in the denominator, and thus, the average sign impacts the time required to obtain meaningful expectation values with controlled error bars in the simulation. The issue is that when the average sign, $\langle \mathrm{sgn} \rangle_{\vec{\phi}}$, is close to zero, the estimator $\left\langle \hat{O} \right\rangle$ is highly noisy. Indeed, the average sign decays exponentially to

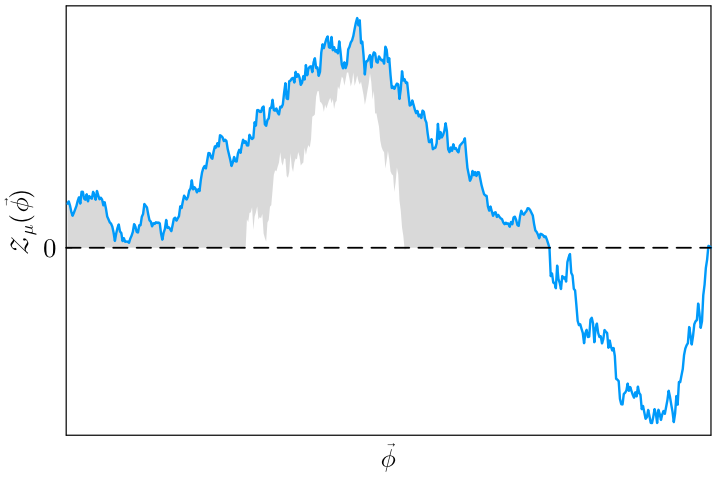

Figure 2.2: Schematic representation of the sign problem. The horizontal axis symbolizes an abstract collection of auxiliary fields, forming a sampling path in QMC simulation, while the vertical axis represents the statistical weights for each instantiation of auxiliary fields, which may take negative values. In conventional QMC where $\left|\mathcal{Z}_\mu(\vec{\phi})\right|$ is sampled, the net contribution is derived from the shaded area which is the result of subtracting the negative contributions coming from the right end of the sampling path from the positive contributions.

zero as the temperature is lowered[102, 122]

$$\langle \mathrm{sgn} \rangle_{\vec{\phi}} \sim e^{-N_s \beta \Delta f}, \tag{2.44}$$

where Δf is the free energy difference of the two systems before and after the MC update. Consequently, the contributions from the Monte Carlo samples largely cancel each other at low temperatures, as illustrated in Fig. 2.2. The partition function, which is the difference between positive and negative terms, becomes vanishingly small. Thus, the computational cost for a fixed statistical accuracy scales exponentially with the system size and inverse temperature.

While the occurrence of the fermionic sign problem depends on the specific representation and algorithm employed, it has been established that finding a general solution to the problem is NP-hard[122]. This suggests that finding a universal solution for the fermionic sign problem is considered to be exceptionally challenging if not impossible. Nonetheless,

in certain scenarios, the AFQMC algorithm does not encounter the sign problem, especially when the system possesses particular symmetries such as particle-hole symmetry (as in the half-filled Hubbard model) or, more broadly, time-reversal symmetry[123]. One common approach to addressing the sign problem is the Constrained Path Auxiliary Field Quantum Monte Carlo (CP-AFQMC) method[124, 125], which restricts the Monte Carlo sampling to regions that have positive weights, at the cost of introducing systematic errors. These errors can be somewhat alleviated by using an appropriate trial density matrix (finite temperature) or trial wave function (zero temperature), or by employing a self-consistent procedure to iteratively lessen the bias[126]. However, discrepancies between the algorithm's performance at finite and zero temperatures have been observed[80]. A recent study suggests improving the average sign at low temperatures by incrementally increasing the interaction strength during propagation, drawing from the adiabatic theorem[127]. In addition to these attempts at solving the fermionic sign problem through numerical simulations, significant efforts have been focused on identifying a wider range of models or representations that inherently avoid the sign problem. Notable examples include Majorana fermion representation[128], basis transformation[129], and Lefschetz thimbles[130].

In the simulations carried out for our study, we primarily focus on systems that are free from the sign problem or live with the sign problem, without employing those sign-problem mitigation techniques. The rationale for this is twofold: a) Our primary interest lies in exploring the intrinsic differences between ensembles (Part I). This aspect is not influenced by the presence of the sign problem; and b) The estimators for most information-theoretic measures presented in our work (Part II) are highly sensitive to the sampling scheme. Consequently, a biased estimator as in the Constraint Path could yield unpredictable results. Hence, we have decided to reserve the exploration of these measures with Constraint Path for future investigations.

CHAPTER 3

Recursive Auxiliary Field Quantum Monte Carlo Algorithm

3.1 Introduction

With the established FT-AFQMC algorithm that works in the grand canonical ensemble (GCE), the capability to trace over fermion degrees of freedom over the entire Fock space results in a significant reduction in mathematical formalism and a closed form for the statistical weight, as shown in Eq.(2.33), greatly enhances the efficiency of the Monte Carlo sampling. It is therefore natural to ask whether a similar closed form exists in the canonical ensemble (CE), where an explicit particle number constraint is imposed. In this chapter, we first demonstrate that such a closed form does not exist in the CE, thereby hindering a direct CE extension of FT-AFQMC. To overcome this issue, we introduce free fermion theories in the CE in Section 3.2. Subsequently, we incorporate these theories into the AFQMC framework and develop a robust and efficient canonical ensemble AFQMC algorithm, named Recursive AFQMC, in Section 3.3.

3.1.1 Challenges Working in the Canonical Ensemble

In quantum systems with an *ab initio* Hamiltonian in the form of Eq.(2.8), its canonical ensemble partition function takes the form

$$Z_N = \mathrm{tr}_N[e^{-\beta \hat{H}}], \tag{3.1}$$

where, unlike in the GCE partition function, the Boltzmann operator does not include a chemical potential term, and the trace is confined to an N-particle Hilbert space instead of the Fock space. This trace in the N-particle Hilbert space is denoted as tr_N. The general AFQMC framework does not depend on the choice of the ensemble because the excluded chemical potential term, $e^{\mu \hat{N}}$, only operates on a diagonal basis and essentially acts as a scaling factor. This leads to a path integral formula similar to that in the GCE:

$$Z_N \approx \mathrm{tr}_N[\int d\vec{\phi} p(\vec{\phi}) \hat{B}(\vec{\phi}_L) \cdots \hat{B}(\vec{\phi}_\tau) \cdots \hat{B}(\vec{\phi}_1)] = \int d\vec{\phi} p(\vec{\phi}) \, \mathrm{tr}_N[\hat{B}(\vec{\phi}_L) \cdots \hat{B}(\vec{\phi}_\tau) \cdots \hat{B}(\vec{\phi}_1)]. \tag{3.2}$$

Indeed, the imaginary-time propagator, $\hat{B}(\vec{\phi}_\tau)$, depends only on the Hamiltonian and the choice of HS transformation. We can define a field-dependent statistical weight in the canonical ensemble (CE) similarly as:

$$Z_N(\vec{\phi}) = \mathrm{tr}_N[\hat{B}(\vec{\phi}_L) \cdots \hat{B}(\vec{\phi}_\tau) \cdots \hat{B}(\vec{\phi}_1)]. \tag{3.3}$$

In contrast to the trace over the full Fock space, it is not possible to simply eliminate the fermion degrees of freedom when taking the trace over the restricted N-particle Hilbert space. By adopting the same eigendecomposition of the propagator matrix as in Eq.(2.33), it can be expressed as:

$$\mathrm{tr}_N[\hat{B}(\vec{\phi}_L) \cdots \hat{B}(\vec{\phi}_1)] = \sum_{\{n_k\}, \sum_k n_k = N} \prod_k e^{-n_k \epsilon_k}. \tag{3.4}$$

Because of the global constraint on the number of particles, the effective occupation numbers, n_k, are correlated and must sum to a constant value, making it impossible to switch the product and summation operations. A straightforward but impractical solution would be to sum over all possible configurations of $\{n_k\}$, but this scales factorially with both N_s and N, making it highly inefficient. For context, the GCE implementation scales as $\mathcal{O}(N_s^3)$ due to determinant calculations. Performing such an operation for every Metropolis test is unfeasible, as it would limit the AFQMC simulations to very small systems.

In the following part of this chapter, we present a new, highly stable recursive algorithm to overcome this unfavorable scaling and reduce the cost of computing $Z_N(\vec{\phi})$ to $\mathcal{O}(N_s^3)$, the same order as the GCE implementation. This new algorithm can therefore stably describe interacting systems in the canonical ensemble by sampling non-interacting partition functions in the form of $Z_N(\vec{\phi})$ and other finite temperature quantities.

3.2 Free Fermions in the Canonical Ensemble: Recursive Algorithms

3.2.1 The Borrmann Recursion Algorithm

Since the HS transformation[110, 112, 46] used in AFQMC produces an ensemble of non-interacting systems by decoupling two-body operators into an integral over one-body operators. Intuitively, one may think each of those non-interacting systems can potentially be subject to the theories developed for free fermions, so a non-interacting (mean-field) canonical ensemble theory could be incorporated into AFQMC and solve the above-mentioned chanllenge. In this regard, we first discuss a recursive algorithm[82] that was proposed for ideal gas systems, before we delve into a thorough proof of this notion. This algorithm aims to compute the N-particle partition function in polynomial time.

One of the reasons it is easier to work with free particles is that the energy spectrum of the system does not depend on the number of particles, i.e., the spacing between energy levels stays the same whether particles are added to or removed from the system. Consider a two-level system of either spinless fermions or hard-core bosons with the energy levels being ϵ_1 and ϵ_2, one can write down the partition function for 1- and 2- particle state at inverse temperature β by summing over the weights all possible configurations:

$$Z_1 = e^{-\beta\epsilon_1} + e^{-\beta\epsilon_2}, Z_2 = e^{-\beta(\epsilon_1+\epsilon_2)}. \tag{3.5}$$

These two partition functions are related:

$$Z_2 = \frac{1}{2}[(e^{-\beta\epsilon_1} + e^{-\beta\epsilon_2})^2 - (e^{-2\beta\epsilon_1} + e^{-2\beta\epsilon_2})] = \frac{1}{2}(z_1 \cdot Z_1 - z_2 \cdot Z_0), \tag{3.6}$$

where we define the 1-particle partition function at inverse temperature $n\beta$: $z_n = \sum_k e^{-n\beta\epsilon_k}$. In a three-level system, this relationship becomes $Z_3 = \frac{1}{3}(z_1 \cdot Z_2 - z_2 \cdot Z_1 + z_3 \cdot Z_0)$. This hints at the possibility of building an N-particle function recursively, provided the knowledge of all the partition functions for fewer than N particles. Borrmann *et al.*[82] suggested a general recursive formula for an N_s-level system with N particles, using induction:

$$Z_N = \frac{1}{N}\sum_{k=1}^{N}(\pm 1)^{k+1} z_k Z(N-k), \tag{3.7}$$

where the minus sign and the plus sign stand for Fermi-Dirac and Bose-Einstein statistics, respectively. Since the average occupation number and the partition function are linked through a derivative with respect to the energy levels, $\langle n_k \rangle_N = -\frac{\partial}{\beta\partial\epsilon_k} \ln Z_N$, one can derive a similar recursive relation for occupation numbers using Laplace transform[131] and arrive at

$$\langle n_k \rangle_N = \frac{Z_{N-1}}{Z_N} e^{-\beta\epsilon_k} \langle 1 \pm n_k \rangle_{N-1}. \tag{3.8}$$

Again, the minus sign and the plus sign represent the fermi and boson statistics, respectively.

$e^{-\beta\epsilon_\lambda}$	$\langle n_\lambda \rangle_4$		$\langle n_\lambda \rangle_6$		$\langle n_\lambda \rangle_7$	
	Borrmann	Exact	Borrmann	Exact	Borrmann	Exact
7.958E-11	1.608E-11	1.608E-11	8.660E-10	8.658E-10	1.352E-10	3.905E-9
1.029E-9	2.080E-10	2.080E-10	1.120E-8	1.120E-8	1.749E-9	5.052E-8
6.120E-9	1.237E-9	1.237E-9	6.660E-8	6.659E-8	1.040E-8	3.004E-7
1.837E-8	3.714E-9	3.714E-9	2.000E-7	1.999E-7	3.123E-8	9.020E-7
2.390E-7	4.831E-8	4.831E-8	2.601E-6	2.600E-6	4.062E-7	1.173E-5
1.473E-6	2.977E-7	2.977E-7	1.603E-5	1.603E-5	2.503E-6	7.231E-5
8.384E-6	1.694E-6	1.694E-6	9.124E-5	9.122E-5	1.424E-5	4.115E-4
4.341E-4	8.773E-5	8.773E-5	4.723E-3	4.722E-3	7.342E-4	0.02121
1.092E-3	2.207E-4	2.207E-4	0.01187	0.01187	0.001834	0.05296
0.02717	0.005487	0.005487	0.2896	0.2895	0.3280	0.9474
0.06884	0.01388	0.01388	0.7103	0.7102	0.3388	0.9791
2.0457	0.3881	0.3881	0.9902	0.9900	0.3386	0.9993
3.5341	0.6389	0.6389	0.9944	0.9942	0.3333	0.9996
31.14609	0.9581	0.9581	0.9995	0.9993	0.2313	0.9999
302.1299	0.9957	0.9957	1.0001	0.9999	-0.09100	1.0000
3669.01383	0.9996	0.9996	0.9989	1.0000	6.9314	1.0000

Table 3.1: The illustration of the numerical sign problem for Borrmann recursion using free fermions on 16 sites. $e^{-\beta\epsilon_\lambda}$ represents the set of statistical (Boltzmann) weights for each energy levels and is randomly-generated, ϵ_λ, and $\langle n_\lambda \rangle_i$ stands for the corresponding mean occupation number of each state, where i denotes the total particle number. The exact values are computed by explicitly enumerating all N-particle configurations (brutal force) and compared against the Borrmann recursion

This recursion formula, which we refer to as the Borrmann recursion in the following, has been quite successful in calculating properties of atomic Bose gases in harmonic traps. It has been able to accurately reproduce results that align with Bosonic statistics, such as the cusp point at the critical temperature in specific heats[131], and the condensate behavior at low temperatures[132, 133].

However, when the Borrmann recursion formula is applied to systems with fermions, a problem arises. In Eq.(3.7), the minus sign causes terms with odd and even particle numbers to contribute positively and negatively, respectively, to the sum. This leads to severe cancellations, which is reminiscent of the physical sign problem in QMC discussed in Section 2.9. This particular issue, known as the numerical sign problem, stems from rounding errors that can build up during the calculation of Eq.(3.8). This has been noted

in several previous studies that discussed recursive approaches to ideal Fermi gases[134, 135, 136]. More specifically, when a large $e^{-\beta\epsilon_\lambda}$ appears in the recursive calculation, its corresponding mean occupation number, $\langle n_\lambda \rangle_N$, tends to approach 1, yielding $\langle 1 - n_\lambda \rangle_N$ values as small as 10^{-15}. When this occurs, the corresponding occupation number cannot be correctly represented by finite precision arithmetic and corrupts the recursion. Table 3.1 illustrates this by using a set of randomly generated energy levels, ϵ_λ, which are then exponentiated with an inverse temperature, β. These exponentials are used as Boltzmann weights in Eq.(3.8) to compute a series of occupation numbers with different, constrained total particle numbers. A brutal force scheme is also used to compute exact values to verify the accuracy of the Borrmann recursion. It is clear that at the fourth iteration, $N = 4$, the Borrmann recursion is pretty accurate and is nearly exact, the discrepancies increase quickly with increasing iterations, as can be seen by the time $N = 6$. Notice that the second lowest energy level (meaning second highest statistical weight) of $\langle n_\lambda \rangle_6$ is slightly greater than 1 due to the round-off error, which violates the Pauli Exclusion Principle and causes the ratio of partition functions in Eq.(3.8) to become negative in turn. Consequently, the recursion completely breaks down by $N = 7$.

We can gain some intuitive understanding of the reasons behind such numerical instability for the case of fermions at low temperatures. In addition to the alternating signs in Eq.(3.7), the contribution of high energy levels to the factors z_k, can be filtered out by limited numerical precision. This is expected to have a minimal effect on low-temperature Bose gases, as their thermodynamic properties rely heavily on the occupation of low energy levels. In contrast, the thermodynamic properties of low-temperature Fermi gases are governed by much higher energy levels in the vicinity of the Fermi level.

It is important to note that the numerical sign problem discussed here is different from the physical sign problem mentioned in Section 2.9. The physical sign problem is inherently due to the HS transformation and is very difficult to fully resolve. On the other hand, the numerical sign problem is due to the instability of the Borrmann recursion and

can be eliminated by using an alternative, stable recursive algorithm that doesn't involve alternating positive and negative signs.

3.2.2 The Auxiliary Partition Function Algorithm

Recently, a new Auxiliary Partition Function (APF) formalism has been proposed that enables the recursive computation of N-particle partition functions and related quantities for non-interacting systems from smaller particle number quantities, thus explicitly taking particle-number constraints into account[81]. In essence, the APF formalism views the canonical ensemble partition function as a sum over the probabilities of varying numbers of particles occupying different subsets of states. Unlike the Borrmann recursion, the APF formalism is able to arrive at expressions for canonical ensemble partition functions using only positive sub-quantities, and hence it is significantly more numerically stable.

Given a set $\{\lambda_i := e^{-\beta\epsilon_i}\}$ of Boltzmann factors that correspond to the single-particle energy spectrum $\{\epsilon_i\}$, we can build the desired N particle partition function recursively by including one of the levels in each recursive step, i.e.,

$$Z_N = \lambda_j Z_{N-1}^{\{\lambda_i\}\backslash\lambda_j} + Z_N^{\{\lambda_i\}\backslash\lambda_j} \ , \tag{3.9}$$

where the notation $\{\lambda_i\}\backslash\lambda_j$ implies that we exclude the specific level j from the set $\{\lambda_i\}$ (see Ref. [81] for extensive details). This recursion does not suffer from the problems of Eq.(3.7) because it is inherently positive. Yet, the unbounded nature of the Boltzmann factors λ_i can make achieving the desired numerical precision difficult, especially at low temperatures. This can be addressed with a simple trick. We modify Eq.(3.9) by inserting an arbitrary multiplicative factor A_j (to be determined below) with the inclusion of each λ_j and apply the modified equation on the modified set $\{B\lambda_i\}$, where B is an additional constant (also to be determined). This results in a modified recursion relation

$$\bar{Z}_N = A_j \left(B\lambda_j \bar{Z}_{N-1}^{\{\lambda_j\}\backslash\lambda_j} + \bar{Z}_N^{\{\lambda_j\}\backslash\lambda_j} \right), \tag{3.10}$$

and we can recover Z_N from the resulting $\bar{Z}_N$ via

$$\bar{Z}_N = B^N Z_N \prod_j A_j. \tag{3.11}$$

This suggests that we can enhance the performance of the APF recursive approach for calculating Z_N through a clever choice of the constants $\{A_j\}$ and B. In order to do so, we rearrange the fugacity expansion for the grand canonical partition function, $\mathcal{Z}_\mu$, in terms of the canonical partition functions, $Z_N = \mathrm{tr}_N\, e^{-\beta \hat{H}}$,

$$\mathcal{Z}_\mu = \sum_N e^{\beta \mu N} Z_N. \tag{3.12}$$

Dividing by the grand canonical partition function and removing the summation over N results in an expression for the particle number probability distribution given by

$$P_\mu(N) = \frac{e^{\beta \mu N} Z_N}{\mathcal{Z}_\mu}\ . \tag{3.13}$$

For non-interacting fermions, $\mathcal{Z}_\mu = \prod_j \left(1 - p_j^{(\mu)}\right)^{-1}$[67], where

$$p_j^{(\mu)} = \frac{e^{\beta \mu} \lambda_j}{1 + e^{\beta \mu} \lambda_j} \tag{3.14}$$

is the probability of occupying the j^{th} energy level. This yields

$$P_\mu(N) = e^{\beta \mu N} Z_N \prod_j \left(1 - p_j^{(\mu)}\right). \tag{3.15}$$

If we compare Eq. (3.15) with Eq. (3.11), we can identify $P_\mu(N)$ with $\bar{Z}_N$ by choosing $A_j = 1 - p_j^{(\mu)}$ and $B = e^{\beta \mu}$, which, when substituted into Eq. (3.10), results in a recursion

relation for the number probability distribution[1]

$$P_\mu(N) = p_j^{(\mu)} P_\mu^{\{\lambda_i\}\backslash\lambda_j}(N-1) + (1-p_j^{(\mu)}) P_\mu^{\{\lambda_i\}\backslash\lambda_j}(N). \tag{3.16}$$

In contrast with Eq. (3.9), all terms in the above equation are bounded between 0 and 1, which further ensures their numerical stability and automatically avoids numerical arithmetic overflow issues caused by extremely large λ_i values. Also, setting $N = 0$ in Eq. (3.13), we see that $1/\mathcal{Z}_\mu = P_\mu(0)$, which enables us to re-express Eq. (3.13) as

$$Z_N = \frac{Z_N}{Z_0} = \frac{e^{\beta\mu N} P_\mu(N)}{P_\mu(0)}, \tag{3.17}$$

where $Z_0 = 1$.

We note that in Eq.(3.17), the chemical potential μ is an algorithmic parameter that can take on any value without changing the value of the canonical trace. It need not be the many-body chemical potential, which is otherwise difficult to determine for an arbitrary system. To increase the numerical stability of Eqs.(3.16) and (3.17), it is best to select a μ around the Fermi level, where P_μ peaks at N. A good choice is $e^{\beta\mu} = |\lambda_N \lambda_{N+1}|^{1/2}$, assuming that $\{\lambda_i\}$ is sorted as $|\lambda_1| < |\lambda_2| < \cdots < |\lambda_{N_s}|$.

To demonstrate the stability of the APF recursion over the Boltzmann recursion, we carried out tests on simple harmonic oscillator models with equal energy spacing. This setup allows the N-particle partition functions to be computed analytically[137], which serve as ideal reference points for comparison. In Fig.3.1, we plot the logarithm of the partition function vs. the number of electrons (N_e) computed using the analytical formula, the Borrmann, and the APF algorithms for an equally-spaced N_s harmonic oscillators. The instability of the Borrmann recursion is indicated in its deviation from the exact results starting at around $N_s = 40$, while the APF algorithm is highly stable and matches

[1] In practice, the computation starts with a fictitious system containing zero energy levels and zero particles; the recursion then proceeds level-by-level and particle-by-particle.

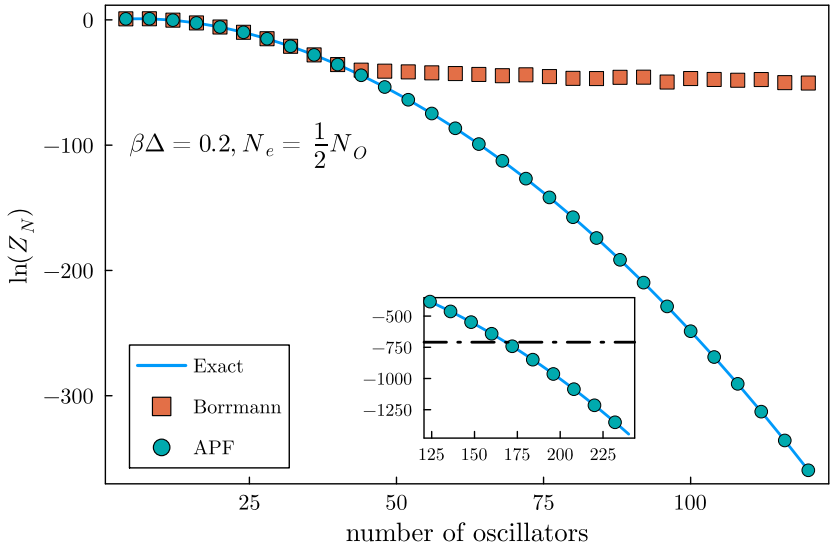

Figure 3.1: The logarithm of canonical partition functions as a function of the number of simple harmonic oscillators with equal energy spacing ($\beta\Delta = 0.2$) at half filling. The results are computed using the analytical formula, the Borrmann recursion, and the APF recursion respectively. The inset graph extends these results up to 250 oscillators, and the dashed line represents the smallest possible value ($\sim 2.22 \times 10^{-308}$) that can be represented in double-precision floating-point format.

the exact results across all the parameters we tested. Moreover, the APF recursion also effectively manages numerical overflows or underflows, because Eq.(3.17) can be presented in logarithmic form, i.e., $\ln Z_N = \beta\mu N + \ln P_\mu(N) - \ln P_\mu(0)$. As observed in the inset plot, the APF recursion remains robust even when the simulation expands to parameters that yield partition functions far smaller than the smallest value representable in double precision. This prominent feature of the APF recursion makes it an excellent fit when generalized to interacting fermions, as the inclusion of many-body correlations might result in extremely large or small partition functions.

It is worth mentioning that the particle number distribution $\mathcal{P}_\mu(N)$ can be viewed as a Poisson-binomial distribution[138], which can be expressed as

$$P_\mu(N) := \sum_{\mathcal{S}_N} \prod_{i \in \mathcal{S}_N} p_i^{(\mu)} \prod_{j \in \bar{\mathcal{S}}_N} (1 - p_j^{(\mu)}), \tag{3.18}$$

where it is constructed from the probability $p_i^{(\mu)}$ of successfully occupying N energy levels

at a given chemical potential and temperature out of a total number of independent (non-interacting) and nonidentical Bernoulli trials[81], where the corresponding set of independent success probabilities is represented by $\left\{p_i^{(\mu)}\right\}$. Here, $\mathcal{S}_N$ is a set of N occupied energy levels selected from N_s energy levels in the single-particle space; $\bar{\mathcal{S}}_N$ denotes the complement coming from unoccupied levels.

3.3 Generalization to Interacting Systems: Recursive AFQMC Formalism

Equipped with a stable algorithm, we are now prepared to address the challenge imposed by the canonical ensemble, by integrating the APF algorithm into the AFQMC framework. While a crude AFQMC generalization appears straightforward — one might simply add auxiliary-field dependence to all recursive formulas and integrate over the fields — this approach demands proof. Indeed, the sufficient condition that allows us to apply the APF algorithm to each auxiliary field realization is that the field-dependent effective energy spectrum should not vary with the particle number. In this section, we will first prove this sufficient condition, which paves the way for QMC estimation of many-body partition functions. Subsequently, we derive recursive formulas for density matrices, enabling us to establish and evaluate estimators for all equal-time observables in the canonical ensemble, such as energy and correlations.

3.3.1 Partition Function

We first show that the QMC statistical weights in the canonical ensemble, $Z_N(\vec{\phi})$, exactly correspond to the trace of a Boltzmann operator of the form $e^{-\beta\hat{H}}$, where $\hat{H}$ is a one-body operator. Recall that in Eq.(3.3), $Z_N(\vec{\phi})$ can be expressed as a product of a string of one-body propagators, $\hat{B}(\vec{\phi}_\tau)$. Using basic commutation/anticommutation rules, it can be proven[112] that the product of the $\hat{B}(\vec{\phi}_\tau)$ exactly corresponds to an exponential

of some one-body operator parameterized by the auxiliary field vector $\vec{\phi} \equiv \{\vec{\phi}_1, \ldots, \vec{\phi}_L\}$, which we denote as $\hat{h}(\vec{\phi})$

$$\begin{aligned} \prod_l^L \hat{B}(\vec{\phi}_l) &= \prod_l^L e^{-\Delta\tau\hat{K}/2} e^{\sum_\gamma \phi_l^\gamma \sqrt{-\Delta\tau\gamma_\gamma}\hat{v}_\gamma} e^{-\Delta\tau\hat{K}/2} \\ &= e^{-\beta\hat{h}(\vec{\phi})}. \end{aligned} \tag{3.19}$$

We can subsequently define a set of new boson/fermion coordinates in which $\hat{h}(\vec{\phi})$ is diagonal[112]

$$e^{-\beta\hat{h}(\vec{\phi})} = e^{-\beta\sum_{i,j} c_i^\dagger \boldsymbol{h}(\vec{\phi})_{ij}\hat{c}_j} = e^{-\beta\sum_\gamma c_\gamma^\dagger \epsilon_\gamma(\vec{\phi})\hat{c}_\gamma}, \tag{3.20}$$

where we call the set of $\{\epsilon_\gamma(\vec{\phi})\}$ the effective single-particle spectrum, because of the following relation

$$\hat{h}(\vec{\phi}) = \sum_{i,j} |i\rangle \boldsymbol{h}(\vec{\phi})_{ij}\langle j| = \sum_\gamma |\gamma\rangle\epsilon_\gamma(\vec{\phi})\langle\gamma|, \tag{3.21}$$

and

$$\hat{c}_\gamma^\dagger = \sum_i \langle i|\gamma\rangle\, \hat{c}_i^\dagger, \quad \hat{c}_\gamma = \sum_i \langle\gamma|i\rangle\, \hat{c}_i. \tag{3.22}$$

Since $e^{-\hat{h}(\vec{\phi})}$ is an independent-particle propagator that only depends on the auxiliary field vector, $\vec{\phi}$, the effective single-particle spectrum, $\{\epsilon_\gamma(\vec{\phi})\}$, is independent of the particle number. For an N-particle, N_s-site system, taking the trace while constraining the particle number yields

$$\begin{aligned} \mathrm{tr}_c(e^{-\beta\hat{h}(\vec{\phi})}) &= \mathrm{tr}_c(e^{-\beta\sum_\gamma c_\gamma^\dagger \epsilon_\gamma(\vec{\phi})\hat{c}_\gamma}) \\ &= \sum_\Gamma \langle\Gamma| e^{-\beta\sum_\gamma c_\gamma^\dagger \epsilon_\gamma(\vec{\phi})\hat{c}_\gamma} |\Gamma\rangle \\ &= \sum_\Gamma e^{-\beta\sum_{\gamma=1}^{N_s} n_\gamma \epsilon_\gamma(\vec{\phi})}. \end{aligned} \tag{3.23}$$

Here, Γ is used to represent the set of N-particle states, and thus, $\sum_\Gamma \equiv \sum_{n_1+\cdots+n_{N_s}=N}$ and n_γ denotes the number of particles in the γth eigenstate. For bosons, $n_\gamma = 0, 1, \ldots, N$,

whereas for fermions, $n_\gamma = 0, 1$. A more detailed derivation of these equations can be found in the Appendix A. The key implication of Equation (3.23) is that, for a specified field $\vec{\phi}$, the single-particle spectrum can be decoupled from the particle number. Hence, the many-particle energy given such fields is simply the sum of all of the single-particle energies, and an AFQMC generalization for the APF algorithm is valid and straightforward:

$$Z_N(\vec{\phi}) = \frac{e^{\beta\mu N} P_\mu(N, \vec{\phi})}{P_\mu(0, \vec{\phi})} \tag{3.24}$$

with recursive relation for the effective spectrum $\{\lambda_\gamma := e^{-\beta\epsilon_\gamma(\vec{\phi})}\}$:

$$P_\mu(N, \vec{\phi}) = p_\gamma^{(\mu)} P_\mu^{\{\lambda_\gamma\}\backslash\lambda_\gamma}(N-1, \vec{\phi}) + (1 - p_\gamma^{(\mu)}) P_\mu^{\{\lambda_\gamma\}\backslash\lambda_\gamma}(N, \vec{\phi}) \tag{3.25}$$

and

$$p_\gamma = \frac{e^{\beta\mu}\lambda_\gamma}{1 + e^{\beta\mu}\lambda_\gamma}.$$

In practice, we propagate the imaginary time from β to 0 by multiplying $\boldsymbol{B}(\vec{\phi}_\tau)$ matrices which results in an overall propagator matrix, $\boldsymbol{B}_{\vec{\phi}}(\beta, 0) = \prod_{\tau=0}^{\beta} \boldsymbol{B}(\vec{\phi}_\tau)$. Then, we carry out an eigendecomposition to extract the effective spectrum, $\boldsymbol{B}_{\vec{\phi}} = \mathbf{P}\Lambda\mathbf{P}^{-1}$, with $\Lambda = \mathrm{diag}(\lambda_\gamma)$. The CE partition function for field $\vec{\phi}$ is then recursively constructed using Equations (3.24) and (3.25). The overall computational cost scales as $\mathcal{O}(N_s^3 + N_s N)$, where the first term arises from diagonalizing the $N_s \times N_s$ matrix $\boldsymbol{B}_{\vec{\phi}}(\beta, 0)$, and the second term originates from the recursive calculation in Equation (3.25). In comparison to the GCE implementation that scales as $\mathcal{O}(N_s^3)$, our CE implementation only adds an extra subleading term, $\mathcal{O}(N_s N)$, which contributes minimally to the total scaling for large system sizes ($N_s \gg 1$).

3.3.2 Density Matrices

In the GCE, most observables of interest can be easily expressed in terms of elements of the one-body density matrix using thermal Wick's theorem[139], as shown in Eq.(2.41). Unfortunately, thermal Wick's theorem cannot be applied to products of field operators in

the canonical ensemble[135]. The reason is that a single creation or annihilation operator is not allowed to move cyclically across a string of operators in the CE. To be more specific, if we apply an annihilation operator in the Heisenberg representation to a quantum state in the GCE, it simplifies as[139]:

$$e^{\beta \hat{H}_0} \hat{c}_i e^{-\beta \hat{H}_0} |\psi\rangle = e^{-\beta \epsilon_i} \hat{c}_i |\psi\rangle, \tag{3.26}$$

However, such an operation in the CE violates particle number conservation, as $\hat{c}_i|\psi\rangle_N$ results in a state with $N-1$ particles. However, we can cyclically move a pair of creation and annihilation operators as it conserves the particle number:

$$e^{\beta \hat{H}_0} \hat{c}_j^\dagger \hat{c}_i e^{-\beta \hat{H}_0} |\psi\rangle = e^{-\beta(\epsilon_j - \epsilon_i)} \hat{c}_j^\dagger \hat{c}_i |\psi\rangle. \tag{3.27}$$

This hints at a generalized Wick's theorem based on commutation rules with pairs of creation and annihilation operators. In this section, we therfore present an alternative approach to obtaining the expectation values of products of operators within the canonical ensemble. Given that both Borrmann and APF algorithms are proven to be generalizable to AFQMC in the previous section, we omit all auxiliary-field dependencies for partition functions and observables for clarity.

Starting with the expectation value of the one-body density operator, we can evaluate it using the same eigendecomposition of the field-dependent propagator matrix, $\boldsymbol{B}_{\vec{\phi}} = \mathbf{P}\Lambda\mathbf{P}^{-1}$, with $\Lambda = \mathrm{diag}(\{\lambda_i\})$, which leads to

$$\langle \hat{c}_i^\dagger \hat{c}_j \rangle_N = \sum_\alpha \mathbf{P}_{i\alpha} \langle \hat{n}_\alpha \rangle_N \mathbf{P}^{-1}_{\alpha j}, \tag{3.28}$$

where $\langle \hat{n}_\alpha \rangle_N$ is computed recursively in $\mathcal{O}(N)$ operations[131, 140, 141] as

$$\langle \hat{n}_\alpha \rangle_N = \frac{\lambda_\alpha P_\mu(N-1)}{e^{\beta\mu} P_\mu(N)} (1 - \langle \hat{n}_\alpha \rangle_{N-1}) \tag{3.29}$$

with the initial condition $\langle \hat{n}_\alpha \rangle_0 = 0$ (a detailed derivation can be found in Appendix A). When λ_α is large, $\langle \hat{n}_\alpha \rangle_N$ is close to 1 and the right side of Eq. (3.29) may develop numerical round-off errors. To avoid this, we reverse the recursion and compute the "hole" distribution function for large values of λ_α

$$1 - \langle \hat{n}_\alpha \rangle_N = \frac{e^{\beta\mu} P_\mu(N+1)}{\lambda_\alpha P_\mu(N)} \langle \hat{n}_\alpha \rangle_{N+1} \tag{3.30}$$

with the initial condition $\langle \hat{n}_\alpha \rangle_{N_s} = 1$ at unit filling.

The expectation value of the two-body density operator can be computed in a similar fashion:

$$\begin{aligned} \langle \hat{c}_i^\dagger \hat{c}_j \hat{c}_k^\dagger \hat{c}_l \rangle_N &= \sum_{\alpha,\beta} [\mathbf{P}_{i\alpha} \mathbf{P}_{k\beta} \langle \hat{n}_\alpha \hat{n}_\beta \rangle_N \mathbf{P}^{-1}_{\beta l} \mathbf{P}^{-1}_{\alpha j} \\ &+ \mathbf{P}_{i\alpha} \mathbf{P}_{k\beta} \langle \hat{n}_\alpha - \hat{n}_\alpha \hat{n}_\beta \rangle_N \mathbf{P}^{-1}_{\beta j} \mathbf{P}^{-1}_{\alpha l}]. \end{aligned} \tag{3.31}$$

To express the two-level correlations in terms of occupation numbers, we use the commutation relation $\hat{c}_\beta^\dagger \hat{c}_\alpha \hat{A} = \hat{A} \hat{c}_\beta^\dagger \hat{c}_\alpha + [\hat{c}_\beta^\dagger \hat{c}_\alpha, \hat{A}]$ for a general operator $\hat{A}$, plug this relation into Eq.(3.27) and obtain

$$(\frac{\lambda_\beta}{\lambda_\alpha} - 1) \left\langle \hat{A} \hat{c}_\beta^\dagger \hat{c}_\alpha \right\rangle_N = \left\langle [\hat{c}_\beta^\dagger \hat{c}_\alpha, \hat{A}] \right\rangle_N . \tag{3.32}$$

The choice $\hat{A} = \hat{c}_\alpha^\dagger \hat{c}_\beta$ leads to

$$\langle \hat{n}_\alpha \hat{n}_\beta \rangle_N = \begin{cases} \langle \hat{n}_\alpha \rangle_N & \alpha = \beta, \\ \\ \frac{\lambda_\beta \langle \hat{n}_\alpha \rangle_N - \lambda_\alpha \langle \hat{n}_\beta \rangle_N}{\lambda_\beta - \lambda_\alpha} & \alpha \neq \beta, \end{cases} \tag{3.33}$$

which can be viewed as the lowest order canonical ensemble generalization [135, 142] of Wick's theorem [143], recently extended to the case of degenerate spectra[81]. These expressions are used throughout the rest of the thesis to compute energies, particle

densities, and correlation functions.

CHAPTER 4

Results: Benchmarks and Applications

4.1 Introduction

While our formalism generalizes to any two-body Hamiltonian, for the sake of subsequent discussion, we will focus on the fermion Hubbard model due to the strong correlation it exhibits and its relevance for the description of many useful chemical and material systems.

In this chapter, we apply the established Recursive AFQMC method to the fermion Hubbard model in one and two spatial dimensions and find improved performance over existing approaches including rapid convergence to ground state expectation values. The effects of excitations above the ground state are quantified using an estimator-agnostic approach including studying the temperature dependence of the purity and overlap fidelity of the canonical and grand canonical density matrices. As an important application, we show that thermometry approaches often exploited in ultra-cold atoms that employ an analysis of the velocity distribution in the grand canonical ensemble may be subject to errors leading to an under-estimation of extracted temperatures with respect to the Fermi

temperature.

4.1.1 Simulation Details

The Hamiltonian for the fermion Hubbard model may be expressed as

$$\hat{H} = -t \sum_{ij,\sigma} \left(\hat{c}^{\dagger}_{i,\sigma} \hat{c}_{j,\sigma} + \text{H.c.} \right) + U \sum_{i} \hat{n}_{i,\uparrow} \hat{n}_{i,\downarrow} \tag{4.1}$$

where $\hat{c}^{\dagger}_{i,\sigma}(\hat{c}_{j,\sigma})$ are anti-commuting fermionic creation(anihilation) operators such that $\hat{c}_i \hat{c}^{\dagger}_j + \hat{c}^{\dagger}_i \hat{c}_j = \delta_{ij}$ and $\hat{n}_{i,\sigma} = \hat{c}^{\dagger}_{i,\sigma} \hat{c}_{i,\sigma}$ is the local spin-resolved density for hopping parameter t and interaction strength U. In our subsequent illustrations, we pose different challenges to our formalism by varying the strength of the electron correlation, U/t, the filling (average number of electrons per site), $\langle n \rangle = (\sum_i \hat{n}_{i\uparrow} + \hat{n}_{i\downarrow})/N_s$, and number of sites, N_s, in our model. We measure energies in units of the hopping parameter t in our simulations and set $t = 1$ in the remainder of this work.

4.2 Accuracy, Stability, and Speed of Recursive AFQMC

4.2.1 Connection to Projection Algorithms

In this section, we illustrate how the more conventional particle number projection formalism[83, 144] can be derived from Eqs.(3.14), (3.15), and (3.16) through a Fourier transform, and hence that it is analytically equivalent to the recursive approach. The fact that these approaches are analytically equivalent will be of value when we compare the accuracy, stability, and speed of these methods.

We begin by considering the generating function of the partition function under the

recursive relation, Eq.(3.9), for any non-zero a

$$\begin{aligned}\sum_{N=0}^{\infty} a^N Z_N &= \lambda_j \sum_{N=1}^{\infty} a^N Z_{N-1}^{\{\lambda_j\}\backslash\lambda_j} + \sum_{N=0}^{\infty} a^N Z_N^{\{\lambda_j\}\backslash\lambda_j} \\ &= (1+a\lambda_j)\sum_{N=0}^{\infty} a^N Z_N^{\{\lambda_j\}\backslash\lambda_j}. \end{aligned} \tag{4.2}$$

By iteratively subtracting the Boltzmann factors λ_j from the set of all levels $\{\lambda_i\}$, we arrive at

$$\sum_{N=0}^{\infty} a^N Z_N = \prod_j (1+a\lambda_j)\,. \tag{4.3}$$

Setting $a = e^{\beta\mu}e^{i\phi_m}$, with $\phi_m = 2\pi m/N_s$, then yields

$$\sum_{N=0}^{\infty} e^{\beta\mu N} e^{i\phi_m N} Z_N = \prod_j (1+e^{\beta\mu}e^{i\phi_m}\lambda_j)\,. \tag{4.4}$$

Using the discrete Fourier transform of the delta function at N, $\delta_N = \sum_{m=1}^{N_s} e^{i\phi_m N}/N_s$, we can solve for $e^{\beta\mu N}Z_N$ and recover the particle number projection result for the canonical trace that was first proposed in Ref.[83]

$$\begin{aligned} Z_N &= \frac{e^{-\beta\mu N}}{N_s}\sum_{m=1}^{N_s} e^{-i\phi_m N}\prod_j (1+e^{\beta\mu}e^{i\phi_m}\lambda_j) \\ &= \frac{1}{N_s}\sum_{m=1}^{N_s} e^{-\beta\mu N}e^{-i\phi_m N}\tilde{\mathcal{Z}}_\mu(m). \end{aligned} \tag{4.5}$$

As we shall demonstrate below, the recursion formalism and the projection formalism have equivalent accuracy with recursion having slightly improved scaling ($\mathcal{O}(N_s^3 + N_s N)$ vs.$\mathcal{O}(N_s^3 + N_s^2)$ after considering the N_s^3 cost of the eigendecomposition) for computing the partition function.

4.2.2 Comparisons with Projection Algorithms

Having demonstrated that both the APF and Projection algorithms are analytically equivalent, we next compare their computational scaling. Both algorithms make heavy use of full matrix diagonalizations at an $\mathcal{O}(N_s^3)$ cost. However, due to its use of a Fourier sum, the Projection algorithm sums over N_s Fourier components with each component computing a Fourier-frequency-dependent partition function of a single-particle space of size N_s. In contrast, the APF algorithm only requires N iterations, where each iteration involves computing the occupation probability of N_s single-particle levels. Ultimately, this results in the recursive algorithm having an $\mathcal{O}(N_s^3 + N_s N)$ scaling for computing partition functions and occupation numbers (one-body densities), whereas the Projection algorithm has an $\mathcal{O}(N_s^3 + N_s^2)$ scaling. Thus, there is a clear benefit to using the APF method for filling fractions below unity. The two algorithms also possess different prefactors: the Projection algorithm requires an additional rescaling step to avoid numerical overflow when the values of the Fourier components exceed the available floating point maximum at a given precision, while the APF algorithm is automatically stabilized as the calculations are mapped to probabilities that take values in the range $[0, 1]$. This points to the recursive algorithm being more efficient, particularly at low fillings and for large system sizes.

The increased efficiency of the recursive algorithm is reflected in the left panel of Fig.4.1, which shows the wall time required for each QMC step of a random sample drawn from a HS-transformed Hubbard model with $U = 2$ and $\beta = 12$ for varying numbers of sites. As computing a full QMC step involves both leading and subleading contributions to the overall scaling of the algorithms, the plots in the left panel are reflective of the differences between the total execution times of both algorithms. In particular, the inset depicts the total speedup of the APF algorithm relative to the Projection algorithm. The $\mathcal{O}(N_s^3)$ diagonalization step is identical for both methods, so in the right panel, we additionally plot the wall time to compute the canonical partition function, $Z_N(\sigma)$, which only reflects subleading contributions to the scaling, for both methods. Regardless of the

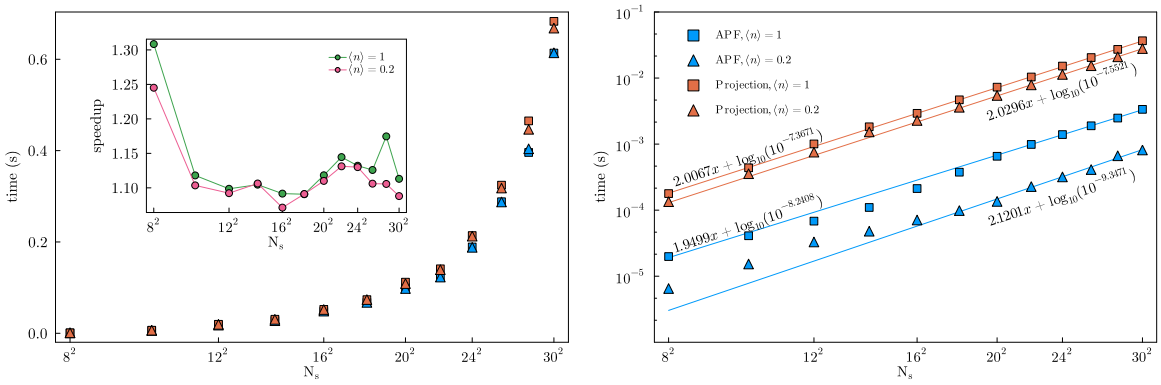

Figure 4.1: Comparison of the runtimes (shorter is better) of our Auxiliary Partition Function (APF) algorithm against the more conventional Projection algorithm for QMC samples drawn from Hubbard models with varying numbers of lattice sites, N_s, with $U = 2$ at two different fillings $\langle n \rangle = 1$ and $\langle n \rangle = 0.2$, and $\beta = 12$. Runtimes are plotted for computing a single QMC step (left panel), which reflects both leading and subleading contributions to the scaling, and the full partition function (right panel), which reflects only subleading contributions to the scaling. The inset in the left panel shows the speedup (larger is better) per QMC step of the APF algorithm relative to the Projection algorithm. Runtimes for $\langle n \rangle = 1$ are denoted by the squares, while those for $\langle n \rangle = 0.2$ are denoted by the triangles.

size of the system and the filling, we find that our APF algorithm is always faster than the Projection algorithm, in line with our scaling derivations. While one would expect the similar $\mathcal{O}(N_s^3)$ contributions to the scaling to dominate the wall times of both algorithms, we nonetheless see from the inset that the APF algorithm remains 10-15% faster than the Projection algorithm over a wide range of system sizes. This speedup leads to a significant practical gain in the efficiency of the APF algorithm relative to the Projection algorithm, especially for larger system sizes and fillings. We also observe that the time to run the Projection algorithm remained roughly the same for different filling fractions, while the wall time of the APF algorithm significantly decreased at lower fillings. Performing linear regression on the log-log data in Fig. 4.1 quantifies the overall N_s^2 scaling of the subleading contributions to the wall time (as given by the slopes of the regression lines) and reduced prefactor (as given by the regression intercepts) of the computationally more efficient APF method.

Although both algorithms could potentially be further optimized, we believe that

the scalings described here are those representative of typical implementations of these algorithms. As further discussed in the Supplementary Materials of Ref.[141], computational complexities can also be worked out for the evaluation of the level occupations and their correlation functions. We find that the cost to compute occupations and related observables follows roughly the same scaling as for calculations of the partition function.

4.3 Convergence to the Ground State Based on the Energy

Having demonstrated the markedly improved stability and speed of our new method, we can now not only assess how it performs on fully interacting systems but contrast the different physics that emerges in the canonical vs.the grand canonical ensemble down to relatively low temperatures. To appreciate these disparities, we begin by comparing how the energies of the Hubbard model converge to their ground state energies at fixed N and μ. The two ensembles are most effectively compared by choosing a grand canonical μ such that the average number of particles is given by $\langle \hat{N} \rangle_{\mu} = N$.

In the past, the convergence of the energy to its ground state value with decreasing temperature has commonly been used to assess the relative contribution of thermal quasiparticle excitations above the ground state to the overall state of the quantum system. These excitations are also a key contributor to free energy, the key property describing finite temperature thermodynamics.

In Fig. 4.2, we plot the energy per electron vs.the inverse temperature for the 6×6 Hubbard model at half-filling with $U = 4$ (and $t = 1$). Both the canonical and grand canonical ensembles yield predictably large energies at high temperatures due to the higher thermal energy enabling the electrons to access higher energy states and then converge to roughly the same energy at lower temperatures (large β). For all values of β, the canonical ensemble energy is lower, with the largest difference occurring at intermediate

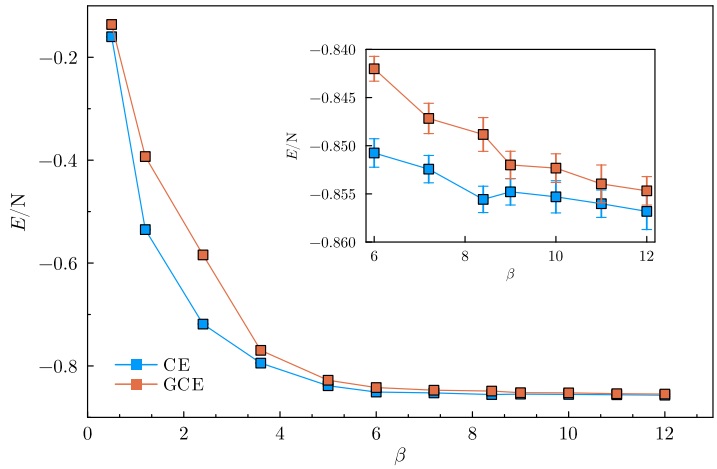

Figure 4.2: Convergence of the energy per electron in the canonical (CE) and grand canonical (GCE) ensembles as a function of the inverse temperature for a 6×6 Hubbard model at half-filling with $U = 4$. Both the main panel and inset demonstrate enhanced convergence in the canonical ensemble.

temperatures. This is because a larger number of higher energy states are accessible to the electrons in the grand canonical ensemble than in the canonical ensemble due to number fluctuations. This difference between ensembles grows with increased filling and decreased lattice size, which is in line with the intuition that differences between the ensembles should decrease as the thermodynamic limit is approached. Interestingly, despite the differences in their state spaces, both ensembles appear to converge to the same ground state energy on the scale of Fig. 4.2 at low temperatures. As we shall show next, the energy turns out to be too blunt of a metric to detect subtle and potentially important differences between ensembles.

4.4 Convergence to the Ground State Based on Information Theoretic Measures: The Purity and Fidelity

Given the similar convergence of the energy to the ground state in both ensembles discussed in the previous section, one may ask if there are more fundamental metrics

sensitive to differences between the two ensembles. Indeed, the two ensembles are comprised of different states that are accessible at different temperatures which should lead to differences in their convergence to the ground state.

For any finite-sized system, there exists a crossover temperature below which the system is effectively in its ground state. This can serve as a more direct indicator for comparing the convergence rate between ensembles than by directly comparing the β-dependence of the total energy. To quantitatively determine the crossover temperature, we are inspired by information theory and turn to the measurement of the purity

$$\mathcal{P} = \operatorname{tr} \hat{\rho}^2, \tag{4.6}$$

where $\hat{\rho}$ is the thermal density matrix. The purity quantifies how mixed a given finite temperature state is: in general, any finite temperature state is mixed and cannot be represented as a single vector in Hilbert space, resulting in a purity of less than 1, $\mathcal{P} < 1$. Thus, quantitative deviations of the purity from the identity can provide insights into the convergence to the ground state in a more general fashion than investigating any individual physical quantity whose $T = 0$ value may not be known in general.

The purity can be computed in QMC through a replica trick[145, 146] by rewriting it in terms of a ratio of partition functions

$$\begin{aligned} \operatorname{tr} \hat{\rho}^2 = \frac{Z(2\beta)}{Z^2(\beta)} &= \frac{\int_{\vec{\phi}_1,\vec{\phi}_2} \operatorname{tr}\left(\hat{U}_{\vec{\phi}}\hat{U}_{\vec{\phi}}\right)}{\int_{\vec{\phi},\vec{\phi}} \operatorname{tr}\left(\hat{U}_{\vec{\phi}_1}\right) \operatorname{tr}\left(\hat{U}_{\vec{\phi}_2}\right)} \\ &= \frac{\int_{\vec{\phi}_1,\vec{\phi}_2} Z(\vec{\phi}_1 \cup \vec{\phi}_2)}{\int_{\vec{\phi}_1,\vec{\phi}_2} Z(\vec{\phi}_1) Z(\vec{\phi}_2)} \,. \end{aligned} \tag{4.7}$$

Here, $Z(\vec{\phi}_1)$ and $Z(\vec{\phi}_2)$ are the usual partition functions (in either the canonical or grand canonical ensembles) as a function of their Hubbard-Stratonovich fields $\vec{\phi}_1$ and $\vec{\phi}_2$. $Z(\vec{\phi}_1 \cup \vec{\phi}_2)$ can be viewed as the partition function for a connected ensemble propagating

from 0 to 2β. The ensemble switching technique[147, 148] can then be adopted to efficiently sample this ratio of partition functions.

Although there is no known closed form for the purity, one can still expand ρ^2 in terms of a system's energy levels, and in the ground state (large-β) limit, only the leading term remains (see Appendix C for a full derivation)

$$\mathcal{P} \propto 1 - 2e^{-\beta \Delta E} \,. \tag{4.8}$$

In the canonical ensemble, ΔE exactly corresponds to the energy gap between the ground state and first excited state, while in the grand canonical ensemble, ΔE represents an effective energy gap that contains contributions from states with $N-1$ and $N+1$ particles as sub-leading terms. As a result, a temperature below which the system falls into its ground state region can be revealed by the onset of linear behavior when plotting $\ln(1-\mathcal{P})$ vs.β. In Fig. 4.3, we show the purity vs.temperature for Hubbard models simulated in the canonical and grand canonical ensembles for two interaction strengths U, and fit $\ln(1-\mathcal{P})$ linearly against the inverse temperature in the low-temperature region in the inset. As before, simulations performed in the canonical ensemble converge more rapidly to the ground state than those performed in the grand canonical ensemble, as indicated by the uniformly larger canonical purities for any given U. The canonical and grand canonical ensemble purities also show the greatest agreement for $U = 4$ for $\beta > 6$, when $\ln(1-\mathcal{P})$ begins to significantly deviate below zero, which echoes the convergence for $\beta > 6$ seen earlier in the energy.

However, in contrast to the relative convergence of the energy, the purity reveals additional trends rooted in the underlying physics of the finite temperature crossovers. In particular, $\ln(1-\mathcal{P})$ can be seen to crossover from exhibiting roughly constant behavior at high temperatures to exhibiting linear decay with decreasing temperature (increasing β), as predicted by Eq. (4.8). This is a clear indicator that the system has crossed into

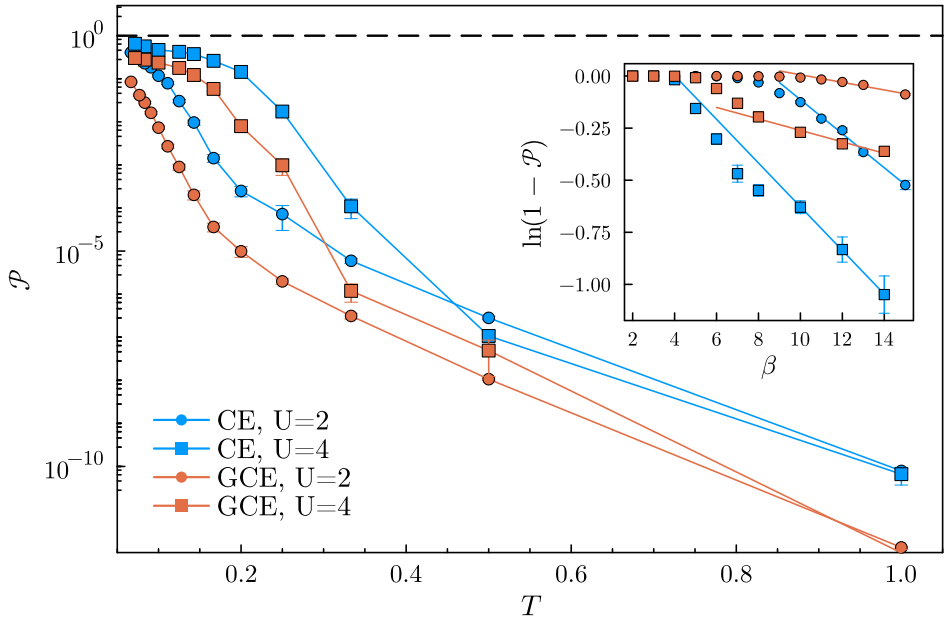

Figure 4.3: The purity, $\mathcal{P}$, of a 6×6 Hubbard model at half-filling with $U = 2$ and $U = 4$ as a function of temperature for the canonical (CE) and grand canonical (GCE) ensemble. Different symbols correspond to different interaction strengths and the lines are a guide to the eye. The inset shows $\ln(1 - \mathcal{P})$ as a function of the inverse temperature β, with the crossover to linear behavior (fitted lines) indicating convergence to the ground state (see Eq. (4.8)).

a regime that is resolving the ground states. By fitting the linear decay of $\ln(1 - \mathcal{P})$, we can also extract the energy gap ΔE from the slope of the regression lines. While it can be statistically challenging to fit curves to such small purity values in the presence of Monte Carlo uncertainties, our fitting procedure yields gaps of -0.0816 and -0.1051 for the canonical ensemble at $U = 2$ and $U = 4$, respectively, and -0.0182 and -0.0275 for the grand canonical ensemble at $U = 2$ and $U = 4$, respectively. Interestingly, the more negative canonical ensemble slopes suggest that the canonical ensemble gaps are larger than the effective grand canonical gaps, which is supported by the fact that more midgap states may be present in a grand canonical treatment. Moreover, based upon the effective gaps extracted, the systems with $U = 4$ possess larger gaps than those with $U = 2$, which is expected given the direct correlation between larger U and larger ΔE. A more detailed discussion of the information that can be obtained from the purity is presented in Appendix C.

Although the purity has provided a more detailed glimpse into the physics of the crossovers that occur in the different ensembles, it is not a measure that directly compares the two ensembles. One metric that can draw such a direct comparison is the fidelity, $\mathcal{F}(\rho, \rho')$, that measures the similarity between two density matrices ρ and ρ'.

In this case, the thermal density matrices in the two ensembles, ρ_N and ρ_μ, describe states that are not pure, and the mixed-state fidelity can be defined as the Hilbert-Schmidt inner product of ρ_N and ρ_μ normalized by the two purities[98, 149]

$$\mathcal{F}(\rho_N, \rho_\mu) = \frac{\mathrm{tr}(\rho_N \rho_\mu)}{\sqrt{\mathrm{tr}(\rho_N^2)\,\mathrm{tr}\big(\rho_\mu^2\big)}}\,. \tag{4.9}$$

It is straightforward to show that under this definition, the fidelity is normalized and reaches its maximum value of 1 if and only if $\rho_N = \rho_\mu$, and that it is also symmetric under the exchange of ρ_N and ρ_μ, $\mathcal{F}(\rho_N, \rho_\mu) = \mathcal{F}(\rho_\mu, \rho_N)$. Note that the trace in the numerator is taken over the whole Fock space, so the matrix form of ρ_N is expanded from the N-particle Hilbert space to the Fock space with varying particle numbers, but is only non-zero in the N-particle block. Moreover, when the number operator, $\hat{N}$, commutes with the Hamiltonian, as is the case for the Hubbard model, ρ_μ is block-diagonal in the particle number regardless of the interaction strength. This fact allows us to simplify the numerator of Eq. (4.9) to $\mathrm{tr}(\rho_N \rho_\mu) = P_\mu(N, \beta)\,\mathrm{tr}(\rho_N^2)$. After some algebra, we arrive at

$$\mathcal{F}(\rho_N, \rho_\mu) = \sqrt{P_\mu(N, 2\beta)} = \sqrt{\frac{e^{2\beta\mu N} Z_N(2\beta)}{\mathcal{Z}_\mu(2\beta)}}, \tag{4.10}$$

which allows $\mathcal{F}(\rho_N, \rho_\mu)$ to be directly measured within our AFQMC simulations, as the ratio between partition functions, $Z_N(2\beta)$ and $\mathcal{Z}_\mu(2\beta)$, can be measured through the same ensemble switching technique as was employed in the purity calculations.

In the ground state limit ($\beta \to \infty$), the fidelity has a similar limiting behavior as the purity, which can be derived by expanding the particle-number distribution $P_\mu(N, 2\beta)$. A

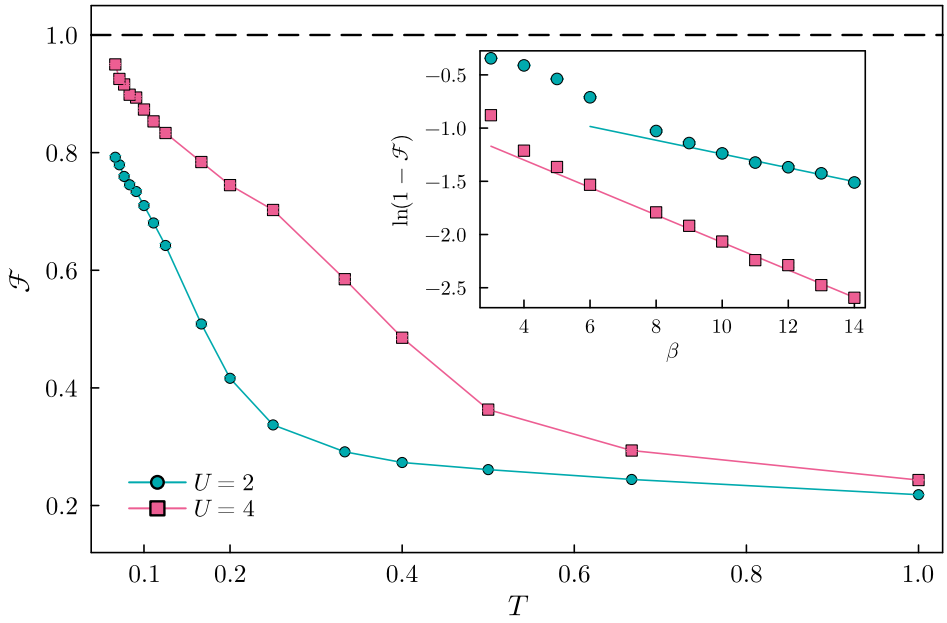

Figure 4.4: Fidelity as a function of temperature for a 6×6 Hubbard model at half-filling with $U = 2$ and $U = 4$. The inset fits $\ln(1 - \mathcal{F})$ to the inverse temperature from $\beta = 8$ to $\beta = 14$ and extends to β values where $\ln(1 - \mathcal{F})$ deviates from a linear fit. The error bars in the inset figure are smaller than the symbols.

full derivation can be found in Appendix C and yields

$$\mathcal{F} \propto 1 - \frac{g}{2} e^{-2\beta\Delta\tilde{E}}, \tag{4.11}$$

where $\Delta\tilde{E}$ is again an effective energy gap that includes the effects of the gap for the system of N particles as its leading term and the gaps for the systems of $N+1$ and $N-1$ particles as its sub-leading terms. g represents an effective degeneracy that accounts for the potentially unresolved spacing of the energy spectrum. This equation implies that plotting $\ln(1 - \mathcal{F})$ against β is expected to possess linear scaling in the large-β limit.

In Fig. 4.4, we show the fidelity vs. temperature as well as $\ln(1 - \mathcal{F})$ vs. β in the inset. From this plot, we see that the fidelity is larger for $U = 4$ than $U = 2$, meaning that, at low temperatures, the ensembles are more similar for larger U values. This is likely because larger U values result in a larger gap, which limits how many additional grand canonical states the system can access beyond those occupied in the canonical

ensemble. From the inset, we additionally observe how $\ln(1-\mathcal{F})$ becomes linear in β at low temperatures, as predicted by Eq. (4.11). A larger effective gap is again observed for the more strongly interacting case with $U = 4$, which possesses a more negative slope than for $U = 2$. The considerable deviation of the fidelity from unity, even at a very low temperature ($T < 0.1$), can be understood from Eq. (4.10), which definitively captures how particle number fluctuations can continue to contribute to the grand canonical density matrix, even in the limit of large systems when approaching the ground state.

Although the gaps obtained may not yet be as accurate as those obtained from excited state calculations, these examples illustrate that the purity and fidelity are much more informative metrics of convergence than the energy alone, and provide additional information that can be exploited to estimate gaps from finite temperature simulations.

4.5 The Sign Problem

After observing how the canonical ensemble converges more rapidly to the ground state, one may ask if this provides a practical way of more readily accessing $\beta \to \infty$ quantities than in the grand canonical ensemble. After all, it is reasonable to assume that if the energy and wave function converge more rapidly in the canonical ensemble, perhaps one can more readily gain access to low-temperature physics before a severe sign problem sets in at certain fillings.

To address the interplay between convergence to the ground state and the emergence of a physical fermion sign problem, we compute the average sign at different fillings for a variety of temperatures and interaction strengths. The behavior of the sign as a function of filling presented in Fig. 4.5 is representative of what we more widely observe: in general, the average sign in the canonical ensemble is less than that in the grand canonical ensemble at any given filling. Just as in the grand canonical ensemble, the sign at certain fillings is at or near 1, reflecting special symmetries and indicating that the system can be

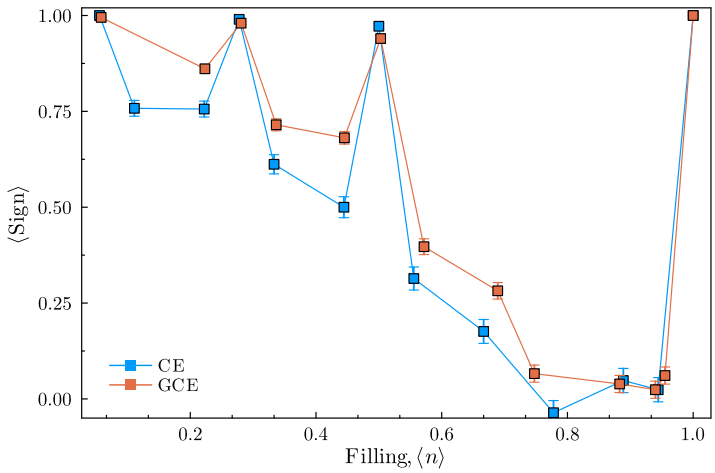

Figure 4.5: Average sign vs.filling fraction in the canonical (CE) and grand canonical (GCE) ensembles of a 6×6 Hubbard model with $U = 4$ and $\beta = 10$.

modeled with no approximations at polynomial cost. However, away from these special fillings, the average sign decreases, meaning that either exponentially more samples must be taken to converge average observables or sign mitigation strategies must be employed. Unfortunately, where the sign problem is present, the canonical sign problem appears to be more severe. This is likely a consequence of the fact that the canonical ensemble more quickly converges to the ground state: the same states that lower the canonical energy relative to the grand canonical energy are those that give rise to a more significant sign problem. This presents a practical tradeoff. While the canonical ensemble more rapidly converges to the ground state with decreasing temperature, it does so with an increased sign problem, signifying that simulations in the canonical ensemble do not allow for a way to mitigate costs associated with simulating many-body systems of fermions. The ground state of the fermion Hubbard model at most fillings possesses a significant sign problem; the more rapidly this ground state is approached, the more rapidly a sign problem emerges, regardless of ensemble.

4.6 Thermometry

While the energy and sign are two of the most commonly measured observables in stochastic many-body simulations, densities and correlation functions enable the most direct comparisons with experiments. One may therefore ask what significant differences may exist between canonical and grand canonical densities. This is not an idle question: many recent cold atom experiments estimate the temperature of their trapped gases assuming that the constituent particles interact according to the grand canonical ensemble[150, 68]. Although this is valid at large particle numbers, many such experiments are performed in a mesoscopic regime in which only a finite number of particles are present. Making this assumption when the thermodynamic limit has not been reached, can lead to inaccurate estimates of the system temperature, resulting in incorrect phase diagrams and potentially unfounded efforts to further reduce temperatures.

To make clear the effect of choosing the incorrect ensemble on the determination of temperature in a finite closed quantum system, it is illustrative to consider the simplest extreme example of one particle ($N = 1$) distributed amongst $N_s = 2$ energy levels $\{0, \Delta\}$. In the canonical ensemble,

$$\langle n_1 \rangle_1 = \frac{1}{1 + e^{-\beta\Delta}}; \qquad \langle n_2 \rangle_1 = e^{-\beta\Delta} \langle n_1 \rangle_1 \ , \tag{4.12}$$

while in the grand canonical ensemble, these average occupations depend on the chemical potential μ,

$$\langle n_1 \rangle_\mu = \frac{1}{1 + e^{-\beta\mu}}; \qquad \langle n_2 \rangle_\mu = \frac{e^{-\beta(\Delta-\mu)}}{1 + e^{-\beta(\Delta-\mu)}}. \tag{4.13}$$

In Eq. (4.13), μ is chosen such that $\langle n_1 \rangle_\mu + \langle n_2 \rangle_\mu = 1$, which yields $\mu = \Delta/2$. Using this value in Eq. (4.13) and equating occupation numbers between ensembles (the quantity most directly accessible in thermometry experiments through the velocity distribution)

would require using an inverse temperature in the grand canonical ensemble that is twice that of the physical canonical temperature, *i.e.*$\beta_\mu = 2\beta \equiv 2\beta_N$. This would result in a 100% error in the extracted temperature (when the incorrect ensemble is chosen), with grand canonical simulations always predicting a *lower* temperature than the physical one.

While this is obviously an extreme (toy) example, thermometry errors can persist to larger systems that include interactions that affect other measurable quantities. Therefore, we similarly examine the differences between occupation numbers in the two different ensembles in an interacting system. The left panel of Fig. 4.6 illustrates the average occupation number at different momenta for a 2D Hubbard model at filling $\langle n \rangle = \frac{2\times 23}{36}$ with $U = 2$. Deviations are visible in the occupation numbers between the canonical and grand canonical ensembles close to the Fermi energy. As in the simple case of only one particle in two levels, demanding that occupations be equal would require shifting the grand canonical occupations to a larger value of β.

This behavior can be quantified by integrating deviations between the occupation numbers over all momenta, which for a discrete spectrum is given by

$$\chi(\beta_N, \beta_\mu) = \sum_{\boldsymbol{k}} \Big| \langle n_{\boldsymbol{k}} \rangle_N - \langle n_{\boldsymbol{k}} \rangle_\mu \Big|, \tag{4.14}$$

where each expectation value could have its own temperature to minimize deviations (as above) and μ has been fine-tuned such that the average number of particles in the grand canonical ensemble is equal to N. The results for the 6×6 Hubbard model at $U = 2$ away from half-filling ($\langle n \rangle = 1.28$) are shown in a logarithmically-scaled heat-map in the right panel of Fig. 4.6.

Complete agreement between ensembles would be signaled by a minimum in χ at $\beta_\mu = \beta_N$ (dashed line), but instead we observe considerable deviations that persist and grow at large values of β. While the magnitude of the color scale depends on the system size, one can always find a temperature region for any finite size system where high

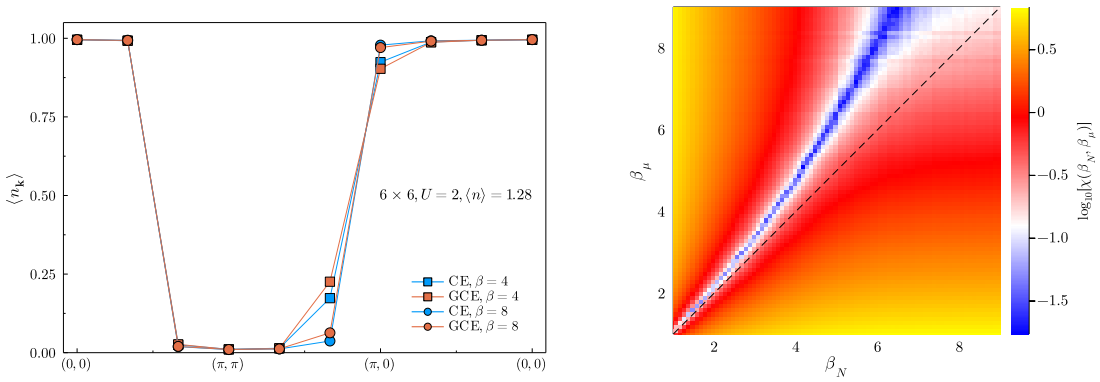

Figure 4.6: Left panel: Average momentum distribution as a function of $\vec{k}$ in the canonical and grand canonical ensembles for a 6×6 Hubbard model at $U = 2$, $\langle n \rangle = 1.28$, and either $\beta = 4$ or $\beta = 8$. Right panel: Heatmap of $\log_{10}[\chi(\beta_N, \beta_\mu)]$, the difference between the occupation of different momentum modes as a function of the temperature in the canonical and grand canonical ensembles. The dashed line denotes the diagonal at which $\beta_\mu = \beta_N$. The upward-sloping blue curve indicates that lower temperature (larger β_μ) GCE momentum distributions agree most with higher temperature (smaller β_N) CE momentum distributions.

precision thermometry protocols necessitate the use of the correct ensemble.

Second-order fluctuations in the particle number provide an even clearer way to explore the impact of choosing the incorrect ensemble. This can be quantified by the site occupancy correlation function

$$\langle \hat{n}_{\mathbf{i}} \hat{n}_{\mathbf{j}} \rangle = \langle (\hat{n}_{\mathbf{i},\uparrow} + \hat{n}_{\mathbf{i},\downarrow})(\hat{n}_{\mathbf{j},\uparrow} + \hat{n}_{\mathbf{j},\downarrow}) \rangle \,, \tag{4.15}$$

where $\mathbf{i}, \mathbf{j}$ are D-dimensional site indices. This correlation function is more naturally studied in momentum space via the static charge structure factor at wavevector $\mathbf{k}$, given by the Fourier transform of Eq. (4.15):

$$\mathcal{C}_{\mathbf{k}} = \frac{1}{N_s} \sum_{\mathbf{i},\mathbf{j}} e^{\imath \mathbf{k} \cdot (\mathbf{i} - \mathbf{j})} \langle \hat{n}_{\mathbf{i}} \hat{n}_{\mathbf{j}} \rangle \,, \tag{4.16}$$

which is, in principle, measurable in cold atom experiments through, *e.g.,*Bragg spectroscopy[151, 152, 153, 154]. To quantify the difference between ensemble predictions

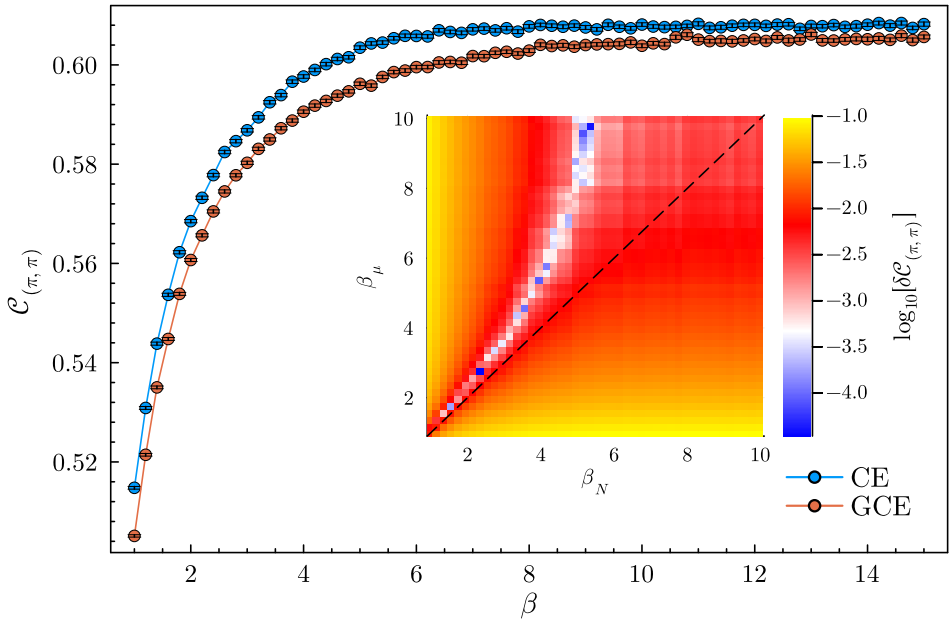

Figure 4.7: Charge structure factor at $\mathbf{k} = (\pi, \pi)$, $\mathcal{C}_{(\pi,\pi)}$, as a function of inverse temperature β in the canonical (CE) and grand canonical (GCE) ensembles for a 6×6 Hubbard model at $U = 2, \langle n \rangle = \frac{2\times23}{36} \approx 1.28$. The inset shows the heatmap of the difference in the charge structural factors, $\delta\mathcal{C}_{(\pi,\pi)}(\beta_N, \beta_\mu)$, as a function of the inverse temperature in the canonical and grand canonical ensembles.

for such a quantity, we compute $\mathcal{C}_\mathbf{k}$ at $\mathbf{k} = (\pi, \pi)$ to expose antiferromagnetic correlations for a 2D Hubbard model at $U = 2$ and filling $\langle n \rangle = \frac{2\times23}{36}$ as a function of inverse temperature β as shown in Fig. 4.7.

The odd number of electrons was chosen due to the existence of the large gap and the increased spacing of low-lying energy levels. The grand canonical ensemble simulations off of half-filling are implemented by tuning the chemical potential dynamically[85] during the Monte Carlo step to ensure $\left|\langle n \rangle_\mu - 1.28\right| < 1e^{-3}$. The deviation at each temperature is clear, with the canonical structure factor having a consistently larger value due to suppressed fluctuations. The inset shows a heat-map of the difference $\delta C_\mathbf{k}$ for each temperature $\beta \equiv \beta_N$, with the y-axis representing the effective inverse temperature β_μ needed to minimize the difference between ensembles (the horizontal shift in the main panel needed to align the two curves). Deviations of the minimum from the line $\beta_\mu = \beta_N$ captures potential errors in thermometry when using the incorrect ensemble.

The maximum deviation in the heatmap over the temperature range we study appears to be $(\beta_N, \beta_\mu) \approx (4.4, 9.4)$, which leads to a 53.2% thermometry error. Such large errors underscore the dramatic errors that can arise from an incorrect choice of ensemble and that can be addressed using the new techniques presented in this work.

CHAPTER 5

Conclusions

5.1 Overview

In summary, we have presented and illustrated applications of a new, significantly more stable recursive algorithm for determining the physics of interacting systems in the canonical ensemble. This algorithm integrates the Auxiliary Partition Function formalism, a highly stable means of computing the properties of non-interacting systems in the canonical ensemble, into the Auxiliary Field Quantum Monte Carlo framework by exploiting the Hubbard-Stratonovich Transformation. We demonstrate the stability of this algorithm and then showcase its potential applications by studying differences in the way that the canonical and grand canonical ensembles converge to the ground state. This convergence is quantified using information theory metrics by comparing the purity of finite temperature states generated within the grand canonical and canonical frameworks. We find that the canonical AFQMC results in a suppression of the mixed state and improved fidelity with the ground state as $T \to 0$ in a practical simulation.

As an experimentally relevant application, we show that a grand canonical treatment of the thermometry of cold atom and other systems with fixed particle numbers can lead to underestimates of the temperatures of those systems, clouding investigations of their

thermodynamics. This is becoming more pressing as studies of trapped homogeneous ultra-cold fermions push into a regime of smaller T/T_F where they are more poorly described by the grand canonical ensemble. Moreover, this work has direct implications for the study of nuclear matter, which possesses fixed nucleon numbers and has traditionally been modeled using the Projection algorithm.

The fact that we find our algorithm to be more computationally-efficient than oft-used Projection algorithms opens the door to a wealth of potential new applications. To date, most Projection algorithms have been limited to system sizes of tens, to at the very most, low hundreds of particles, with application to smaller nuclei and "toy" condensed matter systems. In its present form, without many algorithmic advances or computational fine-tuning, our algorithm can readily model systems with many hundreds of particles. This opens the door to more accurate numerical descriptions of cold atom quantum simulators or mesoscale devices where discrete particle number fluctuations can influence the transport of heat and matter.

5.2 Outlook

Although we illustrated the performance of our algorithm on systems of fermions because of their greater relevance and potential to develop a sign problem, our algorithm, with appropriate modifications, is equally applicable to systems of bosons or particles with other quantum statistics. The fact that the algorithm does not require explicit knowledge of many-body chemical potentials and is stable for large systems implies that it can see wide application in the study of quantum condensates, which can be challenging to simulate in the grand canonical ensemble.

We also anticipate that our algorithm will enable more direct comparisons with other finite temperature algorithms, including the Path Integral Monte Carlo, Density Matrix Quantum Monte Carlo, and emerging Finite Temperature Coupled Cluster theories, all

of which are formulated in the canonical ensemble. Beyond the algorithmic, our work will furthermore enable seamless canonical ensemble simulations from high temperatures to the ground state where most simulations are inherently performed in the canonical ensemble. This will provide critical insights into how finite temperature physics gives rise to ground state physics in correlated systems with decreasing temperature without the noise induced by spurious particle number fluctuations. Given the correlations that fixed-particle number constraints impose on the occupancies of different states, we moreover anticipate that fluctuations and therefore the physics of systems in the canonical ensemble will be fundamentally different. We look forward to the new such canonical ensemble physics this algorithm will reveal.

Part II

Recursive Auxiliary Field Quantum Monte Carlo for Entanglement Measures

CHAPTER 6

Introduction

Understanding the properties of strongly correlated systems from the quantum-information perspective has been gaining increasing attention recently within the realms of quantum chemistry and condensed matter physics. This new perspective emphasizes investigating quantum systems through the lens of global degrees of freedom stemming from information theory, such as the mutual information[155, 156], the entanglement entropy[157, 158, 159, 160] and the fidelity susceptibility[161, 162], and provides a complementary angle to traditional quantum chemistry and condensed matter approaches, which typically focus more on local observables like correlation functions. For example, in quantum chemistry, orbital-based entanglement measures serve as diagnostic tools that distinguish between static and dynamic contributions to correlation energy[163]. These measures also provide ways to assess electron correlation effects in the bond-forming and bond-breaking processes[164] and to select suitable complete active spaces (CAS) in an automated fashion by ignoring orbitals that are weakly entangled to the rest of the system[165]. In condensed matter physics, entanglement entropy and entanglement spectra introduce a fresh perspective on understanding phases and phase transitions that do not fall within the traditional framework of symmetry breaking, including topological orders and their related transitions[166, 167, 168].

Among all of these quantum information notions, entanglement is the foundational element as it encapsulates all non-classical correlations in a many-body system and is the main contributor to the complexity of quantum systems. While quantifying entanglement in mixed states[169] remains a challenge and an active area of research, the amount of entanglement encoded in a pure state can be represented via entanglement entropy in both its von Neumann and Rényi forms. The calculation of these entanglement entropies has become critically important across many fields[170], and meeting the challenge of performing entanglement measures in interacting systems, especially in strongly correlated regimes, forms a frontier in modern computational physics and chemistry.

6.1 Entanglement Entropy

For completeness, we provide a brief review of both entanglement entropy and accessible entanglement entropy in this section. More comprehensive reviews can be found in Refs.[171, 172, 173].

6.1.1 von Neumann Entanglement Entropy

In classical physics, entropy serves as a measure of a system's randomness or disorder, and it can be seen as the lack of knowledge to fully specify the microstate of a system. This means that, among the various possible microstates of a system in thermodynamic equilibrium, all compatible with the system's macrostate[1] and subject to thermodynamic laws, there remains an uncertainty about the exact microstate the system will reside when we only know macroscopic averages. In quantum mechanics, however, a non-zero entropy arises even without a lack of information. To illustrate this, consider a quantum lattice system (Fig.6.1) with a bipartition that divides the lattice sites into two groups, A and its complement A^c [2]. The total Hilbert space is then expressible as a tensor product of

[1] In the sense that conserved quantities have the same values in the microstates and the macrostate.
[2] The process is conceptual and does not alter any properties of the system.

the Hilbert spaces of each group

$$\mathcal{H}_{\text{tot}} = \mathcal{H}_A \otimes \mathcal{H}_{A^c}, \tag{6.1}$$

where $\mathcal{H}_A$ is the Hilbert space associated with the quantum system of all physical sites enclosed within the region A. Assuming a density matrix ρ on $\mathcal{H}_{\text{tot}}$ for a pure state $|\psi\rangle$

$$\rho = |\psi\rangle\langle\psi|, \tag{6.2}$$

we define the reduced density matrix ρ_A of the region A by tracing over the degrees of freedom in region A^c

$$\rho_A := \text{tr}_{\mathcal{H}_{A^c}}(\rho) = \sum_i {}_{A^c}\langle i|\rho|i\rangle_{A^c}, \tag{6.3}$$

with $\{|i\rangle_{A^c}, i = 1, 2, \dots\}$ being an orthonormal basis in $\mathcal{H}_{A^c}$. An alternative, but more mathematically sound definition for ρ_A is the local density matrix that satisfies

$$\text{tr}_{\mathcal{H}}(\rho\hat{O}) = \text{tr}_{\mathcal{H}_A}(\rho_A\hat{O}) \tag{6.4}$$

for all local operators of the form $\hat{O} = \hat{O}_A \otimes \hat{I}_{A^c}$. In this regard, ρ_A serves as a local density matrix containing enough information to reconstruct any observable defined within subsystem A.

The von Neumann entanglement entropy is then defined as

$$S_1(\rho_A) = -\,\text{tr}_{\mathcal{H}_A}(\rho_A \ln \rho_A). \tag{6.5}$$

Note that the entanglement entropy for a pure state always vanishes, $S_1(\rho) = 0$, which is consistent with the classical interpretation of entropy[3]. To further the discussion and comparison with the classical version of the entropy, we decompose $|\psi\rangle$ into a generic

[3]A classical system residing in a single microstate with probability 1 has zero entropy.

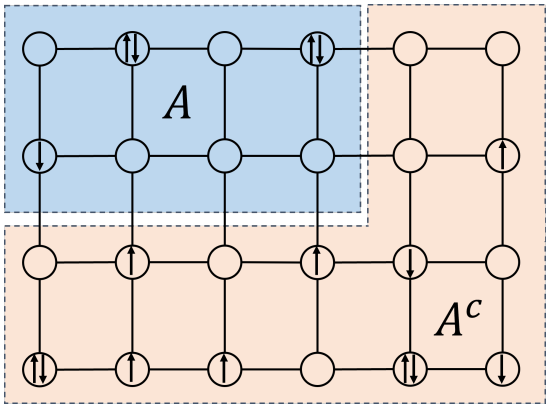

Figure 6.1: The bipartition of a lattice system into subsystem A (blue region) and its complement A^c (yellow region).

form:

$$|\psi\rangle = \sum_{i,j} c_{ij} |i\rangle_A \otimes |j\rangle_{A^c}, \tag{6.6}$$

where $|i\rangle_A$ and $|j\rangle_{A^c}$ form an orthonormal basis for $\mathcal{H}_A$ and $\mathcal{H}_{A^c}$, respectively. In cases where c_{ij} factorizes, $c_{ij} = c_i^A c_j^{A^c}$, $|i\rangle_A$ and $|j\rangle_{A^c}$ are separable and Eq.(6.6) can be recast as

$$|\psi\rangle = |\psi_A\rangle \otimes |\psi_{A^c}\rangle, \tag{6.7}$$

with both $|\psi_A\rangle = \sum_i c_i^A |i\rangle_A$ and $|\psi_{A^c}\rangle = \sum_i c_i^{A^c} |i\rangle_{A^c}$ as pure states, which implies $S_1(\rho_A) = 0$. Conversely, when c_{ij} does not factorize, $|i\rangle_A$ and $|j\rangle_{A^c}$ are "entangled." Here, a change of basis can be applied to Eq.(6.6) to achieve a Schmidt decomposition form

$$|\psi\rangle = \sum_k \sqrt{p_k} |k\rangle_A \otimes |k\rangle_{A^c}, \tag{6.8}$$

where the $\sqrt{p_k}$ are singular values of c_{ij} and satisfy $\sum_k p_k = 1$. It is then easy to write ρ_A as

$$\rho_A = \sum_k p_k |k\rangle_{AA} \langle k|, \tag{6.9}$$

which corresponds to a non-zero von Neumann entanglement entropy

$$S_1(\rho_A) = -\sum_k p_k \ln p_k, \tag{6.10}$$

which is nothing but the Shannon information entropy of the probability distribution $\{p_k\}$. In summary, for an entangled state (a superposition of quantum states, as per Eq.(6.8)), an observer with access only to subsystem A will find themselves in a mixed state, resulting in a non-zero entanglement entropy.

We conclude this section by examining some of the most significant properties of the entanglement entropy, with comprehensive derivations and interpretations available in Ref.[174].

- The entanglement entropy is continuous: $S_1(\rho_A)$ is continuous for all ρ_A in the space of normalized quantum states.

- The entanglement entropy is unitary invariant

$$S_1(\rho_A) = S_1(U\rho_A U^\dagger) \text{ for all unitary } U. \tag{6.11}$$

- For a pure state, the entanglement entropy for A and its complement A^c are the same

$$S_1(\rho_A) = S_1(\rho_{A^c}). \tag{6.12}$$

- The entanglement entropy is sub-additive:

$$S_1(\rho_{A\cup B}) \leq S_1(\rho_A) + S_1(\rho_B), \tag{6.13}$$

  for two disjoint subsystems A and B.

- The entanglement entropy is strongly sub-additivitive:

$$S_1(\rho_A) + S_1(\rho_C) \leq S_1(\rho_{A\cup B}) + S_1(\rho_{B\cup C}) \tag{6.14}$$

  for three disjoint subsystems A, B and C.

These properties are critical to our subsequent discussions, particularly regarding the topological entanglement entropy discussed in Section 8.3.

6.1.2 Rényi Entanglement Entropy

While the von Neumann entanglement entropy is the most common and direct measure of entanglement in a quantum system, it is not always easy to compute or interpret. The evaluation often requires a complete quantum state tomography of the entire density matrix ρ, as seen in various experiments[175, 176] and numerical simulations[177, 178]. This process can be prohibitively costly from both the experimental and computational perspectives. In this regard, we introduce the Rényi entanglement entropy[179] as an alternative measure of entanglement:

$$S_\alpha(\rho_A) = -\frac{1}{1-\alpha} \operatorname{tr} \rho_A^\alpha, \forall \alpha \in (0,\infty)\backslash\{1\}. \tag{6.15}$$

Unlike the von Neumann form, this metric is possible to measure experimentally using ultra-cold atoms[180, 181, 182, 183], and to compute numerically via quantum Monte Carlo[184, 185], as it can be accessed through the expectation values of local operators (which will be further discussed in Chapter 7). Crucially, the Rényi entanglement entropy retains many properties of the von Neumann entanglement entropy, including Eqs.(6.11) and (6.12)[4]. It also exhibits similar scaling forms (boundary laws)[170]. Consequently, many universal features of a quantum system can be revealed equally well using both its

[4]While the Rényi entropy is not sub-additive or strongly sub-additive, as shown in Ref.[186], weaker forms of these properties do exist for the Rényi entropy[187].

von Neumann and Rényi forms. In this sense, the Rényi entanglement entropy provides a more accessible way to obtain the information typically unveiled by the von Neumann entanglement entropy. Therefore, we only focus on the Rényi entropy in our numerical simulations.

Additionally, we note that the von Neumann entropy is a limiting case of the Rényi entropy, $S_1(\rho_A) = \lim_{\alpha\to 1} S_\alpha(\rho_A)$, which is based on the limiting identity, $\lim_{\alpha\to 1} \frac{d}{d\alpha} x^\alpha = x \ln x$.

6.2 Accessible Entanglement Entropy

In this section, we introduce the concept of the accessible entanglement entropy, a new form of entanglement entropy that measures the amount of "useful" entanglement between two parties in the presence of conservation laws. Since entanglement serves as a physical resource that can be used for quantum information (QI) processing[188], it is natural to investigate how we can effectively exploit entanglement for these tasks[189, 190], and what physical restrictions might prevent us from fully harnessing the entanglement encoded in a quantum system. In many physical systems, certain properties are conserved due to underlying symmetries. For example, total spin or charge are conserved under SU(2) (rotational) or U(1) (gauge) symmetry, respectively. These conservation laws restrict the set of operations that can be performed on the system and in turn limits the amount of entanglement that can be extracted for QI processing. As an example, we can consider a trivial one-particle state

$$|\psi_{\mathrm{AB}}\rangle = \frac{1}{\sqrt{2}}(|0_{\mathrm{A}}\rangle|1_{\mathrm{B}}\rangle + |1_{\mathrm{A}}\rangle|0_{\mathrm{B}}\rangle) \tag{6.16}$$

that contains 1 ebit of entanglement and is divided into two parties, A and B. One way to extract entanglement contained in this state for QI processing is to apply a **SWAP**

gate[174, 191] to the party A and a quantum register

$$\mathbf{SWAP}|0_{\mathrm{Reg}}\rangle \otimes \frac{1}{\sqrt{2}}(|0_{\mathrm{A}}\rangle|1_{\mathrm{B}}\rangle + |1_{\mathrm{A}}\rangle|0_{\mathrm{B}}\rangle) = |0_{\mathrm{A}}\rangle \otimes \frac{1}{\sqrt{2}}(|0_{\mathrm{Reg}}\rangle|1_{\mathrm{B}}\rangle + |1_{\mathrm{Reg}}\rangle|0_{\mathrm{B}}\rangle), \quad (6.17)$$

such that the entanglement that initially involves A is now transferred to the quantum register. However, the superposition on the RHS of Eq.(6.17) violates the particle number conservation of the system and hence such an operation between this system and a quantum register is physically forbidden (according to the so-called superselection rule). This hints that the amount of entanglement that can be physically and operationally accessed is smaller than the value provided by the von Neumann or Rényi entanglement entropy.

To address this issue, Wiseman and Vaccaro[76, 192] proposed the idea of accessible entanglement, which refers to the quantum entanglement that can be extracted from a many-body state and then transferred to a quantum register while a superselection rule (SSR) is in place. The accessible entanglement is defined as the weighted sum of the entanglement entropies, which are calculated for the projected states of fixed local particle number based on ρ_A. For the von Neumann entropy, the definition is as follows:

$$S_1^{\mathrm{acc}}(\rho_A) = \sum_n P_n S_1(\rho_{A_n}), \quad (6.18)$$

where n is the number of particles in subsystem A, P_n is the probability of A having n particles,

$$P_n := \mathrm{tr}(\Pi_n \rho_A \Pi_n), \quad (6.19)$$

with Π_n the projector onto the subspace of A with n particles, and ρ_{A_n} is the reduced density matrix of A, projected onto fixed local particle number n

$$\rho_{A_n} = \frac{1}{P_n}\Pi_n \rho_A \Pi_n. \quad (6.20)$$

For the α-Rényi entropy, the accessible entanglement entropy is expressed as[78]

$$S_\alpha^{\mathrm{acc}}(\rho_A) = \frac{\alpha}{1-\alpha} \ln[\sum_n P_n e^{\frac{1-\alpha}{\alpha} S_\alpha(\rho_{A_n})}], \tag{6.21}$$

which reduces to S_1^{acc} in the limiting case $\alpha \to 1$. Although Eq.(6.21) takes a rather complicated form, it can be simplified and associated with $S_2(\rho_A)$ via decomposition:

$$S_2(\rho_A) = S_\alpha^{\mathrm{acc}}(\rho_A) + H_{1/\alpha}(\{P_{n,\alpha}\}) \tag{6.22}$$

with $H_{1/\alpha}$ being a generalized Shannon entropy with index $1/\alpha$

$$H_{1/\alpha}(\{P_{n,\alpha}\}) = \frac{1}{1-\alpha} \ln \sum_n (P_{n,\alpha})^{1/\alpha}, \tag{6.23}$$

$$P_{n,\alpha} = \frac{\mathrm{tr}[\Pi_{A_n} \rho_A^\alpha \Pi_{A_n}]}{\mathrm{tr}\rho_A^\alpha}. \tag{6.24}$$

Conceptually, Equation 6.22 can be viewed as a decomposition of the source of the quantum entanglement: One term is more "classical" and reflects the entanglement caused by fluctuations in particle numbers, as defined by the Shannon entropy, and another is more "quantum" and represents the configurational entanglement between the subsystem and its complement, indicated by the accessible entanglement. From this perspective, the accessible entropy is not only significant as an experimentally relevant bound on the amount of extractable entanglement, but it might also display more interesting behavior across different quantum phases compared to the total entropy, as it effectively subtracts the classical "noise" produced by fluctuations.

However, the interplay of many-body correlations and a superselection rule that fixes the total particle number has not yet been thoroughly investigated, as previous studies have mainly concentrated on systems with few particles[192, 193] or non-interacting systems[78, 194]. An algorithm that enables large-scale simulations for fully interacting systems could offer valuable insights into (a) understanding how the presence of a symmetry

impacts the entanglement properties of a quantum system (b) identifying how the accessible entanglement entropy behaves differently at quantum critical points or across different phases compared to standard entanglement entropy, and (c) determining the scaling form of the accessible entanglement entropy relative to the system size. Addressing these points could provide additional information for characterizing quantum correlations and phase transitions in many-body quantum systems.

6.3 Outline of Part II

In Part II, we expand the capabilities of the Recursive AFQMC, introduced in Part I, to include the computation of entanglement entropy and its symmetry-resolved variant, the accessible entanglement entropy. This marks the *first* study of accessible entanglement entropy for fully interacting fermions. It is important to note that the investigation of entanglement properties in interacting systems remains an under-explored area, with applications to realistic systems primarily confined to small systems that can be solved with the Density Matrix Renormalization Group (DMRG)[163]. As a result, our focus throughout this part is limited to quantum many-body systems on a lattice. Despite their simplified forms, such lattice systems are ubiquitous in condensed matter and are instrumental in understanding material properties from a microscopic viewpoint.

The structure of this part is organized as follows. In Chapter 7, we delve into the algorithmic details in computing these quantities using Recursive AFQMC. Benchmark results on models that exhibit phase transitions and topological orders are presented in Chapter 8. Finally, Part II concludes with an overview of the findings as well as prospective directions for further research in Chapter 9.

CHAPTER 7

Theory and Method

7.1 Introduction

In this chapter, we introduce algorithms for computing the Rényi entanglement entropy $S_\alpha(\rho_A)$ and accessible entanglement entropy $S_\alpha^{\text{acc}}(\rho_A)$ for interacting fermionic systems, specifically for the case of $\alpha = 2$, using AFQMC. Calculating entanglement, as opposed to regular correlation functions, is a difficult task due to its inherently non-local nature and the complexity of its mathematical formulation. Unlike local observables that only depend on properties at a single point or a few points in space, entanglement entropy requires consideration of correlations among all parts of the subsystem and its complement. Moreover, the mathematical formulation of entanglement entropy involves the reduced density matrix obtained by tracing over the degrees of freedom of the subsystem's complement. This is more complicated than the calculation of correlation functions that only involves averages of products of operators. A common workaround to these challenges is the "replica trick". The core idea of the trick is to create multiple copies, or "replicas," of a system and then study the correlations among these replicas to gain insight into the entanglement properties of the original system.

We start by discussing Grover's algorithm[195][1], a direct implementation of the replica trick (Section 7.2). This algorithm extends the entanglement measures developed for free fermions and is as simple to implement as conventional AFQMC. However, it suffers from significant signal-to-noise issues even in sign-problem-free cases. A more elaborate method called the swap algorithm[147, 148], which borrows the idea of swap operations from field theory, offers better-controlled statistical errors. However, it has to work in a manually enlarged Hilbert space, leading to a rather unfavorable scaling for large systems. In Section 7.3, we propose a solution to these algorithmic issues by incorporating the estimator in Grover's algorithm into the construction of "swap" moves in the swap algorithm, thus significantly reducing the computational cost of the original swap algorithm as well as avoiding the uncontrollable statistical errors in Grover's algorithm. Lastly, in Section 7.4, we discuss how to generalize Recursive AFQMC introduced in Part I to resolve symmetry sectors in the reduced density matrix, thereby giving access to the calculation of accessible entanglement entropy.

We note that most entanglement measures used in Part II are for quantum systems in the ground state, since the finite temperature entanglement entropy is a mixture of quantum entanglement entropy (boundary law) and thermal entropy (volume law), which is less physically meaningful for use as a quantification of entanglement. This may raise some confusion as the methodology introduced in Part I is for thermal quantum states. Indeed, the finite temperature formalism in Part I can accommodate ground state calculations, as the ground state can be considered a special case of the finite temperature formalism where the inverse temperature, β, approaches infinity. In practice, the Boltzmann operator $e^{-\beta\hat{H}}$ is used as a projector in ground state calculations, and β is interpreted as an effective temperature that is sufficiently large but finite to converge the ground state wave function. The statistical weights in the ground state AFQMC then

[1]Note that this is different from the better-known Grover's algorithm in quantum computing[196].

take the form[197]

$$Z = \det\Big(P^\dagger e^{-\beta\hat{H}} P\Big), \tag{7.1}$$

where P is a projector corresponding to a ground state trial wave function, $|\psi_T\rangle$, that takes the form of a Slater determinant. Thus, we ascribe a "partition function" to the ground state in our formalism, enabling our theory to apply to both finite-temperature and ground-state scenarios. It is important to remember that this does not imply one can define a partition function in the ground state. It means that the statistical weight in the finite-β ground state AFQMC simulation can replace the partition function used in the finite temperature formalism to yield ground state results.

7.2 Grover's Algorithm

7.2.1 Reduced Density Matrix for Free Fermions

As the primary advantage of AFQMC lies in its ability to decompose an interacting system into a collection of non-interacting systems subject to free fermion theories, a natural idea is to explore the analytical expression for the reduced density matrix (RDM), ρ_A, corresponding to a subsystem of free fermions. This expression can then be applied to each effectively non-interacting system within every auxiliary field realization. In fact, RDMs for solvable fermionic and bosonic models have been studied in the early 2000s by the Density Matrix Renormalization Group (DMRG) community[198, 199, 200, 201]. This was possible because, in the Renormalization Group (RG) schemes, a large Hilbert space is continually truncated with the aim that a reduced number of states would effectively reproduce most physics from the larger set of states. Since the states of a block within a larger system are represented by RDMs, it is a natural strategy to use them to guide the truncations. While a formal analysis is conducted using Grassmann variables, we provide a less formal, more straightforward process[202] to derive the analytical expression of ρ_A, to make this section more coherent with the subsequent AFQMC generalization.

Consider a generic free fermion system with the Hamiltonian

$$\hat{H} = \sum_{i,j} h_{ij} \hat{c}_i^\dagger \hat{c}_j. \tag{7.2}$$

The elements of the related whole density matrix, ρ, can be expressed as

$$\left\langle \hat{c}_i^\dagger \hat{c}_j \right\rangle = \mathrm{tr}\Big[\rho \hat{c}_i^\dagger \hat{c}_j\Big]. \tag{7.3}$$

By definition, ρ_A must reproduce the values of $\left\langle \hat{c}_i^\dagger \hat{c}_j \right\rangle$ for all i, j in the subsystem A

$$\left\langle \hat{c}_i^\dagger \hat{c}_j \right\rangle_A = \mathrm{tr}\Big[\rho_A \hat{c}_i^\dagger \hat{c}_j\Big]. \tag{7.4}$$

This property also holds for 4-point correlations and is subject to Wick's theorem

$$\begin{aligned} \left\langle \hat{c}_i^\dagger \hat{c}_j \hat{c}_k^\dagger \hat{c}_l \right\rangle_A &= \mathrm{tr}\Big[\rho_A \hat{c}_i^\dagger \hat{c}_j \hat{c}_k^\dagger \hat{c}_l\Big] \\ &= \mathrm{tr}\Big[\rho_A \hat{c}_i^\dagger \hat{c}_j\Big]\, \mathrm{tr}\Big[\rho_A \hat{c}_k^\dagger \hat{c}_l\Big] + \mathrm{tr}\Big[\rho_A \hat{c}_i^\dagger \hat{c}_l\Big]\, \mathrm{tr}\Big[\rho_A \hat{c}_j \hat{c}_k^\dagger\Big], \end{aligned} \tag{7.5}$$

which implies that ρ_A is the density matrix of a non-interacting "entanglement Hamiltonian," denoted as $\hat{H}_A$

$$\rho_A = \frac{1}{Z_A} e^{-\hat{H}_A} = \frac{1}{Z_A} e^{-\hat{c}^\dagger \mathbf{H}_A \hat{c}}. \tag{7.6}$$

Here, Z_A is the normalization ensuring $\mathrm{tr}\,\rho_A = 1$. Similar to Section 3.3, we perform a eigendecomposition to $\hat{H}_A$ to yield

$$\rho_A = \frac{1}{Z_A} e^{-\sum_\gamma \epsilon_\gamma \hat{c}_\gamma^\dagger \hat{c}_\gamma}. \tag{7.7}$$

Assuming $\langle n_\gamma \rangle$ are eigenvalues of the local two-point correlation matrix $\left\langle \hat{c}_i^\dagger \hat{c}_j \right\rangle_A$, we can establish a Fermi-Dirac distribution for the entanglement spectra, $\{\epsilon_\gamma\}$, as

$$\langle n_\gamma \rangle = \frac{1}{1 + e^{\epsilon_\gamma}}. \tag{7.8}$$

Since two-point correlations and Green's functions are related through $\left\langle \hat{c}_i^\dagger \hat{c}_j \right\rangle = I - G_{ji}$, local two-point correlations can be linked to the Green's function by taking a submatrix of G whose indices are confined in A, $\left\langle \hat{c}_i^\dagger \hat{c}_j \right\rangle_A = I - (G_A)_{ji}$. Transforming Eq.(7.8) back to real space, we arrive at

$$I - G'_A = (1 + e^{-\mathbf{H}_A})^{-1}, \tag{7.9}$$

where the prime denotes the transpose. After some algebra, we can acquire the matrix representation of Eq.(7.8):

$$\mathbf{H}_A = \ln\big(G_A^{-1} - \mathbb{I}\big). \tag{7.10}$$

Therefore, the RDM can be written in a closed form as

$$\rho_A = \det(\mathbb{I} - G_A) e^{-\hat{c}^\dagger \ln\left(G_A^{-1} - \mathbb{I}\right)\hat{c}}. \tag{7.11}$$

Note that Z_A can be computed through the normalization

$$Z_A = \mathrm{tr}_{\mathcal{H}_A}(e^{-\hat{c}^\dagger \ln\left(G_A^{-1} - \mathbb{I}\right)\hat{c}}) = \det\big(\mathbb{I} + (G_A^{-1} - \mathbb{I})^{-1}\big) = \det(\mathbb{I} - G_A)^{-1}. \tag{7.12}$$

By substituting Eq.(7.11) into Eq.(6.15) with $\alpha = 2$, we derive the Rényi-2 entanglement entropy for free fermions

$$\begin{aligned} S_2(\rho_A) &= -\ln\big(\mathrm{tr}\,\rho_A^2\big) \\ &= -\ln\big(\det(\mathbb{I} - G_A)^2 \det\big(\mathbb{I} + (G_A^{-1} - \mathbb{I})^2\big)\big) \\ &= -\ln\big(\det\big[(\mathbb{I} - G_A)^2 + G_A^2\big]\big). \end{aligned} \tag{7.13}$$

7.2.2 AFQMC Generalization

In order to calculate the Rényi-2 entanglement entropy for interacting fermion systems via AFQMC, it is necessary to not only identify a potential estimator for $S_2(\rho_A)$ in the form suggested by Eq.(7.13), but also to devise an appropriate sampling strategy to ensure

that the estimator has a statistically correct distribution. As is put forward by Grover in his seminal paper[195], Eq.(7.11) can be generalized to interacting systems through the auxiliary-field decomposition:

$$\rho_A = \int \mathcal{D}\vec{\phi} P_{\vec{\phi}} \rho_{A,\vec{\phi}}, \tag{7.14}$$

with

$$\rho_{A,\vec{\phi}} = \det\Big(\mathbb{I} - G_{A,\vec{\phi}}\Big) e^{-\hat{c}^\dagger \ln\left(G^{-1}_{A,\vec{\phi}} - \mathbb{I}\right)\hat{c}}. \tag{7.15}$$

In this equation, $P_{\vec{\phi}}$ refers to the probability distribution of the field $\vec{\phi}$ and takes the form $P_{\vec{\phi}} = Z(\vec{\phi})/Z$. Here, $Z(\vec{\phi})$ and Z are the partition functions of the $\vec{\phi}$-dependent system and the many-body system, respectively, and can belong to grand canonical, canonical, or ground state forms.

As a result, the estimator for the Rényi-2 entropy can be constructed by using the replica trick

$$\begin{aligned}
\exp[-S_2(\rho_A)] &= \int \mathcal{D}\vec{\phi}_1 \mathcal{D}\vec{\phi}_2 P_{\vec{\phi}_1} P_{\vec{\phi}_2} \operatorname{tr}\Big[\rho_{A,\vec{\phi}_1}\rho_{A,\vec{\phi}_2}\Big] \\
&= \int \mathcal{D}\vec{\phi}_1 \mathcal{D}\vec{\phi}_2 P_{\vec{\phi}_1} P_{\vec{\phi}_2} \langle \exp[-S_2(\rho_A)]\rangle_{\vec{\phi}_1,\vec{\phi}_2} \\
&= \int \mathcal{D}\vec{\phi}_1 \mathcal{D}\vec{\phi}_2 P_{\vec{\phi}_1} P_{\vec{\phi}_2} \det\Big[(\mathbb{I} - G_{A,\vec{\phi}_1})(\mathbb{I} - G_{A,\vec{\phi}_2}) + G_{A,\vec{\phi}_1} G_{A,\vec{\phi}_2}\Big],
\end{aligned} \tag{7.16}$$

where the last equation comes from the normalization

$$\begin{aligned}
\operatorname{tr}\Big[\rho_{A,\vec{\phi}_1}\rho_{A,\vec{\phi}_2}\Big] &= \det\Big(\mathbb{I} - G_{A,\vec{\phi}_1}\Big)\det\Big(\mathbb{I} - G_{A,\vec{\phi}_2}\Big)\operatorname{tr}\left[e^{\hat{c}^\dagger \ln\left[(G^{-1}_{A,\vec{\phi}_1} - \mathbb{I})(G^{-1}_{A,\vec{\phi}_2} - \mathbb{I})\right]\hat{c}}\right] \\
&= \det\Big(\mathbb{I} - G_{A,\vec{\phi}_1}\Big)\det\Big(\mathbb{I} - G_{A,\vec{\phi}_2}\Big)\det\Big[\mathbb{I} + (G^{-1}_{A,\vec{\phi}_1} - \mathbb{I})(G^{-1}_{A,\vec{\phi}_2} - \mathbb{I})\Big] \\
&= \det\Big[(\mathbb{I} - G_{A,\vec{\phi}_1})(\mathbb{I} - G_{A,\vec{\phi}_2}) + G_{A,\vec{\phi}_1} G_{A,\vec{\phi}_2}\Big].
\end{aligned} \tag{7.17}$$

Here, $P_{\vec{\phi}_1}$ and $P_{\vec{\phi}_2}$ stand for the probability distributions for a pair of independent replica fields, $(\vec{\phi}_1, \vec{\phi}_2)$. For simplicity, we represent $(\mathbb{I} - G_{A,\vec{\phi}_1})(\mathbb{I} - G_{A,\vec{\phi}_2}) + G_{A,\vec{\phi}_1} G_{A,\vec{\phi}_2}$ as $g_A^{\vec{\phi}_1,\vec{\phi}_2}$, call it the Grover matrix, and refer to its determinant as the Grover estimator.

In practice, $\exp[-S_2(\rho_A)]$ can be computed in AFQMC using the so-called Grover algorithm, wherein the Grover estimator is sampled across two copies of the system using the joint probability distribution function $P_{\vec{\phi}_1} P_{\vec{\phi}_2}$. A significant advantage of Grover's algorithm is that it requires no additional technical components beyond AFQMC, as the probability distribution $P_{\vec{\phi}}$ and Green's function G_A are identical to those used in the standard AFQMC algorithm.

However, it has been found that this independent replica structure can lead to substantial statistical fluctuations[203, 204, 205, 206], as rare pairs of $(\vec{\phi}_1, \vec{\phi}_2)$ often make significant contributions to the computation of Eq.(7.17). Generally, Grover estimator values should fall within the range $(0, 1]$, given that the entanglement entropy is always non-negative, $S_2(\rho_A) \geq 0$. In rare situations, the values of the Grover estimator, $\det g_A^{\vec{\phi}_1, \vec{\phi}_2}$, can exceed 1, resulting in a negative estimation for $S_2(\rho_A)$ after averaging. This phenomenon is demonstrated in the left panel of Fig.7.1. Despite the majority of samples being distributed within $10^{-2} \sim 10^{0}$, two rare samples near the right end of the sampling path show extremely high values (10^{2-3}) and significantly elevate the sample average of the Grover estimator (red dashed line) above 1, causing the estimation of $S_2(\rho_A)$ to be unphysically negative.

To gain an intuitive understanding of this signal-to-noise issue, it helps to examine the joint distribution $P_{\vec{\phi}_1} P_{\vec{\phi}_2}$. In the case of the continuous Hubbard-Stratonovich transform, Eq.(2.21), $P_{\vec{\phi}}$ follows a multivariate Gaussian distribution, $\mathcal{N}(0, \mathbf{\Gamma})$. Consequently, the joint distribution is a product of Gaussians and aligns with a χ-distribution, which has a much heavier tail than a normal distribution. Therefore, in the process of replica sampling, the likelihood of encountering rare events with large, unphysical estimator values increases, leading to the destabilization of the measurement process.

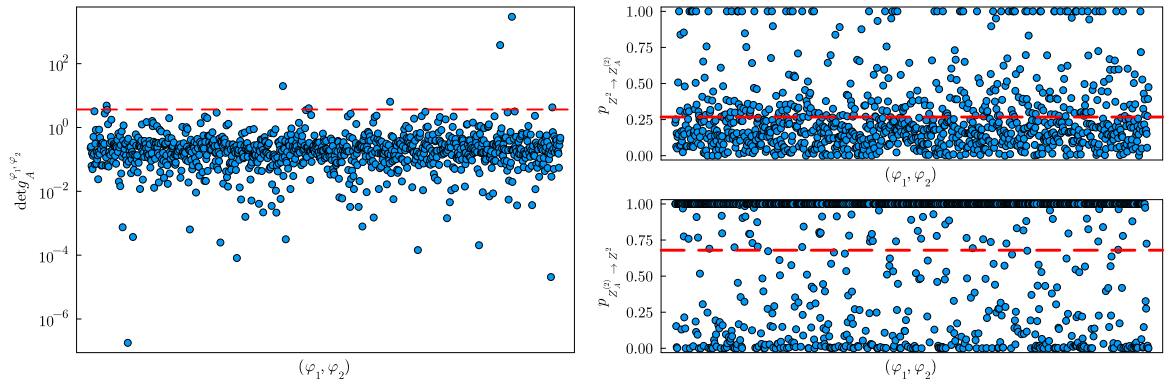

Figure 7.1: Distributions of 1000 AFQMC samples as employed in Grover's algorithm (left panel) and the swap algorithm (right panel). The horizontal axis symbolizes an abstract collection of pairs of auxiliary fields that form a replica sampling path. In the left panel, the vertical axis denotes Grover's estimator, $\det g_A^{\phi_1,\phi_2} = \langle \exp(-S_2(\rho_A)) \rangle_{\phi_1,\phi_2}$, while the two vertical axes on the right panel correspond to the transition probabilities as defined in Eqs.(7.21) and (7.23). The red dashed lines indicate the average sample values of the estimators.

7.3 The Swap Algorithm

To mitigate this statistical issue, it becomes necessary to establish an explicit correlation between replicas in order to suppress the tail distribution such that rare configurations with large statistical weights occur less frequently. The swap algorithm, initially proposed in Variational Monte Carlo (VMC)[184] and Path Integral Monte Carlo (PIMC)[185], is one way to achieve this replica correlation. The key idea behind the swap algorithm is to augment the replica MC sampling process with "swap" moves as illustrated in Fig.7.2a, which exchange the configurations between the two replicas in the entangled region. These "swap" moves help in mixing the configurations from two different replicas, resulting in a more uniform sampling over the space of configuration pairs and therefore leading to a lower variance.

While originally formulated in real space QMC, Trebst *et al.*[113, 147] first expanded the "swap" moves into the abstract auxiliary-field space by constructing an ensemble that "glues" together the entangled region of the two replicas shown in Fig.7.2b. This technique provided a stable method for computing the Renyi entanglement entropy using AFQMC.

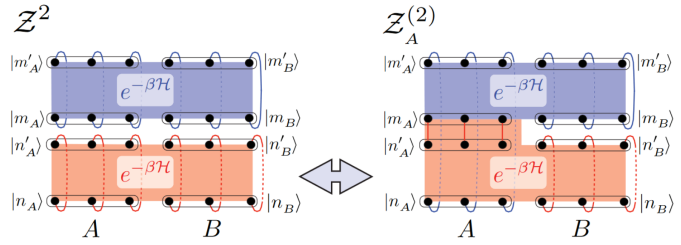

(a) Two replicas are shown as the blue/red regions, respectively. After a swap move, the entangled regions (marked as A) within both replicas are concatenated in such a way that the propagation in imaginary time proceeds across the replicas. This figure is adapted from Ref.[185].

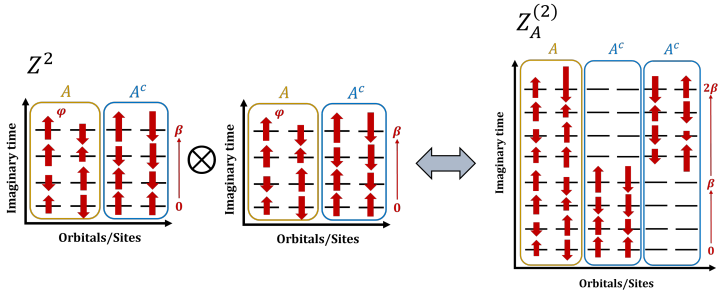

(b) The Hilbert space in the right part is artificially enlarged to represent the real-space concatenation shown in PIMC (above figure). The Hamiltonian vanishes in the regions with no auxiliary fields.

Figure 7.2: Illustration of the swap algorithm as implemented in PIMC (upper panel) and in AFQMC (lower panel). In each panel, the left portion represents the ensemble of two independent replicas with the partition function Z^2. The right portion represents the "glued" ensemble with the partition function $Z_A^{(2)}$. In both figures, A refers to the subsystem of interest (the entangled region), while B/A^c represents the rest of the system. The arrow moving left-to-right signifies the "swap" move between the two ensembles.

Here, a real-space configuration swap is replaced by a swap between the ensembles of two independent replicas and the "glued" ensemble. However, this method comes with a cost: it expands the size of the simulated Hilbert space to $|\mathcal{H}_A^{(2)}| = N_A + 2N_{A^c}$[148], making simulations more resource-intensive as the replica sampling in the enlarged Hilbert space scales as $\mathcal{O}((N_A + 2N_{A^c})^3)$.

In this section, we present a new approach we have developed to implement the swap algorithm in AFQMC without the need to manually enlarge the simulated Hilbert space as in Fig.7.2b. This technique typically achieves a speedup of 3 to 6 times. The first step

is to rewrite Equation (7.17) by expressing the joint probability distribution $P_{\vec{\phi}1}P_{\vec{\phi}_2}$ in terms of ratios of partition functions, $P_{\vec{\phi}1}P_{\vec{\phi}_2} = Z(\vec{\phi}_1)Z(\vec{\phi}_2)/Z^2$,

$$\exp[-S_2(\rho_A)] = \frac{Z_A^{(2)}}{Z^2} = \frac{\int \mathcal{D}\vec{\phi}_1\mathcal{D}\vec{\phi}_2 Z(\vec{\phi}_1)Z(\vec{\phi}_2)\det\left(g_A^{\vec{\phi}_1,\vec{\phi}_2}\right)}{Z^2}. \tag{7.18}$$

Here, the partition function of the "glued" ensemble can be explicitly expressed as two standard partition functions multiplied by the Grover estimator

$$Z_A^{(2)} = \int \mathcal{D}\vec{\phi}_1\mathcal{D}\vec{\phi}_2 Z(\vec{\phi}_1)Z(\vec{\phi}_2)\det\left(g_A^{\vec{\phi}_1,\vec{\phi}_2}\right). \tag{7.19}$$

The ratio in Eq.(7.18) can be calculated by conducting two separate simulations in the independent replica ensemble and in the "glued" ensemble, respectively. In the independent replica ensemble, the Metropolis acceptance ratio is of the usual form

$$R = \frac{Z(\vec{\phi'}_1)}{Z(\vec{\phi}_1)} \text{ or } R = \frac{Z(\vec{\phi'}_2)}{Z(\vec{\phi}_2)}, \tag{7.20}$$

and, in the measurement steps, we measure the transition probability from the current ensemble to the "glued" ensemble

$$p_{Z^2\to Z_A^{(2)}}(\vec{\phi}_1,\vec{\phi}_2) = \min(1, \frac{Z_A^{(2)}(\vec{\phi}_1,\vec{\phi}_2)}{Z(\vec{\phi}_1)Z(\vec{\phi}_2)}). \tag{7.21}$$

While in the "glued" ensemble, the Metropolis acceptance ratio is given by

$$R = \frac{Z(\vec{\phi'}_1)\det\left(g_A^{\vec{\phi'}_1,\vec{\phi}_2}\right)}{Z(\vec{\phi}_1)\det\left(g_A^{\vec{\phi}_1,\vec{\phi}_2}\right)} \text{ or } R = \frac{Z(\vec{\phi'}_2)\det\left(g_A^{\vec{\phi}_1,\vec{\phi'}_2}\right)}{Z(\vec{\phi}_2)\det\left(g_A^{\vec{\phi}_1,\vec{\phi}_2}\right)} \tag{7.22}$$

and then the transition probability to the independent replica ensemble is measured as

$$p_{Z_A^{(2)}\to Z^2}(\vec{\phi}_1,\vec{\phi}_2) = \min(1, \frac{Z(\vec{\phi}_1)Z(\vec{\phi}_2)}{Z_A^{(2)}(\vec{\phi}_1,\vec{\phi}_2)}). \tag{7.23}$$

Hence, $S_2(\rho_A)$ can be estimated as the ratio of two transition probabilities averaged in their respective ensembles

$$\begin{aligned}
\frac{\langle p_{Z^2\to Z_A^{(2)}}\rangle_{Z^2}}{\langle p_{Z_A^{(2)}\to Z^2}\rangle_{Z_A^{(2)}}} &= \frac{\frac{1}{Z^2}\int_{\vec{\phi}_1,\vec{\phi}_2}[\sum_{\frac{Z(\vec{\phi_1})Z(\vec{\phi_2})}{Z_A^{(2)}(\vec{\phi}_1,\vec{\phi}_2)}<1} Z_A^{(2)}(\vec{\phi}_1,\vec{\phi}_2)+\sum_{\frac{Z(\vec{\phi_1})Z(\vec{\phi_2})}{Z_A^{(2)}(\vec{\phi}_1,\vec{\phi}_2)}\geq 1} Z(\vec{\phi}_1)Z(\vec{\phi}_2)]}{\frac{1}{Z_A^{(2)}}\int_{\vec{\phi}_1,\vec{\phi}_2}[\sum_{\frac{Z(\vec{\phi_1})Z(\vec{\phi_2})}{Z_A^{(2)}(\vec{\phi}_1,\vec{\phi}_2)}\geq 1} Z(\vec{\phi}_1)Z(\vec{\phi}_2)+\sum_{\frac{Z(\vec{\phi_1})Z(\vec{\phi_2})}{Z_A^{(2)}(\vec{\phi}_1,\vec{\phi}_2)}<1} Z_A^{(2)}(\vec{\phi}_1,\vec{\phi}_2)]} \\
&= \frac{Z_A^{(2)}}{Z^2} = \exp[-S_2(\rho_A)]. \qquad (7.24)
\end{aligned}$$

It is important to note that the new swap algorithm shares the same scaling as traditional AFQMC, $\mathcal{O}((N_A+N_{A^c})^3)=\mathcal{O}(N^3)$. This results in a reduction in simulation time when compared to the original swap algorithm, which scales as $\mathcal{O}((N_A+2N_{A^c})^3)$. When the system is equally partitioned, with $N_A=N_{A^c}=N/2$, the speedup is $(\frac{N_A+2N_{A^c}}{N_A+N_{A^c}})^3=3.375$. This speedup becomes even more significant when the subsystem's size is smaller. For instance, when $N_A=N/4$, the speedup increases to 5.36.

Given that the transition probabilities computed in Eqs.(7.21) and (7.23) are strictly confined to the range $[0,1]$, the measurements for any rare configuration pairs that might be problematic in Grover's algorithm are capped at a maximum of 1 when mapped to the swap algorithm. As depicted in the left panel of Figure 7.1, the distribution of transition probabilities is bounded within the $[0,1]$ range, ensuring the robustness of the average values. Therefore, the swap algorithm has a lower variance and is more stable compared to Grover's algorithm, making it a preferred choice for computing the entanglement entropy in QMC simulations.

7.4 Resolving Symmetries: Revisiting the Recursive AFQMC Algorithm

In this section, we discuss how to generalize the Recursive AFQMC formalism introduced in Part I to compute the accessible entanglement entropy in the $\alpha = 2$ case

$$S_2^{\text{acc}}(\rho_A) = S_2(\rho_A) - H_{1/2}(\{P_{n,2}\}), \tag{7.25}$$

with

$$\begin{aligned} H_{1/2}(\{P_{n,2}\}) &= 2\ln \sum_n (P_{n,2})^{1/2}, & (7.26)\\ P_{n,2} &= \frac{\text{tr}[\Pi_{A_n}\rho_A^2\Pi_{A_n}]}{\text{tr}\,\rho_A^2}. & (7.27) \end{aligned}$$

Given that we have already covered methods for calculating $S_2(\rho_A)$ in Section 7.3, we now only require the probability distribution $P_{n,2}$. This will enable us to obtain the generalized Shannon entropy and subsequently, the accessible entropy. To resolve this probability distribution, we first rewrite Eq.(7.27) as a ratio of two partition functions

$$P_{n,2} := \frac{Z_{A_n}^{(2)}}{Z_A^{(2)}}, \tag{7.28}$$

where $Z_A^{(2)}$ is the partition function of the "glued" ensemble introduced in Section 7.3, and $Z_{A_n}^{(2)}$ is defined as the normalization for the squared reduced density matrix projected onto the n-particle symmetry sector, such that

$$\text{tr}\big[\Pi_{A_n}\rho_A^2\Pi_{A_n}\big] = \frac{Z_{A_n}^{(2)}}{Z^2}. \tag{7.29}$$

Assume that there exists an auxiliary-field decomposition for this normalization: $Z^{(2)}_{A_n} = \int \mathcal{D}\vec{\phi}_1 \mathcal{D}\vec{\phi}_2 Z^{(2)}_{A_n}(\vec{\phi}_1, \vec{\phi}_2)$, Eq.(7.28) can also be expressed in terms of auxiliary-fields

$$\begin{aligned} P_{n,2} &= \frac{1}{Z^{(2)}_A} \int \mathcal{D}\vec{\phi}_1 \mathcal{D}\vec{\phi}_2 Z^{(2)}_{A_n}(\vec{\phi}_1, \vec{\phi}_2) \\ &= \frac{1}{Z^{(2)}_A} \int \mathcal{D}\vec{\phi}_1 \mathcal{D}\vec{\phi}_2 \frac{Z^{(2)}_{A_n}(\vec{\phi}_1, \vec{\phi}_2)}{Z^{(2)}_A(\vec{\phi}_1, \vec{\phi}_2)} Z^{(2)}_A(\vec{\phi}_1, \vec{\phi}_2) \end{aligned} \tag{7.30}$$

which enables QMC sampling via the estimator

$$\langle P_{n,2}(\vec{\phi}_1, \vec{\phi}_2) \rangle_{Z^{(2)}_A} = \langle \frac{Z^{(2)}_{A_n}(\vec{\phi}_1, \vec{\phi}_2)}{Z^{(2)}_A(\vec{\phi}_1, \vec{\phi}_2)} \rangle_{Z^{(2)}_A}. \tag{7.31}$$

Although Eq.(7.19) gives the expression for $Z^{(2)}_A(\vec{\phi}_1, \vec{\phi}_2)$, the expression for $Z^{(2)}_{A_n}(\vec{\phi}_1, \vec{\phi}_2)$ is difficult to derive, which makes the $P_{n,2}$ estimator less useful. However, if there exists a pseudo-Hamiltonian such that $Z^{(2)}_A(\vec{\phi}_1, \vec{\phi}_2)$ and $Z^{(2)}_{A_n}(\vec{\phi}_1, \vec{\phi}_2)$ can be viewed as the partition functions of this Hamiltonian in the grand canonical ensemble with $\mu = 0$ and in the canonical ensemble with n particles, respectively, all the canonical ensemble formalism developed in the Recursive AFQMC can be mathematically viable for evaluating Eq.(7.31). To find this pseudo-Hamiltonian, we first write down the auxiliary-field decomposition for the squared reduced density matrix, ρ^2_A, using Eqs.(7.15) and (7.17):

$$\rho^2_A = \int \mathcal{D}\vec{\phi}_1 \mathcal{D}\vec{\phi}_2 \det\Big(\mathbb{I} - G_{A,\vec{\phi}_1}\Big) \det\Big(\mathbb{I} - G_{A,\vec{\phi}_2}\Big) e^{\hat{c}^\dagger \ln\Big[(G^{-1}_{A,\vec{\phi}_1} - \mathbb{I})(G^{-1}_{A,\vec{\phi}_2} - \mathbb{I})\Big] \hat{c}}, \tag{7.32}$$

and an entanglement Hamiltonian can therefore be defined as

$$\hat{H}^{(2)}_A(\vec{\phi}_1, \vec{\phi}_2) = \hat{c}^\dagger \ln\Big[(G^{-1}_{A,\vec{\phi}_1} - \mathbb{I})(G^{-1}_{A,\vec{\phi}_2} - \mathbb{I})\Big] \hat{c} \tag{7.33}$$

to serve this purpose. Since $\hat{H}^{(2)}_A(\vec{\phi}_1, \vec{\phi}_2)$ is a one-body operator, it can be easily diagonalized to obtain an "entanglement spectrum", $\{\epsilon^{(2)}_A(\vec{\phi}_1, \vec{\phi}_2)\}$. By denoting the ith eigenvalue

$e^{-\epsilon^{(2)}_{A,i}(\vec{\phi}_1,\vec{\phi}_2)}$ as λ_i, we can recursively compute $P_{n,2}(\vec{\phi}_1,\vec{\phi}_2)$ using Eq.(3.16) by setting $\mu = 0$:

$$P_{n,2}(\vec{\phi}_1,\vec{\phi}_2) = p_i P^{\{\lambda\}\backslash\lambda_i}_{n-1,2}(\vec{\phi}_1,\vec{\phi}_2) + (1-p_i)P^{\{\lambda\}\backslash\lambda_i}_{n,2}(\vec{\phi}_1,\vec{\phi}_2), \tag{7.34}$$

with $p_i = \lambda_i/(1+\lambda_i)$. Hence, following Eq.(7.31), we can estimate the probability distribution as Eq.(7.34) in each measurement step when we sample in the "glued" ensemble space using the weight function $Z^{(2)}_A(\vec{\phi}_1,\vec{\phi}_2)$, the statistical average of which provides an estimate[2] for the Shannon Entropy $H_{1/2}(\{P_{n,2}\})$ and the accessible entropy $S^{\mathrm{acc}}_2(\rho_A)$.

We note that Eqs.(7.33) and (7.34) only hold in the ground state or in the grand canonical ensemble at finite temperature. In the canonical ensemble, one has to first project the total particle number to N from the grand canonical ensemble, then project the local particle number to n. The form of the entanglement Hamiltonian is therefore different, which also leads to a different recursive formula. As we only focus on ground state applications in Part II, the explicit canonical ensemble formulas are not included in this section. Interested readers can refer to Appendix D for a detailed illustration.

In summary, Recursive AFQMC combined with the swap algorithm gives access to the Rényi-2 entanglement entropy and its symmetry-resolved forms in two parallel simulations. The workflow of the algorithm is:

- Conduct the simulation in the replica ensemble space specified by the partition function Z^2. Initialize two random walkers with auxiliary-field configurations $\vec{\phi}_1$ and $\vec{\phi}_2$, respectively.

    1. Update the field $\vec{\phi}_1$ multiple times using the acceptance ratio $r = \min(1, \frac{Z(\vec{\phi}'_1)}{Z(\vec{\phi}_1)})$, while $\vec{\phi}_2$ is kept unchanged. After some time, switch to the field $\vec{\phi}_2$.

    2. Spend the same amount of time as in step 1 updating $\vec{\phi}_2$, using the acceptance ratio $r = \min(1, \frac{Z(\vec{\phi}'_2)}{Z(\vec{\phi}_2)})$, $\vec{\phi}_1$ is kept unchanged. Switch to the field $\vec{\phi}_1$ in the end.

[2] A Jackknife[207] or bootstrap resampling[207] has to be performed to yield an unbiased estimation

3. Repeat Steps 1 and 2 $100 \sim 1000$ times to thermalize the walkers. After equilibrium is reached, measure the transition probability $p_{Z^2 \to Z_A^{(2)}}$ as in Eq.(7.21) at the end of Step 2.

- Conduct in parallel another simulation in the replica ensemble space specified by the partition function $Z_A^{(2)}$. Initialize two random walkers with auxiliary-field configurations $\vec{\phi}_1$ and $\vec{\phi}_2$, respectively.

  1. Update the field $\vec{\phi}_1$ multiple times using the acceptance ratio $r = \min(1, \frac{Z(\vec{\phi'}_1) \det g_A^{\vec{\phi'}_1, \vec{\phi}_2}}{Z(\vec{\phi}_1) \det g_A^{\vec{\phi}_1, \vec{\phi}_2}})$. $\vec{\phi}_2$ is kept unchanged. After some time, switch to the field $\vec{\phi}_2$.

  2. Spend the same amount of time as in step 1 updating $\vec{\phi}_2$, using the acceptance ratio $r = \min(1, \frac{Z(\vec{\phi}'_2) \det g_A^{\vec{\phi}_1, \vec{\phi}'_2}}{Z(\vec{\phi}_2) \det g_A^{\vec{\phi}_1, \vec{\phi}_2}})$. $\vec{\phi}_1$ is kept unchanged. Switch to the field $\vec{\phi}_1$ in the end.

  3. Repeat Steps 1 and 2 $100 \sim 1000$ times to thermalize the walkers. After equilibrium is reached, measure the transition probability $p_{Z_A^{(2)} \to Z^2}$ and the probability distribution $P_{n,2}$ as in Eqs.(7.23) and (7.31), respectively, at the end of Step 2.

- Gather the statistical averages $\left\langle p_{Z^2 \to Z_A^{(2)}} \right\rangle$, $\left\langle p_{Z_A^{(2)} \to Z^2} \right\rangle$ and $\langle P_{n,2} \rangle$. Then, use the Jackknife resampling scheme to compute the unbiased estimate for $S_2(\rho_A)$ and $S_2^{\text{acc}}(\rho_A)$ as per Eqs.(7.24) and (7.25), respectively.

CHAPTER 8

Results and Discussions

8.1 Introduction

After deriving a theoretical formalism for measuring these entanglements for interacting fermions, we use two paradigmatic spinful fermion models to showcase the increased resolution and detail entanglement measures provide and compare these with more conventional, local observables. The additional spin degrees of freedom in spinful models introduce spin conservation into the system, along with the conservation of charge (particle number), enabling us to conduct two types of symmetry resolutions in our accessible entanglement measurements, specifically the charge-resolved and spin-resolved accessible entanglement entropies

$$S_{2,n}^{\mathrm{acc}}(\rho_A) = S_2(\rho_A) - 2\ln\sum_n (P_{n,2})^{1/2}, \tag{8.1}$$

$$S_{2,m}^{\mathrm{acc}}(\rho_A) = S_2(\rho_A) - 2\ln\sum_n (P_{m,2})^{1/2}. \tag{8.2}$$

Here, the local charge and spin number can be obtained by measuring local spin-up and spin-down electron numbers: $n = n_{A,\uparrow} + n_{A,\downarrow}$ and $m = n_{A,\uparrow} - n_{A,\downarrow}$. Since two spin species factorize after the Hubbard-Stratonovich transformation, $n_{A,\uparrow}$ and $n_{A,\downarrow}$ are

counted separately in the measurement step, making the evaluation of Eqs.(8.1) and (8.2) a post-measurement data processing. Our workflow is thus unchanged by including spins.

In Section 8.2, we use the bilayer Hubbard model to study the transition between the antiferromagnetic (Mott insulator) and band insulator phases. We apply an entanglement perspective o this elementary phase diagram to the bilayer Hubbard model and compare the results to a local observable measuring the bond strength between its two layers. Our comparison suggests that entanglement measures offer sharper signals near the critical point and are less affected by finite-size effects. Moving on to Section 8.2, we analyze the Su–Schrieffer–Heeger-Hubbard (SSHH) model, the simplest model exhibiting symmetry-protected topological order (SPT). Here, we evaluate both the accessible topological entanglement entropy and the standard topological entanglement entropy. This parallel evaluation underscores the additional resolution that accessible entropy provides, particularly in detecting different topological orders. This aspect suggests the unique contribution and value that accessible entanglement measures bring to our understanding of complex quantum phenomena.

8.2 Probing Phase Transitions and Crossovers

The bilayer Hubbard model, in essence, represents two interacting layers of a square lattice. Each layer is an instance of the single-layer Hubbard model whose Hamiltonian is shown in Eq.(4.1). The overall Hamiltonian then reads

$$\hat{H} = -t \sum_{\langle i,j\rangle,\sigma} \left(\hat{c}^{\dagger}_{i,\sigma}\hat{c}_{j,\sigma} + \text{H.c.}\right) - t_{\perp} \sum_{i,i',\sigma} \left(\hat{c}^{\dagger}_{i,\sigma}\hat{c}_{i',\sigma} + \text{H.c.}\right) + U \sum_{i} \hat{n}_{i,\uparrow}\hat{n}_{i,\downarrow}, \tag{8.3}$$

which describes the competition between conventional band structures arising from the $U = 0$ tight-binding lattice model that is parametrized by hopping amplitudes t and $t_{\perp}$, and Mott physics arising from an on-site Coulomb repulsion U. Here, $\langle i, j\rangle$ denotes a pair of the nearest sites in the same layer, while i, i' represents two sites from different layers

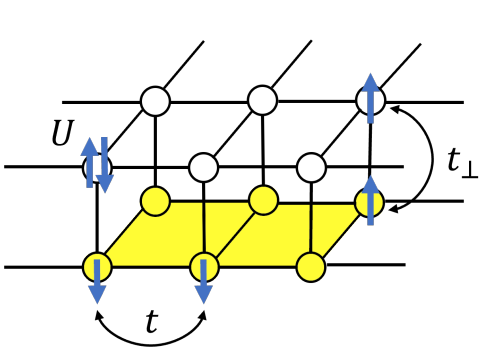

(a) To study entanglement properties, the lattice is partitioned into two layers where the lower layer is the subsystem of interest (yellow region).

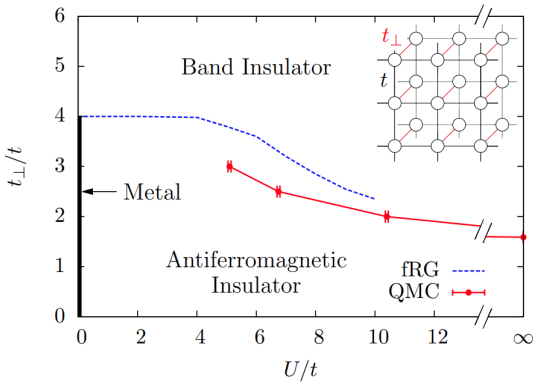

(b) Ground state phase diagram of the bilayer Hubbard model at half filling, adapted from functional renormalization (fRG) group calculations[208].

Figure 8.1: Illustration of the bilayer Hubbard model. Three types of interactions are labeled within the figure: intralayer hopping (t), interlayer hopping ($t_\perp$), and on-site repulsion (U). Electrons with up and down spins are depicted by blue arrows.

connected by interlayer bonds with strength $t_\perp$.

Fig.8.1 provides a schematic phase diagram for this model, mapping out the relationship between the on-site interaction U and interlayer hopping $t_\perp$. When the interlayer hopping strength $t_\perp$ is very large, irrespective of the U value, the system turns into a featureless band insulator as a result of the band gap opening. Conversely, when U is sufficiently large and interlayer hopping $t_\perp$ is small, the system transforms into a Mott insulator with an antiferromagnetic order. In the weak coupling regime ($U/t < 4$), the transition into the band insulator phase takes place when $t_\perp$ is approximately equal to $4t$. The critical value of $t_\perp$ gradually decreases to $t_\perp = 1.588t$ as $U \to \infty$, at which the system can be described by a spin-1/2 Heisenberg model[209, 210].

We conduct our Recursive AFQMC simulation on a medium-sized $6 \times 6 \times 2$ half-filled model and go deep into the strong coupling region at $U = 6t$. To carry out entanglement measures, we considered a subsystem of a single layer with size $6 \times 6 \times 1$, as depicted in the left panel of Fig.8.1. The simulation is conducted at $\beta = 18$ where the convergence is reached. Fig.8.2 presents our simulation results, with the left panel illustrating the

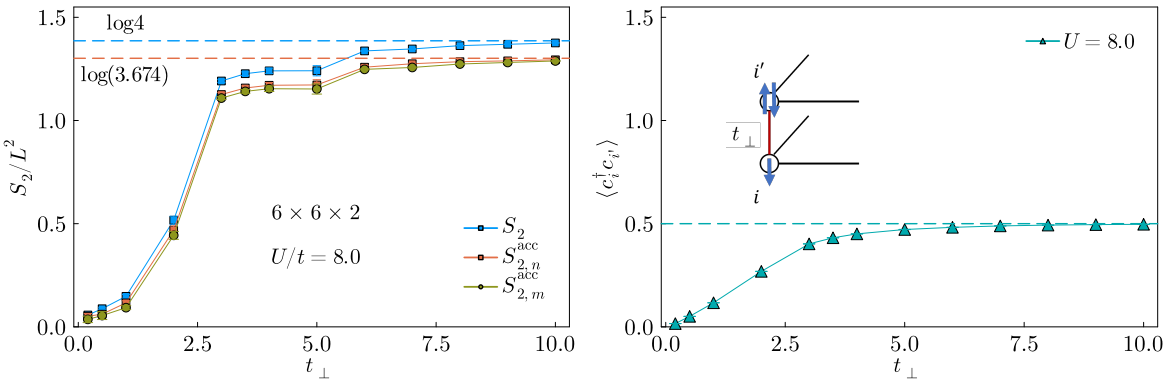

Figure 8.2: QMC simulation of a $6 \times 6 \times 2$ half-filled bilayer Hubbard model at $U = 8t$. Left panel: Entanglement entropies with a horizontal cut for the bipartition. The blue, red, and green curves correspond to the Rényi-2, charge-resolved, and spin-resolved entropies, respectively. The blue and red dashed lines represent the asymptotic values for the Rényi-2 and accessible entropies in the limit $t_\perp \to \infty$. Right panel: Interlayer bond strength (red bond in the inset figure), $\langle \hat{c}_i^\dagger \hat{c}_{i'} \rangle$, measured at different values of $t_\perp$. The y-axis is set to the same as the left panel for better comparison. The dashed line indicates its value when $t_\perp$ approaches infinity.

Rényi-2 entropy, charge-resolved and spin-resolved accessible entropies normalized by the size of the subsystem, L^2, across a wide range of $t_\perp \in [0, 10.0]$. Clearly, two distinct regimes can be readily distinguished by a sharp rise in the values of all three types of entanglement entropies. In the Mott insulator phase, weak interlayer hopping and strong on-site repulsion (U) largely restrict electrons to their local sites, inhibiting their movement across layers. This limitation results in relatively low entanglement entropies. Conversely, in the band insulator region, the effect of interlayer hopping surpasses the on-site repulsion, which leads to the formation of singlet dimers on the rungs between layers. Active interlayer hopping of electrons then produces large amounts of entanglement as can be seen in the $t_\perp > 5t$ regime of the left panel of Fig.8.2. It is interesting to observe that the sudden jump at $t_\perp \approx 2.5t$ in all three entanglement entropies signals the phase transition, which is in accordance with the functional RG prediction at $U = 8t$ in Fig.8.1.

In the right panel of Fig.8.2, we compare our findings with local observables by measuring the interlayer bond strength, $\langle \hat{c}_i^\dagger \hat{c}_{i'} \rangle$. This value is averaged over all sites in the lower layer, across the same range of $t_\perp$ values. Notably, the local observable demonstrates

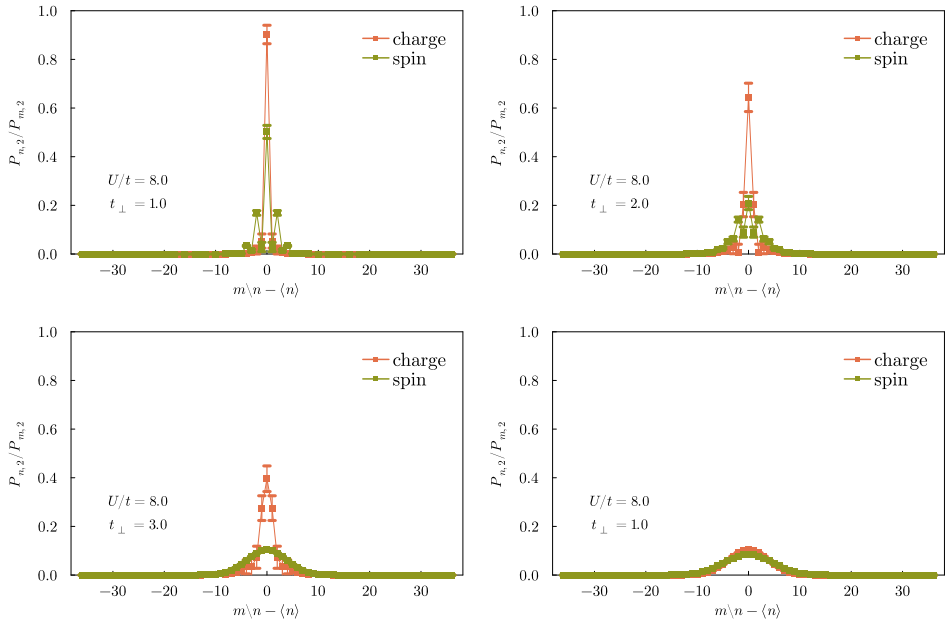

Figure 8.3: Charge and spin probability distributions measured at different $t_\perp$ values. For the spin distribution, the x-axis is the total spin of a single layer whose range is $[-36, 36]$. While for the charge distribution, the x-axis is the deviation of the mean particle number of a single layer, $\langle n \rangle = 36$.

a much weaker response to the phase transition compared to the entanglement entropies. This can be attributed to the fact that two-point correlations require a larger system size to detect the abrupt increase in correlation length at the critical point, while entanglement entropy inherently encodes global information to better capture changes in the correlation length. Consequently, entanglement entropy can sharply signal the phase transition even at relatively small system sizes, potentially reducing the need for extrapolation to the thermodynamic limit.

Lastly, we note that the accessible entropies behave almost the same as the Rényi-2 entropy. It is because, in a three-dimensional system, the configurational entanglement grows much faster than the number fluctuations. Despite this, we can still gain some extra insights by examining the charge and spin probability distributions. The charge and spin distributions are depicted for four different $t_\perp$ values in Fig.8.3. In the Mott insulating phase, there is a pronounced even-odd effect at lower $t_\perp$ values. This arises from the fact that, while the double occupation is strongly suppressed (as evidenced by the

strong, singular peaks in the charge distribution), a pair of electrons with different spins can swap positions across layers, thereby altering the total spin in a single layer by ± 2. This is represented by the peaks at even numbers in the spin distribution. The sudden vanishing of these sub-peaks after the phase transition, as shown in the $t_\perp = 3$ figure, provides complementary and supporting information that aligns with the entanglement measures in Fig.8.2.

8.3 Topological Properties Revealed by Entanglement

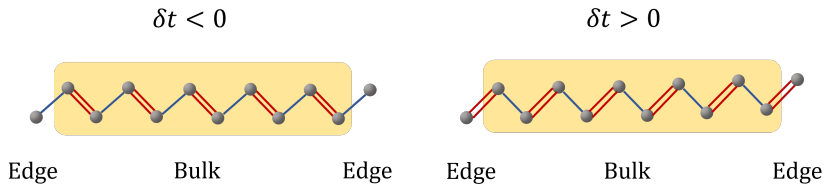

Figure 8.4: Schematic figure of the SSH model with open boundary conditions (OBC). In the $\delta t < 0$ case, two edge sites are connected to the bulk (yellow region) through a weak bond, while in the $\delta t > 0$ case, edge sites connect to the bulk via a strong bond.

In this section, we showcase how accessible entanglement can behave significantly differently from the standard entanglement entropy, by applying the entanglement measures to the 1D SSH model with open boundary conditions, which combines the famous Su-Schrieffer-Heeger (SSH) model with the Hubbard-type many-body interaction. The Hamiltonian of the 1D SSH model is

$$H = -\sum_i [t + (-1)^i \delta t](c_i^\dagger c_{i+1} + \text{h.c.}) + U \sum_i n_{i\uparrow} n_{i\downarrow}, \tag{8.4}$$

where the first term is the SSH term, which is well known for demonstrating the topological nature of solitons in polyacetylene[211], represented by a chain with alternating coupling strengths, and the second term is the usual on-site repulsion. This model system is designed to explore the intricate interplay between electron correlation effects (from the

Hubbard term) and topological order (from the SSH term).

The topological insulator phase in the SSH model arises in the $\delta t < 0$ cases as is depicted in the left panel of Fig.8.4, where two edges are linked to the bulk of the chain through weak bonds. In such cases, electrons of the bulk sites are dimerized, which leads to a topologically non-trivial phase characterized by the presence of zero-energy edge states[212]. This edge state is protected by inversion symmetry and is thus robust against small perturbations.

Since the transition from a topologically trivial phase ($\delta t > 0$) to a topological insulator phase ($\delta t < 0$) does not fall into the traditional symmetry-breaking framework, it cannot be described using local order parameters. One effective approach to identify this topological order is through the use of the topological entanglement entropy (TEE)[166, 213], a concept that relates to the inherent "long-range" entanglement within topologically ordered states. In the SSH model, such long-range entangled topological order manifests as a subleading term in the scaling law for the entanglement entropy[166, 214]:

$$S_{2,\mathrm{OBC}}(\rho_A) = \alpha L + S_{2,\mathrm{edge}} + \cdots . \tag{8.5}$$

Here, α is a nonuniversal coefficient arising from short-range entanglements localized near the boundary [215], and $S_{2,\mathrm{edge}}$ is related to the ground state degeneracy $\mathcal{D}$ on one open end as $\lim_{L\to\infty} S_{2,\mathrm{edge}} = \ln \mathcal{D}$. To extract this subleading term, one needs to remove the leading short-range entanglement that follows the boundary law. It is achieved by using an auxiliary SSH chain under periodic boundary conditions (PBC), where no edge states exist as the chain is closed as a loop. As a result, its entanglement entropy scales as $S_{2,\mathrm{PBC}} \approx 2\alpha L$. The TEE can then be extracted as[214]

$$S_{2,\mathrm{edge}}(\rho_A) = S_{2,\mathrm{OBC}}(\rho_A) - \frac{S_{2,\mathrm{PBC}}(\rho_A)}{2}. \tag{8.6}$$

Consequently, we can define the accessible topological entanglement entropy with charge

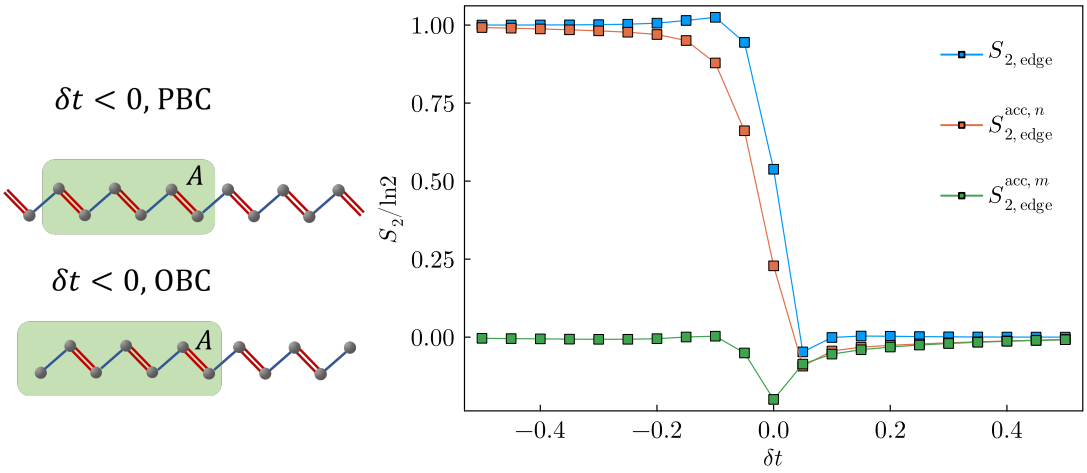

Figure 8.5: Left panel: Bipartitions of the chain for extracting the topological edge entanglement at $\delta t < 0$. For periodic boundary conditions, the site indices of the subsystem are $[2, 3, \cdots, L/2{+}1]$, and for open boundary conditions, the subsystem consists of the sites with indices $[1, 2, \cdots, L/2 + 1]$. Right Panel: Topological edge entanglement entropies for the $L = 12$ SSH model at $U = 4$. The blue, red, and green curves correspond to the Rényi-2, charge-resolved, and spin-resolved topological entanglement entropies, respectively.

and spin resolution respectively as

$$S^{\mathrm{acc},n}_{2,\mathrm{edge}}(\rho_A) = S^{\mathrm{acc},n}_{2,\mathrm{OBC}}(\rho_A) - \frac{S^{\mathrm{acc},n}_{2,\mathrm{PBC}}(\rho_A)}{2} \tag{8.7}$$

and

$$S^{\mathrm{acc},m}_{2,\mathrm{edge}}(\rho_A) = S^{\mathrm{acc},m}_{2,\mathrm{OBC}}(\rho_A) - \frac{S^{\mathrm{acc},m}_{2,\mathrm{PBC}}(\rho_A)}{2}. \tag{8.8}$$

The right panel of Fig.8.5 depicts the simulated results for topological edge entanglement entropies in the Rényi and accessible forms for the $L = 12$ open SSH chain at $U = 4$. The subsystem is chosen by cutting at the weak bonds of the chain. For cases where $\delta t > 0$, the site indices in subsystem A are the same for two boundary conditions, $[1, 2, \ldots, L/2]$. For $\delta t < 0$, the partition methods are different for PBC and OBC as shown in the left panel of Fig.8.5. All three edge entanglements are almost zero for any $\delta t > 0$ as the phase is topologically trivial and featureless. The edge entanglement entropy exhibits a quantized behavior in the topological insulator phase ($\delta t < 0$) for both its Rényi-2 and

charge-resolved forms, $S_{2,\text{edge}}, S^{\text{acc},n}_{2,\text{edge}} \approx \ln 2$, whereas the values for the spin-resolved edge entanglement remain zero for any $\delta t < 0$. This result can be understood as follows. The edge modes on the left and right ends of the chain are coupled through the bulk and form a degenerate singlet ground state

$$|\psi^{\delta t<0}\rangle = \frac{1}{\sqrt{2}}(\hat{c}^\dagger_{L,\uparrow}\hat{c}^\dagger_{R,\downarrow} - \hat{c}^\dagger_{L,\downarrow}\hat{c}^\dagger_{R,\uparrow})|0\rangle, \tag{8.9}$$

where $\hat{c}^\dagger_{L,\sigma}$ creates an electron with spin σ on the left edge. After tracing out the degrees of freedom on the right edge, we are left with the left edge mode

$$|\psi^{\delta t<0}_L\rangle = \frac{1}{\sqrt{2}}(\hat{c}^\dagger_{L,\uparrow} + \hat{c}^\dagger_{L,\downarrow})|0\rangle, \tag{8.10}$$

which leads to $S_{2,\text{edge}} = 2$. In this left edge mode, the charge distribution behaves like a δ-function as there is only one possible charge number, $P_{n=1,\alpha} = 1$, resulting in a corresponding Shannon entropy of zero. This implies that the topological entanglement is mostly preserved in the charge resolution. Conversely, the spin distribution could have two possible equally distributed values, $P_{m=\pm1,\alpha} = \frac{1}{2}$, which leads the corresponding Shannon entropy to nullify the TEE with $H_{1/2}(P_{m,2}) = \ln 2$. This suggests that the spin distribution has no impact on the edge entanglement.

While we have studied a rather simple model whose topological behavior can be readily analyzed, our findings suggest that symmetry resolutions in the form of accessible TEE can complement the standard TEE. They provide additional insights for analyzing topological orders that the standard method may lack. We anticipate that this concept could be demonstrated in a more sound manner in 2D systems with more complicated electron-electron correlations, such that the competition between topological band structures and correlation physics is not straightforward to analyze. We reserve such explorations for future research.

CHAPTER 9

Conclusions

9.1 Overview

In summary, we have presented the *first* exploration of symmetry-resolved, accessible entanglement measures for fully interacting fermionic systems. This is accomplished by integrating our novel Recursive AFQMC algorithm with the ground state swap algorithm. We first enhanced the efficiency of the swap algorithm by incorporating the Grover estimator into the Monte Carlo update within the algorithm, achieving a milder computational scaling with respect to system size. Subsequently, we utilized the Recursive AFQMC algorithm to explicitly calculate the probability distribution of each symmetry sector in the entangled region, allowing us to resolve probability distribution functions and observables based on symmetry. We derived a workflow that allows for the calculation of all relevant observables via two parallel simulations, with scaling identical to that of the conventional AFQMC algorithm.

We have employed this method on two representative models, namely the bilayer Hubbard model and the Su-Schrieffer-Heeger-Hubbard model. These models manifest conventional and topological phase transitions, respectively, and demonstrate how entanglement measures can serve as a versatile probe for various phase transitions. The

sensitivity of these entanglement measures to the change of correlation length near the critical point is confirmed by comparison with local observables. The distinct behaviors of the charge- and spin-resolved TEEs in a topologically ordered state suggest that they can supplement the information provided by the standard TEE.

9.2 Outlook

While our initial exploration is focused on simpler, demonstrative types of models, our formalism is quite general and does not assume that the system has any specific properties. Therefore, we expect our approach to find more comprehensive applications in a broader range of models. Such models could include those with spin-orbit couplings, where the distinctions between spin and charge resolutions become more pronounced, or two-dimensional topological models that present more complex edge-bulk correspondences. Another promising avenue for future applications is for realistic systems where the sign problem emerges. Here, our method may employ the Constrained Path Quantum Monte Carlo algorithm to eliminate the sign problem, thereby enabling the study of richer physics in realistic systems caused by long-range correlations.

Lastly, it is worthwhile to mention the potential application of accessible entanglement measures as a metric for the concept of decoherence-free subspaces (DFS) in Quantum Information. In general, identifying the symmetries of a given system-environment interaction is a critical step towards discovering and utilizing DFS to protect quantum information from decoherence. Given that the accessible entanglement primarily operates within different symmetry sectors of a subsystem, it could potentially serve to bound the maximum amount of information resistant to certain types of environmental noise.

Appendix A

Detailed Derivation of Partition Functions and Density Matrices in the Canonical Ensemble

In this Appendix, we provide detailed derivations of several recursive relations that are essential to obtaining the partition functions and density matrices for a specific auxiliary field. Some of these equations have been derived in other contexts before[107, 108, 140, 216].

First, we derive Eq.(3.23), which undergirds our expressions for the canonical partition function. Suppose we have an arbitrary $N \times N$ matrix A expressed in the single-particle basis and form two Fock-space operators that operate on boson and fermion Fock states respectively

$$\hat{A}_b = \hat{b}^\dagger A \hat{b}, \tag{A.1}$$

$$\hat{A}_f = \hat{c}^\dagger A \hat{c}. \tag{A.2}$$

We then consider the operations $\hat{A}_b \hat{b}^\dagger$ and $\hat{A}_f \hat{c}^\dagger$. Using the elementary commutation/anticommutation

relations, it is straightforward to show that

$$\begin{aligned}
\hat{A}_b\hat{b}_k^\dagger &= \sum_{ij}\hat{b}_i^\dagger A_{ij}\hat{b}_j\hat{b}_k^\dagger \\
&= \sum_i \hat{b}_i^\dagger A_{ik} + \hat{b}_k^\dagger \sum_{ij}\hat{b}_i^\dagger A_{ij}\hat{b}_j, \qquad \text{(A.3)} \\
\hat{A}_f\hat{c}_k^\dagger &= \sum_{ij}\hat{c}_i^\dagger A_{ij}\hat{c}_j\hat{c}_k^\dagger \\
&= \sum_i \hat{c}_i^\dagger A_{ik} - \sum_{ij}\hat{c}_i^\dagger\hat{c}_k^\dagger A_{ij}\hat{c}_j \\
&= \sum_i \hat{c}_i^\dagger A_{ik} + \hat{c}_k^\dagger \sum_{ij}\hat{c}_i^\dagger A_{ij}\hat{c}_j \qquad \text{(A.4)}
\end{aligned}$$

which gives

$$\begin{aligned}
\hat{A}_b\hat{b}^\dagger &= \hat{b}^\dagger(A + I\hat{A}_b), \qquad \text{(A.5)} \\
\hat{A}_f\hat{c}^\dagger &= \hat{c}^\dagger(A + I\hat{A}_f), \qquad \text{(A.6)}
\end{aligned}$$

where I is the $N \times N$ unit matrix. Note that the elements of the matrices A and I are c numbers in Fock space and $\hat{A}$ is a scalar relative to the $N \times N$ matrices. As a result, $I\hat{A}$ and A commute as matrices. Repeatedly applying these two equations yields

$$\begin{aligned}
\hat{A}_b^n\hat{b}^\dagger &= \hat{b}^\dagger(A + I\hat{A}_b)^n, \qquad \text{(A.7)} \\
\hat{A}_f^n\hat{c}^\dagger &= \hat{c}^\dagger(A + I\hat{A}_f)^n \qquad \text{(A.8)}
\end{aligned}$$

for any positive integer n. Hence,

$$\begin{aligned}
e^{-\hat{A}_b}\hat{b}^\dagger &= \hat{b}^\dagger e^{-(A+I\hat{A}_b)} = \hat{b}^\dagger e^{-A}e^{-\hat{A}_b}, \qquad \text{(A.9)} \\
e^{-\hat{A}_f}\hat{c}^\dagger &= \hat{c}^\dagger e^{-(A+I\hat{A}_f)} = \hat{c}^\dagger e^{-A}e^{-\hat{A}_f} \qquad \text{(A.10)}
\end{aligned}$$

can be shown inductively, where in the last step of both equations, the exponential is allowed to be broken up because the two terms in the exponent commute, as noted above.

These results allow $e^{-\beta\hat{h}(\vec{\phi})}$ in Eq.(3.23) to "walk through" the string of creation operators that defines the N-particle state $|\Gamma\rangle$. More specifically, by expanding $|\Gamma\rangle$ in terms of particle creation operators, we have

$$\begin{aligned} e^{-\hat{h}(\vec{\phi})}|\Gamma\rangle &= e^{-\beta\sum_\gamma \hat{c}_i^\dagger\gamma\epsilon_\gamma(\vec{\phi})\hat{c}\gamma}\prod_\gamma(\hat{c}_i^\dagger\gamma)^{n_\gamma}|0\rangle \\ &= \left[\prod_\gamma(\hat{c}_i^\dagger\gamma e^{-\beta\epsilon_\gamma(\vec{\phi})})^{n_\gamma}\right]e^{-\hat{h}(\vec{\phi})}|0\rangle \\ &= \left[\prod_\gamma(\hat{c}_i^\dagger\gamma e^{-\beta\epsilon_\gamma(\vec{\phi})})^{n_\gamma}\right]|0\rangle, \end{aligned} \tag{A.11}$$

where, in the last step, we have used the fact $e^{-\hat{h}(\vec{\phi})}|0\rangle = |0\rangle$. Thus, sandwiching $e^{-\hat{h}(\vec{\phi})}$ between $\langle\Gamma|$ and $|\Gamma\rangle$ yields

$$\langle\Gamma|e^{-\hat{h}(\vec{\phi})}|\Gamma\rangle = \prod_\gamma e^{-\beta n_\gamma\epsilon_\gamma(\vec{\phi})}, \tag{A.12}$$

which enables us to proceed from the second line to the last line in Eq.(3.23). Notice that Eqs.(A.9) and (A.10) have exactly the same form. As such, Eq.(A.12) holds true for both boson and fermion propagators, as they propagate the corresponding states in the same manner.

Next, we show how to iteratively obtain the mean occupation numbers of the eigenstates, i.e., Eq.(3.29). This is needed to evaluate a system's energy and correlation functions.

Without loss of generality, we consider the $\lambda = 1$ case of Eq.(3.29). By definition,

$$\langle\hat{n}_1\rangle_N = \frac{\sum_{\{n_\lambda\}_1^N} n_1 e^{-\beta\sum_{\gamma=1}^{N_s} n_\gamma\epsilon_\gamma}}{Z_N}, \tag{A.13}$$

where we have introduced the shorthand $\{n_\gamma\}_1^N$ to denote all states that conserve their particle number such that $\sum_{\gamma=1}^{N_s} n_\gamma = N$ and have omitted all field dependence for clarity.

Since n_γ can only be 0 and 1 for fermions, we arrive at the following two identities

$$\sum_{n_\gamma=0,1} n_\gamma e^{-\beta n_\gamma \epsilon_\gamma} = e^{-\beta\epsilon_\gamma} \tag{A.14}$$

$$\sum_{n_\gamma=0,1} (1-n_\gamma) e^{-\beta n_\gamma \epsilon_\gamma} = 1. \tag{A.15}$$

Substituting these identities into Eq.(A.13) yields

$$\begin{aligned} \langle \hat{n}_1 \rangle_N Z_N &= e^{-\beta\epsilon_1} \sum_{\{n_\gamma\}_2^{N-1}}^{n_\gamma=0,1} e^{-\beta \sum_{\gamma=2}^{N_s} n_\gamma \epsilon_\gamma} \\ &= e^{-\beta\epsilon_1} \sum_{\{n_\gamma\}_2^{N-1}}^{n_\gamma=0,1} (1-n_1) e^{-\beta \sum_{\gamma=1}^{N_s} n_\gamma \epsilon_\gamma} \\ &= e^{-\beta\epsilon_1} \langle 1-\hat{n}_1 \rangle_{N-1} Z_{N-1}, \end{aligned} \tag{A.16}$$

which leads to Eq.(3.29) by using the ratio of partition functions given in Eq.(3.17).

Appendix B

Algorithmic Details for Recursive AFQMC Sampling and Propagator Stabilization Techniques

In this Appendix, we provide details regarding how we sample and stabilize our matrices in our new algorithm. To better illustrate how propagators are operated (i.e., multiplied or cyclically permuted) in the implementation, we use the notation $\mathbf{B}^{(\vec{\phi})}_{L-k\Delta\tau}$ for the propagator matrix at time slice $[L-k\Delta\tau, L-(k-1)\Delta\tau]$. Similar to other auxiliary field-based QMC algorithms [47, 50, 56], one needs to take special care multiplying the propagators, $\mathbf{B}^{(\vec{\phi})}_{L}\mathbf{B}^{(\vec{\phi})}_{L-1}\cdots\mathbf{B}^{(\vec{\phi})}_{1}$, used to compute the traces together as directly multiplying the propagators is numerically unstable at low temperatures due to the existence of extremely large and extremely small singular values [54, 84]. In order to circumvent this, QR factorization with column-pivoting is used to separate singular values of different magnitudes for series of $\mathbf{B}^{(\vec{\phi})}$s of length l:

$$\tilde{\mathbf{B}}^{(\tilde{\phi})}_{\mathbf{k}} = \mathbf{B}^{(\tilde{\phi})}_{\mathbf{l+k}}\mathbf{B}^{(\tilde{\phi})}_{\mathbf{l+k-1}}\cdots\mathbf{B}^{(\tilde{\phi})}_{\mathbf{k}} = \mathbf{U}^{(\tilde{\phi})}_{\mathbf{k}}\mathbf{D}^{(\tilde{\phi})}_{\mathbf{k}}\mathbf{T}^{(\tilde{\phi})}_{\mathbf{k}}, \tag{B.1}$$

where $\mathbf{U}_\mathbf{k}^{(\tilde{\phi})}$ is a unitary matrix, $\mathbf{D}_\mathbf{k}^{(\tilde{\phi})}$ is a diagonal matrix whose elements range from very large to very small in magnitude, and $\mathbf{T}_\mathbf{k}^{(\tilde{\phi})}$ is a regular matrix with a small condition number. Matrix multiplications using this factorization turn out to be stable.

The MC sampling proceeds by updating the $\mathbf{B}_\mathbf{i}^{(\tilde{\phi})}$ sequentially. A full update from $i = 1$ to $i = L$ is called a sweep. Before the sweep, we initialize a string of randomly-generated propagator matrices, $\mathbf{B}_\mathbf{L}^{(\tilde{\phi})}\mathbf{B}_\mathbf{L-1}^{(\tilde{\phi})}\cdots\mathbf{B}_\mathbf{1}^{(\tilde{\phi})}$, and compute and store all of the partial factorizations as

$$[\underbrace{\mathbf{U_{n-1}^{(\tilde{\phi})}D_{n-1}^{(\tilde{\phi})}T_{n-1}^{(\tilde{\phi})}}}_{\tilde{\mathbf{B}}_\mathbf{n}^{(\tilde{\phi})}}, \underbrace{\mathbf{U_{n-2}^{(\tilde{\phi})}D_{n-2}^{(\tilde{\phi})}T_{n-2}^{(\tilde{\phi})}}}_{\tilde{\mathbf{B}}_\mathbf{n}^{(\tilde{\phi})}\tilde{\mathbf{B}}_\mathbf{n-1}^{(\tilde{\phi})}}, \ldots, \underbrace{\mathbf{U_1^{(\tilde{\phi})}D_1^{(\tilde{\phi})}T_1^{(\tilde{\phi})}}}_{\tilde{\mathbf{B}}_\mathbf{n}^{(\tilde{\phi})}\cdots\tilde{\mathbf{B}}_\mathbf{2}^{(\tilde{\phi})}}]. \tag{B.2}$$

Here, we denote the total number of groups of matrices as $n = L/l$. When updating the kth group of matrices, $\tilde{\mathbf{B}}_\mathbf{k}^{(\tilde{\phi})}$, in order to reduce the number of QR factorizations, a cyclicly-permuted string of propagator matrices is computed

$$\underbrace{\mathbf{U_L D_L T_L}}_{\tilde{\mathbf{B}}_\mathbf{n}^{(\tilde{\phi})}\cdots\tilde{\mathbf{B}}_\mathbf{k+1}^{(\tilde{\phi})}}\tilde{\mathbf{B}}_\mathbf{k}^{(\tilde{\phi})}\underbrace{\mathbf{U_R D_R T_R}}_{\tilde{\mathbf{B}}_\mathbf{k-1}^{(\tilde{\phi})}\cdots\tilde{\mathbf{B}}_\mathbf{1}^{(\tilde{\phi})}} \rightarrow \underbrace{\mathbf{U_C D_C T_C}}_{\mathbf{U_R D_R T_R U_L D_L T_L}}\tilde{\mathbf{B}}_\mathbf{k}^{(\tilde{\phi})}, \tag{B.3}$$

which preserves the value of the trace because the canonical trace is invariant under cyclic permutations, i.e., $\mathrm{tr}_N[\mathbf{B}_\mathbf{L}^{(\tilde{\phi})}\cdots\mathbf{B}_\mathbf{1}^{(\tilde{\phi})}] = \mathrm{tr}_N[\mathbf{U_C D_C T_C}\tilde{\mathbf{B}}_\mathbf{k}^{(\tilde{\phi})}]$. As we will show in the following, this form reduces the number of QR factorizations needed for each update to two. Since the left factorization $\mathbf{U_L D_L T_L}$ has been precomputed and stored in Eq.(B.2), it can be directly read as $\mathbf{U_L D_L T_L} = \mathbf{U}_\mathbf{k}^{(\tilde{\phi})}\mathbf{D}_\mathbf{k}^{(\tilde{\phi})}\mathbf{T}_\mathbf{k}^{(\tilde{\phi})}$, and only one QR factorization is required to merge two factorizations, $\mathbf{U_C D_C T_C} = \mathbf{U_R D_R T_R U_L D_L T_L}$.

Every time slice in $\tilde{\mathbf{B}}_\mathbf{k}^{(\tilde{\phi})}$ is then updated sequentially according to the Metropolis criterion. That is, we propose a change to the ith time slice $\mathbf{B}_\mathbf{i}^{(\tilde{\phi})}$ in $\tilde{\mathbf{B}}_\mathbf{k}^{(\tilde{\phi})}$ and accept the proposal with probability

$$p_i = \min(1, \frac{Z_N(\{\vec{\phi}\backslash\phi_i\} \cup \phi_i')}{Z_N(\vec{\phi})}), \tag{B.4}$$

where

$$
\begin{aligned}
Z_N(\vec{\phi}) &= \mathrm{tr}_N[\mathbf{U_C D_C T_C} \tilde{\mathbf{B}}_{\mathbf{k}}^{(\tilde{\phi})}] \\
&= \mathrm{tr}_N[\mathbf{U_C D_C} \tilde{\mathbf{T}}], \qquad \text{(B.5)} \\
Z_N(\{\vec{\phi} \backslash \phi_i\} \cup \phi_i')) &= \mathrm{tr}_N[\mathbf{B}_{\mathbf{i+1}}^{(\phi_{\mathbf{i+1}})} \cdots \mathbf{B}_{\mathbf{l+k}}^{(\phi_{\mathbf{l+k}})} \mathbf{U_C D_C T_C} \\
&\quad \cdot \mathbf{B}_{\mathbf{k}}^{(\phi_{\mathbf{k}})} \cdots \mathbf{B}_{\mathbf{i}}^{(\phi_{\mathbf{i}}')}] \\
&= \mathrm{tr}_N[\tilde{\mathbf{U}} \mathbf{D_C} \tilde{\mathbf{T}}]. \qquad \text{(B.6)}
\end{aligned}
$$

Once $\tilde{\mathbf{B}}_{\mathbf{k}}^{(\tilde{\phi})}$ is updated to $\tilde{\mathbf{B}}_{\mathbf{k}}^{(\tilde{\phi}')}$, we update the kth partial factorization of Eq.(B.2) as

$$
\mathbf{U}_{\mathbf{k}}^{(\tilde{\phi})} \mathbf{D}_{\mathbf{k}}^{(\tilde{\phi})} \mathbf{T}_{\mathbf{k}}^{(\tilde{\phi})} \leftarrow \mathbf{U}_{\mathbf{k}}^{(\tilde{\phi}')} \mathbf{D}_{\mathbf{k}}^{(\tilde{\phi}')} \mathbf{T}_{\mathbf{k}}^{(\tilde{\phi}')} = \tilde{\mathbf{B}}_{\mathbf{k}}^{(\tilde{\phi}')} \mathbf{U_R D_R T_R}. \qquad \text{(B.7)}
$$

Hence, one effectively subtracts one group of matrices from the left factorization, updates this group, and then multiplies it into the right factorization. For the kth update, the left factorization can be directly read from the kth element in Eq.(B.2) and the right factorization is computed at the end of the $(k-1)$th update according to Eq.(B.7). Note that at $k = 1$, we have $\mathbf{U_R D_R T_R} = \mathbf{I}$. As a result, a total number of $2n$ QR factorizations are performed during each sweep.

After a full sweep is completed, the partial factorization vector now stores all intermediate right factorizations

$$
[\underbrace{\mathbf{U}_{\mathbf{n-1}}^{(\tilde{\phi}')} \mathbf{D}_{\mathbf{n-1}}^{(\tilde{\phi}')} \mathbf{T}_{\mathbf{n-1}}^{(\tilde{\phi}')}}_{\tilde{\mathbf{B}}_{\mathbf{n-1}}^{(\tilde{\phi}')} \cdots \tilde{\mathbf{B}}_{\mathbf{1}}^{(\tilde{\phi}')}}, \underbrace{\mathbf{U}_{\mathbf{n-2}}^{(\tilde{\phi}')} \mathbf{D}_{\mathbf{n-2}}^{(\tilde{\phi}')} \mathbf{T}_{\mathbf{n-2}}^{(\tilde{\phi}')}}_{\tilde{\mathbf{B}}_{\mathbf{n-2}}^{(\tilde{\phi}')} \cdots \tilde{\mathbf{B}}_{\mathbf{1}}^{(\tilde{\phi}')}}, \ldots, \underbrace{\mathbf{U}_{\mathbf{1}}^{(\tilde{\phi}')} \mathbf{D}_{\mathbf{1}}^{(\tilde{\phi}')} \mathbf{T}_{\mathbf{1}}^{(\tilde{\phi}')}}_{\tilde{\mathbf{B}}_{\mathbf{1}}^{(\tilde{\phi}')}}]. \qquad \text{(B.8)}
$$

In order to reuse the stored factorizations, we need to sweep all of the fields in reverse order in the next run, i.e., we start the sweep from the $k = n$th group of matrices, subtract the kth group from the right factorization for the kth update, whose value can be read from the kth element in Eq.(B.8), update this group, and then multiply it into the left

factorization and store the results to the partial factorization vector as in Eq.(B.7). At the end of the reverse sweep, $\tilde{\mathbf{B}}_{\mathbf{1}}^{(\tilde{\phi}')}$ is updated, and the partial factorization vector is back to the form of Eq.(B.2), which enables a regular sweep to be performed during the next run. Therefore, the fields are swept back and forth, and all partial factorizations not only save computational time but also provide direct access to unequal-time Green's functions or force terms at any imaginary time in Hybrid Monte Carlo algorithms.

For each update, one has to solve the eigenproblem $\mathbf{UDT} = \tilde{\mathbf{U}}\mathbf{D_C}\tilde{\mathbf{T}}$ as given in Eq.(B.6)

$$\mathbf{UDTx} = \lambda\mathbf{x} \tag{B.9}$$

to obtain the spectrum $\{\lambda\}$ that would be used in the canonical partition function calculation. A direct diagonalization of $\mathbf{UDT}$ is not numerically stable and one may permute the factorization as

$$\mathbf{DTUx}' = \lambda\mathbf{x}' \tag{B.10}$$

with $\mathbf{x}' = \mathbf{U^{-1}x}$. The resulting matrices $\mathbf{DTU}$ are row-graded matrices and can be stably diagonalized by matrix balancing [84].

For the observable measurements presented in the main text, we initialize $10 - 60$ independent random walkers. Each walker first sweeps the lattice back and forth $\sim$ 100 times to thermalize and then collects approximately uncorrelated 1000 samples by measuring the observables every ~ 10 sweeps.

Appendix C

Purity and Fidelity of Thermal States

Here, we compare the purity of the thermal state in the canonical and the grand canonical ensembles. To do so, first, we review the relationship between the canonical and the grand canonical thermal states in a system of itinerant particles. If the Hamiltonian $\hat{H}$ governs a system of itinerant particles and also commutes with the system number operator $\hat{N}$, then, we can write

$$e^{-\beta\hat{H}} = \sum_N \hat{\Pi}_N e^{-\beta\hat{H}} \hat{\Pi}_N, \tag{C.1}$$

and thus

$$\mathrm{Tr}\left[e^{-\beta\hat{H}}\right] = \sum_N \mathrm{Tr}_N\left[e^{-\beta\hat{H}}\right], \tag{C.2}$$

where, in general, the canonical trace Tr_N is defined as $\mathrm{Tr}_N[\hat{\rho}] = \mathrm{Tr}\left[\hat{\Pi}_N \hat{\rho} \hat{\Pi}_N\right]$. Accordingly, the canonical thermal state is

$$\hat{\rho}_N(\beta) = \frac{\hat{\Pi}_N e^{-\beta\hat{H}} \hat{\Pi}_N}{Z_N(\beta)}, \tag{C.3}$$

where $Z_N(\beta) = \mathrm{Tr}_N\left[e^{-\beta\hat{H}}\right]$ is the canonical partition function. Next, the thermal state of the system in the grand canonical ensemble is

$$\hat{\rho}_\mu(\beta) = \frac{e^{-\beta\left(\hat{H}-\mu\hat{N}\right)}}{\mathcal{Z}_\mu(\beta)}, \tag{C.4}$$

where, $\mathcal{Z}_\mu(\beta) = \mathrm{Tr}\left[e^{-\beta\left(\hat{H}-\mu\hat{N}\right)}\right]$ is the grand canonical partition function and the constant μ is the chemical potential. As a generalization of Eq. (C.1), we write

$$e^{-\beta\left(\hat{H}-\mu\hat{N}\right)} = \sum_N \hat{\Pi}_N e^{-\beta\hat{H}}\hat{\Pi}_N e^{\beta\mu N}, \tag{C.5}$$

and thus,

$$\hat{\rho}_\mu(\beta) = \sum_N P_\mu(N,\beta)\hat{\rho}_N(\beta), \tag{C.6}$$

where

$$P_\mu(N;\beta) = \frac{e^{\beta\mu N}Z_N(\beta)}{\mathcal{Z}_\mu(\beta)}, \tag{C.7}$$

is the probability that the system is in the N-particle sector for a given μ and β.

C.1 Purity

The purity of a normalized quantum state $\hat{\rho}$ is defined as

$$\mathcal{P} = \mathrm{Tr}\left[\hat{\rho}^2\right]. \tag{C.8}$$

In general, $\mathcal{P}$ is bounded as $1/|\mathcal{H}| \leq \mathcal{P} \leq 1$, where $|\mathcal{H}|$ is the dimension of the corresponding Hilbert space $\mathcal{H}$. The upper bound can be reached, only if $\hat{\rho}$ is pure, in which case it can be expressed as $\hat{\rho} = |\Psi\rangle\langle\Psi|$, where $|\Psi\rangle$ is a normalized state. The lower bound is achieved if $\hat{\rho}$ is proportional to the identity $\hat{I}$, i.e., $\hat{\rho} = \frac{1}{|\mathcal{H}|}\hat{I}$. Consider the thermal

state $\hat{\rho}(\beta) = \frac{e^{-\beta\hat{H}}}{\mathrm{Tr}\left[e^{-\beta\hat{H}}\right]}$ of a system at an inverse temperature β, where $\hat{H}$ is the system Hamiltonian. The purity of such a state is given by

$$\mathcal{P} = \frac{Z(2\beta)}{Z(\beta)^2}, \tag{C.9}$$

where $Z(\beta) = \mathrm{Tr}\left[e^{-\beta\hat{H}}\right]$ is the corresponding partition function.

In the canonical ensemble, we have

$$\mathcal{P}_N = \frac{Z_N(2\beta)}{Z_N(\beta)^2}, \tag{C.10}$$

or equivalently

$$\ln \mathcal{P}_N = 2\beta \left[F_N(\beta) - F_N(2\beta)\right], \tag{C.11}$$

where $F_N(\beta) = -\ln Z_N(\beta)/\beta$ is the free energy. However, the purity of the grand canonical thermal state is

$$\mathcal{P}_\mu = \frac{\mathcal{Z}_\mu(2\beta)}{\mathcal{Z}_\mu(\beta)^2}, \tag{C.12}$$

and similarly

$$\ln \mathcal{P}_\mu = 2\beta \left[\Phi_\mu(\beta) - \Phi_\mu(2\beta)\right], \tag{C.13}$$

where $\Phi_\mu(\beta) = -\ln \mathcal{Z}_\mu(\beta)/\beta$ is the grand free energy.

We can relate the canonical and the grand canonical purity using Eq (C.7), where

$$\mathcal{P}_\mu = \mathcal{P}_N \frac{P_\mu(N;\beta)^2}{P_\mu(N;2\beta)}. \tag{C.14}$$

C.2 Fidelity

Given a quantum state $\hat{\rho}$, we can measure how close it is to a target state $\hat{\rho}_t$ using the mixed-state quantum fidelity $\mathcal{F}(\hat{\rho}, \hat{\rho}_t)$, where $\mathcal{F}$ measures the similarity between the

two quantum states. Yet, in the context of quantum information, different measures of mixed-state fidelity have been proposed [217, 218, 149, 98]. The most familiar definition of the mixed-state fidelity is [217, 218]

$$\tilde{\mathcal{F}}(\hat{\rho}, \hat{\rho}_t) = \mathrm{Tr}\left[\sqrt{\sqrt{\hat{\rho}_t}\hat{\rho}\sqrt{\hat{\rho}_t}}\right], \tag{C.15}$$

which, in general, is difficult to calculate. However a much simpler expression has been proposed [149]

$$\mathcal{F}(\hat{\rho}, \hat{\rho}_t) = \frac{|\mathrm{Tr}\left[\hat{\rho}\hat{\rho}_t\right]|}{\sqrt{\mathrm{Tr}\left[\hat{\rho}^2\right]\mathrm{Tr}\left[\hat{\rho}_t^2\right]}}. \tag{C.16}$$

To test how the grand canonical states approximate the canonical states, we compute

$$\mathcal{F}(\hat{\rho}_\mu, \hat{\rho}_N) = \frac{\mathrm{Tr}\left[\hat{\rho}_\mu\hat{\rho}_N\right]}{\sqrt{\mathrm{Tr}\left[\hat{\rho}_\mu^2\right]\mathrm{Tr}\left[\hat{\rho}_N^2\right]}}, \tag{C.17}$$

which, using $\hat{\rho}_\mu\hat{\rho}_N = P_\mu(N;\beta)\hat{\rho}_N$, gives

$$\mathcal{F}(\hat{\rho}_\mu, \hat{\rho}_N) = P_\mu(N;\beta)\sqrt{\frac{\mathrm{Tr}\left[\hat{\rho}_N^2\right]}{\mathrm{Tr}\left[\hat{\rho}_\mu^2\right]}} = P_\mu(N;\beta)\sqrt{\frac{\mathcal{P}_N}{\mathcal{P}_\mu}}. \tag{C.18}$$

Furthermore, using Eq (C.14), we get

$$\mathcal{F}(\hat{\rho}_\mu, \hat{\rho}_N) = \sqrt{P_\mu(N;2\beta)}. \tag{C.19}$$

Also, employing the fact that $[\hat{\rho}_\mu, \hat{\rho}_N] = 0$, simplifies $\tilde{\mathcal{F}}(\hat{\rho}_\mu, \hat{\rho}_N)$ to

$$\tilde{\mathcal{F}}(\hat{\rho}_\mu, \hat{\rho}_N) = \sqrt{P_\mu(N;\beta)}. \tag{C.20}$$

C.3 Low temperature behavior of the Purity and Fidelity

Let the the spectrum of $\hat{H}$ be $\{E_{N,i}\}$ and the corresponding degeneracies be $\{g_{N,i}\}$, where $\{E_{N,i}\} > \{E_{N,j}\}$ for $i > j$. The canonical partition function $Z_N(\beta)$ for N particles at some inverse temperature β is then

$$Z_N(\beta) = \sum_i g_{N,i} e^{-\beta E_{N,i}}. \tag{C.21}$$

For $\beta\Delta_{N,1} \gg 1$, where $\Delta_{N,i} = E_{N,i} - E_{N,0}$, we have

$$Z_N(\beta) \approx g_{N,0} e^{-\beta E_{N,0}} \left(1 + \frac{g_{N,1}}{g_{N,0}} e^{-\beta\Delta_{N,1}} + \mathcal{O}(e^{-\beta\Delta_{N,2}})\right), \tag{C.22}$$

and thus

$$\begin{aligned} \mathcal{P}_N &= \frac{Z_N(2\beta)}{Z_N(\beta)^2} \\ &\approx \frac{g_{N,0} e^{-2\beta E_{N,0}} \left(1 + \frac{g_{N,1}}{g_{N,0}} e^{-2\beta\Delta_{N,1}} + \mathcal{O}(e^{-2\beta\Delta_{N,2}})\right)}{g_{N,0}^2 e^{-2\beta E_{N,0}} \left(1 + \frac{g_{N,1}}{g_{N,0}} e^{-\beta\Delta_{N,1}} + \mathcal{O}(e^{-\beta\Delta_{N,2}})\right)^2} \\ &\approx \frac{1}{g_{N,0}} \left(1 - \frac{2g_{N,1}}{g_{N,0}} e^{-\beta\Delta_{N,1}} + \mathcal{O}(e^{-\beta\tilde{\Delta}_N})\right), \end{aligned} \tag{C.23}$$

where $\tilde{\Delta} = \min\{\Delta_{N,2}, 2\Delta_{N,1}\}$. For a non-degenerate ground state, $g_{N,0} = 1$, we have

$$\ln(1 - \mathcal{P}_N) \approx -\beta\Delta_{N,1} + \ln 2g_{N,1}. \tag{C.24}$$

For the grand canonical case,

$$\mathcal{Z}_\mu(\beta) = \sum_N e^{\beta\mu N} Z_N(\beta), \tag{C.25}$$

where at sufficiently large β, we have $\mathcal{Z}_\mu(\beta) \approx e^{\beta\mu N}\left(e^{-\mu\beta}Z_{N-1}(\beta) + Z_N(\beta) + e^{\mu\beta}Z_{N+1}(\beta)\right)$ (probability distribution argument) or

$$\mathcal{Z}_\mu(\beta) \approx e^{\beta\mu N} Z_N(\beta)\left(1 + e^{-\mu\beta}\frac{Z_{N-1}(\beta)}{Z_N(\beta)} + e^{\mu\beta}\frac{Z_{N+1}(\beta)}{Z_N(\beta)}\right). \tag{C.26}$$

Also,

$$\begin{aligned}\frac{Z_{N+1}(\beta)}{Z_N(\beta)} &\approx \frac{g_{N+1,0}}{g_{N,0}}e^{-\beta\left(E_{N+1,0}-E_{N,0}\right)}\frac{1+\mathcal{O}(e^{-\beta\Delta_{N+1,1}})}{1+\mathcal{O}(e^{-\beta\Delta_{N,1}})} \\ &\approx \frac{g_{N+1,0}}{g_{N,0}}e^{-\beta\left(E_{N+1,0}-E_{N,0}\right)},\end{aligned} \tag{C.27}$$

and similarly

$$\frac{Z_{N-1}(\beta)}{Z_N(\beta)} \approx \frac{g_{N-1,0}}{g_{N,0}}e^{-\beta\left(E_{N-1,0}-E_{N,0}\right)}. \tag{C.28}$$

Putting everything together, we get

$$\begin{aligned}\mathcal{Z}_\mu(\beta) \approx e^{\beta\mu N} Z_N(\beta)\Bigg[1 &+ \frac{g_{N-1,0}}{g_{N,0}}e^{\beta\left(E_{N,0}-E_{N-1,0}-\mu\right)} \\ &+ \frac{g_{N+1,0}}{g_{N,0}}e^{-\beta\left(E_{N+1,0}-E_{N,0}-\mu\right)}\Bigg].\end{aligned} \tag{C.29}$$

Substituting this into Eq. (C.12) yields

$$\begin{aligned}\mathcal{P}_\mu \approx \mathcal{P}_N[1 &- 2\frac{g_{N-1,0}}{g_{N,0}}e^{\beta\left(E_{N,0}-E_{N-1,0}-\mu\right)} \\ &- 2\frac{g_{N+1,0}}{g_{N,0}}e^{-\beta\left(E_{N+1,0}-E_{N,0}-\mu\right)}].\end{aligned} \tag{C.30}$$

From Eq.(C.29), we can approximate $P_\mu(N;\beta)$ as (assuming that the probability

distribution is sharply peaked at an average of N)

$$\begin{aligned} P_\mu(N;\beta) &= \frac{e^{\beta\mu N} Z_N(\beta)}{\mathcal{Z}_\mu(\beta)} \\ &\approx [1 + \frac{g_{N-1,0}}{g_{N,0}} e^{\beta\left(E_{N,0}-E_{N-1,0}-\mu\right)} \\ &\quad + \frac{g_{N+1,0}}{g_{N,0}} e^{-\beta\left(E_{N+1,0}-E_{N,0}-\mu\right)}]^{-1} \\ &\approx 1 - \frac{g_{N-1,0}}{g_{N,0}} e^{\beta\left(E_{N,0}-E_{N-1,0}-\mu\right)} \\ &\quad - \frac{g_{N+1,0}}{g_{N,0}} e^{-\beta\left(E_{N+1,0}-E_{N,0}-\mu\right)}, \end{aligned} \tag{C.31}$$

and thus

$$\begin{aligned} \mathcal{F}(\hat{\rho}_\mu, \hat{\rho}_N) &= \sqrt{P_\mu(N;2\beta)} \\ &\approx [1 - \frac{g_{N-1,0}}{g_{N,0}} e^{2\beta\left(E_{N,0}-E_{N-1,0}-\mu\right)} \\ &\quad - \frac{g_{N+1,0}}{g_{N,0}} e^{-2\beta\left(E_{N+1,0}-E_{N,0}-\mu\right)}]^{1/2} \\ &\approx 1 - \frac{g_{N-1,0}}{2g_{N,0}} e^{2\beta\left(E_{N,0}-E_{N-1,0}-\mu\right)} \\ &\quad - \frac{g_{N+1,0}}{2g_{N,0}} e^{-2\beta\left(E_{N+1,0}-E_{N,0}-\mu\right)}. \end{aligned} \tag{C.32}$$

Combining the two exponential terms then gives

$$\ln[1 - \mathcal{F}(\hat{\rho}_\mu, \hat{\rho}_N)] \approx -2\beta\Delta\tilde{E} + 2\ln\frac{g}{2}, \tag{C.33}$$

with $\Delta\tilde{E}$ and g represent the effective gap and degeneracy, respectively.

Appendix D

Many-Body Reduced Density Matrix for Free Fermions in the Canonical Ensemble

In this Appendix, we provide details on how to obtain the expression of reduced density matrix and accessible entanglement entropy for free fermions at finite temperature in the canonical ensemble. To prevent ambiguity, we first provide notations for different density matrices:

- ρ: Density matrix of the whole system in the grand canonical ensemble, with the normalization $\mathcal{Z}_\mu$
- ρ_A: Reduced density matrix of the subsystem A in the grand canonical ensemble, with the normalization Z_A
- ρ_{A_n}: n-particle-resolved reduced density matrix of the subsystem A in the grand canonical ensemble with the normalization Z_{A_n}
- $\rho^{(N)}$: Density matrix of the whole system in the N-particle canonical ensemble, with the normalization Z_N

- $\rho_A^{(N)}$: Reduced density matrix of the subsystem A in the N-particle canonical ensemble, with the normalization $Z_{N,A}$
- $\rho_{A_n}^{(N)}$: n-particle-resolved reduced density matrix of the subsystem A in the N-particle canonical ensemble, with the normalization Z_{N,A_n}

Without loss of generality, we assume $\mu = 0$ for all grand canonical ensembles in the following derivations, then for a general non-interacting Hamiltonian

$$\hat{H} = \sum_{i,j} \hat{c}_i^\dagger h_{ij} \hat{c}_j, \tag{D.1}$$

ρ reads

$$\rho = \frac{1}{\mathcal{Z}} e^{-\beta \hat{H}}, \text{ with } \mathcal{Z} = \det\left(\mathbb{I} + e^{-\beta \boldsymbol{H}}\right). \tag{D.2}$$

According to Eq.(7.11) , we have the expression for ρ_A:

$$\rho_A = \det(\mathbb{I} - G_A) \exp\left(\sum_{i,j} \hat{c}_i^\dagger [\ln G_A (\mathbb{I} - G_A)^{-1}]_{ij} \hat{c}_j \right), \tag{D.3}$$

with

$$(G_A)_{ij} = \langle \hat{c}_i^\dagger \hat{c}_j \rangle = [\frac{e^{-\beta \mathbf{H}}}{\mathbb{I} + e^{-\beta \mathbf{H}}}]_{ji}, \forall i, j \in A. \tag{D.4}$$

Though the closed form of $\rho_A^{(N)}$ is difficult to obtain, we show that its matrix elements, $\langle \xi' | \rho_A^{(N)} | \xi \rangle$, are obtainable via extracting the information from its grand canonical counterpart, $\langle \xi' | \rho_A | \xi \rangle$. The extraction is essentially based upon the relation

$$\rho = \sum_{N=0}^{N_s} \frac{Z_N}{\mathcal{Z}} \rho^{(N)}, \tag{D.5}$$

which holds as long as the total particle operator $\hat{N}$ commutes $\hat{H}$. Since this relation is

preserved under any linear operations, a partial trace over the complement of A yields

$$\rho_A = \sum_{N=0}^{N_s} \frac{Z_N}{\mathcal{Z}} \rho_A^{(N)}. \tag{D.6}$$

Hence, we have

$$\langle \xi' | \rho_A | \xi \rangle \mathcal{Z} = \sum_{N=0}^{N_s} \langle \xi' | \rho_A^{(N)} | \xi \rangle Z_N. \tag{D.7}$$

A Fourier transform can then be constructed by defining a sequence of frequencies $\phi_m = 2\pi m/(N_s+1)$:

$$\langle \xi' | e^{i\phi_m \hat{N}} \rho_A | \xi \rangle \tilde{\mathcal{Z}}_m = \sum_{N=0}^{N_s} e^{i\phi_m N} \langle \xi' | \rho_A^{(N)} | \xi \rangle Z_N, \tag{D.8}$$

where $\tilde{\mathcal{Z}}_m$ is the frequency-dependent grand canonical partition function

$$\tilde{\mathcal{Z}}_m = \mathrm{tr}(e^{i\phi_m \hat{N}} e^{-\beta \hat{H}}) = \det\big(\mathbb{I} + e^{i\phi_m} e^{-\beta \mathbf{H}}\big). \tag{D.9}$$

Therefore, performing an inverse Fourier transform gives the projected result

$$\langle \xi' | \rho_A^{(N)} | \xi \rangle Z_N = \frac{1}{N_s+1} \sum_{m=0}^{N_s} e^{-i\phi_m N} \langle \xi' | e^{i\phi_m \hat{N}} \rho_A | \xi \rangle \tilde{\mathcal{Z}}_m. \tag{D.10}$$

Note that the values of $\langle \xi' | e^{i\phi_m \hat{N}} \rho_A | \xi \rangle$ can be computed using the correlation matrix method as is given in Eq.(D.3). For instance, the matrix element corresponding to the empty filling $|\xi'\rangle = |\xi\rangle = |\mathbf{0}\rangle$ may be written as

$$\langle \mathbf{0} | e^{i\phi_m \hat{N}} \rho_A | \mathbf{0} \rangle = \det\Big(\mathbb{I} - \tilde{G}_A^m\Big) = \det\left[\mathbb{I} - \Big(\frac{e^{i\phi_m} e^{-\beta \mathbf{H}}}{\mathbb{I} + e^{i\phi_m} e^{-\beta \mathbf{H}}}\Big)'\right]. \tag{D.11}$$

Hence,

$$\langle \mathbf{0} | \rho_A^{(N)} | \mathbf{0} \rangle = \frac{1}{(N_s+1) Z_N} \sum_{m=0}^{N_s} e^{-i\phi_m N} \det\Big(\mathbb{I} - \tilde{G}_A^m\Big) \tilde{\mathcal{Z}}_m \tag{D.12}$$

Matrix elements of squared density matrices can be computed in a similar manner.

Notice that

$$\langle\xi'|\rho_A^2|\xi\rangle = \sum_{N,N'=0}^{N_s} \frac{Z_N Z_{N'}}{\mathcal{Z}^2}\langle\xi'|\rho_A^{(N)}\rho_A^{(N')}|\xi\rangle, \tag{D.13}$$

a 2D Fourier transform is required to extract information from squared density matrices

$$\begin{aligned}\langle\xi'|e^{i\phi_m\hat{N}}e^{i\phi_n\hat{N}}\rho_A^2|\xi\rangle\tilde{\mathcal{Z}}_m\tilde{\mathcal{Z}}_n &= \sum_{N,N'=0}^{N_s} e^{i\phi_m N}e^{i\phi_m N'} \\ &\times \langle\xi'|\rho_A^{(N)}\rho_A^{(N')}|\xi\rangle Z_N Z_{N'}.\end{aligned} \tag{D.14}$$

An inverse Fourier transform would then yield the projected results. For example, the trace of $(\rho_A^{(N)})^2$ in the N-particle canonical ensemble, which gives access to the Renyi-2 entropy, can be evaluated by first computing

$$\begin{aligned}\gamma_{mn} &:= \mathrm{tr}[e^{i\phi_m\hat{N}}e^{i\phi_n\hat{N}}\rho_A^2] \\ &= \det\Big(\mathbb{I}-\tilde{G}_A^m\Big)\det\Big(\mathbb{I}-\tilde{G}_A^n\Big) \\ &\times \det\Big[\mathbb{I}+\tilde{G}_A^m(\mathbb{I}-\tilde{G}_A^m)^{-1}\cdot\tilde{G}_A^n(\mathbb{I}-\tilde{G}_A^n)^{-1}\Big] \\ &= \det\Big[(\mathbb{I}-\tilde{G}_A^m)(\mathbb{I}-\tilde{G}_A^n)+\tilde{G}_A^m\tilde{G}_A^n\Big],\end{aligned} \tag{D.15}$$

and then doing the inverse Fourier transform

$$\mathrm{tr}[(\rho_A^{(N)})^2] = \frac{1}{(N_s+1)^2 Z_N^2}\sum_{m,n=0}^{N_s} e^{-i\phi_m N}e^{-i\phi_n N}\tilde{\mathcal{Z}}_m\tilde{\mathcal{Z}}_n\gamma_{mn}. \tag{D.16}$$

We may actually trace over a specific k-particle sector of $\rho_A^{(N)}$ and obtain the particle-number-resolved entanglement entropy by following a similar projection scheme, which

again depends on the linearity of Eq.(D.13):

$$\begin{aligned}\mathrm{tr}_{A_k}[\rho_A^2] &:= \sum_{\xi\in A_k}\langle\xi|\rho_A^2|\xi\rangle = P_{k,2}\cdot\mathrm{tr}[(\rho_A^{(N)})^2] \\ &= \sum_{N,N'=0}^{N_s}\frac{Z_N Z_{N'}}{\mathcal{Z}^2}\sum_{\xi\in A_k}\langle\xi|\rho_A^{(N)}\rho_A^{(N')}|\xi\rangle \end{aligned} \tag{D.17}$$

with the definition

$$P_{k,2} := \frac{\mathrm{tr}[\Pi_{A_k}\rho_A^2\Pi_{A_k}]}{\mathrm{tr}[\rho_A^2]}, \tag{D.18}$$

and Π_{A_k} is the k-particle projection operator. $P_{k,2}$ has a Poisson-binomial distribution and can therefore be computed recursively through

$$P_{k,2}(j) = \frac{\nu_{j,2}}{1+\nu_{j,2}}P_{k-1,2}(j-1) + \frac{1}{1+\nu_{j,2}}P_{k,2}(j-1), \tag{D.19}$$

where $\nu_{j,2}$ are eigenvalues of the entanglement Hamiltonian corresponding to ρ_A^2. Then we would compute

$$\tilde{P}_{k,2}^{mn} := \frac{\mathrm{tr}[\Pi_{A_k}e^{i\phi_m\hat{N}}e^{i\phi_n\hat{N}}\rho_A^2\Pi_{A_k}]}{\mathrm{tr}[e^{i\phi_m\hat{N}}e^{i\phi_n\hat{N}}\rho_A^2]} \tag{D.20}$$

recursively, similar to Eq.(7.34):

$$\tilde{P}_{k,2}^{mn}(j) = \frac{\tilde{\nu}_{j,2}^{mn}}{1+\tilde{\nu}_{j,2}^{mn}}\tilde{P}_{k-1,2}^{mn}(j-1) + \frac{1}{1+\tilde{\nu}_{j,2}^{mn}}\tilde{P}_{k,2}^{mn}(j-1), \tag{D.21}$$

while $\tilde{\nu}_{j,2}^{mn}$ are the eigenvalues of the exponentiated entanglement Hamiltonian whose matrix form is

$$e^{-\mathbf{H}_A^{(2)}} = \tilde{G}_A^m(\mathbb{I}-\tilde{G}_A^m)^{-1}\tilde{G}_A^n(\mathbb{I}-\tilde{G}_A^n)^{-1}. \tag{D.22}$$

Performing an inverse Fourier transform based on Eq.(D.17) then yields

$$\mathrm{tr}_{A_k}[(\rho_A^{(N)})^2] = \frac{1}{(N_s+1)^2 Z_N^2}\sum_{m,n=0}^{N_s}e^{-i\phi_m N}e^{-i\phi_n N}\tilde{\mathcal{Z}}_m\tilde{\mathcal{Z}}_n\tilde{P}_{k,2}^{mn}\gamma_{mn}, \tag{D.23}$$

Bibliography

[1] Attila Szabo and Neil S Ostlund. *Modern quantum chemistry: introduction to advanced electronic structure theory*. Courier Corporation, 2012.

[2] I. Shavitt and R.J. Bartlett. *Many-Body Methods in Chemistry and Physics: MBPT and Coupled-Cluster Theory*. Cambridge Molecular Science. Cambridge University Press, 2009. ISBN 9780521818322.

[3] Rodney J. Bartlett and Monika Musiał. Coupled-cluster theory in quantum chemistry. *Rev. Mod. Phys.*, 79:291–352, Feb 2007. doi: 10.1103/RevModPhys.79.291.

[4] Winfried Lorenzen, Andreas Becker, and Ronald Redmer. Progress in warm dense matter and planetary physics. In *Lecture Notes in Computational Science and Engineering*, pages 203–234. Springer International Publishing, 2014.

[5] Jeffrey M. McMahon, Miguel A. Morales, Carlo Pierleoni, and David M. Ceperley. The properties of hydrogen and helium under extreme conditions. *Rev. Mod. Phys.*, Nov 2012.

[6] Shaunak Mukherjee, Florian Libisch, Nicolas Large, Oara Neumann, Lisa V. Brown, Jin Cheng, J. Britt Lassiter, Emily A. Carter, Peter Nordlander, and Naomi J. Halas. Hot electrons do the impossible: Plasmon-induced dissociation of h_2 on au. *Nano Letters*, 13(1):240–247, 2013.

[7] Linan Zhou, Chao Zhang, Michael J. McClain, Alejandro Manjavacas, Caroline M. Krauter, Shu Tian, Felix Berg, Henry O. Everitt, Emily A. Carter, Peter Nordlander,

and Naomi J. Halas. Aluminum nanocrystals as a plasmonic photocatalyst for hydrogen dissociation. *Nano Letters*, 16(2):1478–1484, 2016.

[8] Haiwang Yong, Nikola Zotev, Jennifer M. Ruddock, Brian Stankus, Mats Simmermacher, Andrés Moreno Carrascosa, Wenpeng Du, Nathan Goff, Yu Chang, Darren Bellshaw, Mengning Liang, Sergio Carbajo, Jason E. Koglin, Joseph S. Robinson, Sébastien Boutet, Michael P. Minitti, Adam Kirrander, and Peter M. Weber. Observation of the molecular response to light upon photoexcitation. *Nature Communications*, 11(1), 2020.

[9] Ricardo Ramirez and LM Falicov. Theory of the α- γ phase transition in metallic cerium. *Physical Review B*, 3(8):2425, 1971.

[10] Masatoshi Imada, Atsushi Fujimori, and Yoshinori Tokura. Metal-insulator transitions. *Rev. Mod. Phys.*, 70:1039–1263, 1998.

[11] AI Lichtenstein and MI Katsnelson. Antiferromagnetism and d-wave superconductivity in cuprates: A cluster dynamical mean-field theory. *Physical Review B*, 62 (14):R9283, 2000.

[12] George Christou, Dante Gatteschi, David N Hendrickson, and Roberta Sessoli. Single-molecule magnets. *Mrs Bulletin*, 25(11):66–71, 2000.

[13] J. Orenstein and A. J. Millis. Advances in the physics of high-temperature superconductivity. *Science*, 288(5465):468–474, 2000.

[14] Qimiao Si, Rong Yu, and Elihu Abrahams. High-temperature superconductivity in iron pnictides and chalcogenides. *Nature Reviews Materials*, 1(4), 2016.

[15] T D Ladd, F Jelezko, R Laflamme, Y Nakamura, C Monroe, and J L O'Brien. Quantum computers. *Nature*, 464(7285):45–53, 2010.

[16] Raj Kumar Pathria. *Statistical mechanics*. Elsevier, 2016.

[17] Linda E Reichl. *A modern course in statistical physics*. John Wiley & Sons, 2016.

[18] Takeo Matsubara. A new approach to quantum-statistical mechanics. *Progress of theoretical physics*, 14(4):351–378, 1955.

[19] Richard Phillips Feynman. Space-time approach to non-relativistic quantum mechanics. *Reviews of modern physics*, 20(2):367, 1948.

[20] Piers Coleman. *Introduction to many-body physics*. Cambridge University Press, 2015.

[21] S. A. Jafari. Introduction to Hubbard Model and Exact Diagonalization. *arXiv e-prints*, art. arXiv:0807.4878, July 2008.

[22] N.David Mermin. Stability of the thermal hartree-fock approximation. *Annals of Physics*, 21(1):99 – 121, 1963.

[23] G Sanyal, Sk. H Mandal, and D Mukherjee. On optimal mean-field descriptions in finite-temperature many-body theories: Use of thermal Brillouin and Bruckner conditions. *Proceedings of the Indian Academy of Sciences - Chemical Sciences*, 106 (2):407, 1994. ISSN 0973-7103.

[24] Valentin V. Karasiev, Travis Sjostrom, James Dufty, and S. B. Trickey. Accurate homogeneous electron gas exchange-correlation free energy for local spin-density calculations. *Phys. Rev. Lett.*, 112:076403, Feb 2014.

[25] Aurora Pribram-Jones, Stefano Pittalis, EKU Gross, and Kieron Burke. Thermal density functional theory in context. In *Frontiers and Challenges in Warm Dense Matter*, pages 25–60. Springer, 2014.

[26] Gaurav Harsha, Thomas M. Henderson, and Gustavo E. Scuseria. Thermofield theory for finite-temperature quantum chemistry. *J. Chem. Phys.*, 150(15):154109, 2019.

[27] Gaurav Harsha, Thomas M. Henderson, and Gustavo E. Scuseria. Thermofield theory for finite-temperature coupled cluster. *Journal of Chemical Theory and Computation*, 15(11):6127–6136, 2019.

[28] Alec F. White and Garnet Kin-Lic Chan. A time-dependent formulation of coupled-cluster theory for many-fermion systems at finite temperature. *J. Chem. Theory Comput.*, 14(11):5690–5700, September 2018.

[29] Alec F. White and Garnet Kin-Lic Chan. Finite-temperature coupled cluster: Efficient implementation and application to prototypical systems. *J. Chem. Phys.*, 152(22):224104, 2020.

[30] Philip Shushkov and Thomas F. Miller. Real-time density-matrix coupled-cluster approach for closed and open systems at finite temperature. *J. Chem. Phys.*, 151 (13):134107, 2019.

[31] Punit K Jha and So Hirata. Numerical evidence invalidating finite-temperature many-body perturbation theory. In *Annual Reports in Computational Chemistry*, volume 15, pages 3–15. Elsevier, 2019.

[32] Punit K. Jha and So Hirata. Finite-temperature many-body perturbation theory in the canonical ensemble. *Phys. Rev. E*, 101:022106, 2020.

[33] Alec F. White and Garnet Kin-Lic Chan. Comment on "Numerical Evidence Falsifying Finite-Temperature Many-Body Perturbation Theory". *arXiv e-prints*, art. arXiv:1810.03653, October 2018.

[34] So Hirata and Punit K Jha. Converging finite-temperature many-body perturbation theory in the grand canonical ensemble that conserves the average number of electrons. In *Annual Reports in Computational Chemistry*, volume 15, pages 17–37. Elsevier, 2019.

[35] So Hirata and Punit K. Jha. Finite-temperature many-body perturbation theory in the grand canonical ensemble. *J. Chem. Phys.*, 153(1):014103, 2020.

[36] R. Santra and J. Schirmer. Finite-temperature second-order many-body perturbation theory revisited. *Chemical Physics*, 482:355 – 361, 2017. Electrons and nuclei in motion - correlation and dynamics in molecules (on the occasion of the 70th birthday of Lorenz S. Cederbaum).

[37] Dominika Zgid and Emanuel Gull. Finite temperature quantum embedding theories for correlated systems. *New J. Phys.*, 19(2):023047, 2017.

[38] Antoine Georges, Gabriel Kotliar, Werner Krauth, and Marcelo J. Rozenberg. Dynamical mean-field theory of strongly correlated fermion systems and the limit of infinite dimensions. *Rev. Mod. Phys.*, 68:13–125, 1996.

[39] G. Kotliar, S. Y. Savrasov, K. Haule, V. S. Oudovenko, O. Parcollet, and C. A. Marianetti. Electronic structure calculations with dynamical mean-field theory. *Rev. Mod. Phys.*, 78:865–951, 2006.

[40] Alicia Rae Welden, Alexander A. Rusakov, and Dominika Zgid. Exploring connections between statistical mechanics and green's functions for realistic systems: Temperature dependent electronic entropy and internal energy from a self-consistent second-order green's function. *J. Chem. Phys.*, 145(20):204106, 2016.

[41] Alexei A. Kananenka, Alicia Rae Welden, Tran Nguyen Lan, Emanuel Gull, and Dominika Zgid. Efficient temperature-dependent green's function methods for realistic systems: Using cubic spline interpolation to approximate matsubara green's functions. *J. Chem. Theory Comput.*, 12(5):2250–2259, 2016.

[42] Alexei A. Kananenka, Jordan J. Phillips, and Dominika Zgid. Efficient temperature-dependent green's functions methods for realistic systems: Compact grids for orthogonal polynomial transforms. *J. Chem. Theory Comput.*, 12(2):564–571, 2016.

[43] W. M. C. Foulkes, L. Mitas, R. J. Needs, and G. Rajagopal. Quantum monte carlo simulations of solids. *Rev. Mod. Phys.*, 73:33–83, 2001.

[44] Julien Toulouse, Roland Assaraf, and Cyrus J. Umrigar. Chapter fifteen - introduction to the variational and diffusion monte carlo methods. In Philip E. Hoggan and Telhat Ozdogan, editors, *Electron Correlation in Molecules, ab initio Beyond Gaussian Quantum Chemistry*, volume 73 of *Advances in Quantum Chemistry*, pages 285 – 314. Academic Press, 2016.

[45] J. Gubernatis, N. Kawashima, and P. Werner. *Quantum Monte Carlo Methods: Algorithms for Lattice Models*. Cambridge University Press, 2016.

[46] Mario Motta and Shiwei Zhang. Ab initio computations of molecular systems by the auxiliary-field quantum monte carlo method. *Wiley Interdisciplinary Reviews: Computational Molecular Science*, 8(5):e1364, 2018.

[47] S. R. White, D. J. Scalapino, R. L. Sugar, E. Y. Loh, J. E. Gubernatis, and R. T. Scalettar. Numerical study of the two-dimensional hubbard model. *Phys. Rev. B*, 40(1):506–516, July 1989.

[48] J. E. Hirsch. Two-dimensional hubbard model: Numerical simulation study. *Phys. Rev. B*, 31:4403–4419, 1985.

[49] Zhaojun Bai, Wenbin Chen, Richard Scalettar, and Ichitaro Yamazaki. Numerical methods for quantum monte carlo simulations of the hubbard model. In *Multi-Scale Phenomena in Complex Fluids*, pages 1–110. World Scientific, 2009.

[50] Shiwei Zhang. Finite-temperature monte carlo calculations for systems with fermions. *Phys. Rev. Lett.*, 83:2777–2780, 1999.

[51] Yuan-Yao He, Hao Shi, and Shiwei Zhang. Reaching the continuum limit in finite-temperature ab initio field-theory computations in many-fermion systems. *Phys. Rev. Lett.*, 123:136402, 2019.

[52] Yuan Liu, Minsik Cho, and Brenda Rubenstein. Ab initio finite temperature auxiliary field quantum monte carlo. *Journal of Chemical Theory and Computation*, 14(9): 4722–4732, 2018.

[53] Zi-Xiang Li and Hong Yao. Sign-problem-free fermionic quantum monte carlo: Developments and applications. *Annual Review of Condensed Matter Physics*, 10 (1):337–356, 2019.

[54] E. Y. Loh, J. E. Gubernatis, R. T. Scalettar, S. R. White, D. J. Scalapino, and R. L. Sugar. Sign problem in the numerical simulation of many-electron systems. *Phys. Rev. B*, 41:9301–9307, 1990.

[55] Shiwei Zhang, J. Carlson, and J. E. Gubernatis. Constrained path monte carlo method for fermion ground states. *Phys. Rev. B*, 55:7464–7477, 1997.

[56] Shiwei Zhang and Henry Krakauer. Quantum monte carlo method using phase-free random walks with slater determinants. *Physical review letters*, 90(13):136401, 2003.

[57] Shiwei Zhang, J. Carlson, and J. E. Gubernatis. Constrained path quantum monte carlo method for fermion ground states. *Phys. Rev. Lett.*, 74:3652–3655, 1995.

[58] Bo-Xiao Zheng, Chia-Min Chung, Philippe Corboz, Georg Ehlers, Ming-Pu Qin, Reinhard M. Noack, Hao Shi, Steven R. White, Shiwei Zhang, and Garnet Kin-Lic Chan. Stripe order in the underdoped region of the two-dimensional hubbard model. *Science*, 358(6367):1155–1160, 2017.

[59] J. P. F. LeBlanc, Andrey E. Antipov, Federico Becca, Ireneusz W. Bulik, Garnet Kin-Lic Chan, Chia-Min Chung, Youjin Deng, Michel Ferrero, Thomas M. Henderson, Carlos A. Jiménez-Hoyos, E. Kozik, Xuan-Wen Liu, Andrew J. Millis, N. V. Prokof'ev, Mingpu Qin, Gustavo E. Scuseria, Hao Shi, B. V. Svistunov, Luca F. Tocchio, I. S. Tupitsyn, Steven R. White, Shiwei Zhang, Bo-Xiao Zheng, Zhenyue Zhu, and

Emanuel Gull and. Solutions of the two-dimensional hubbard model: Benchmarks and results from a wide range of numerical algorithms. *Phys. Rev. X*, 5(4), 2015.

[60] Wirawan Purwanto, Shiwei Zhang, and Henry Krakauer. An auxiliary-field quantum monte carlo study of the chromium dimer. *J. Chem. Phys.*, 142(6):064302, 2015.

[61] Malliga Suewattana, Wirawan Purwanto, Shiwei Zhang, Henry Krakauer, and Eric J. Walter. Phaseless auxiliary-field quantum monte carlo calculations with plane waves and pseudopotentials: Applications to atoms and molecules. *Phys. Rev. B*, 75: 245123, 2007.

[62] James Shee, Shiwei Zhang, David R. Reichman, and Richard A. Friesner. Chemical transformations approaching chemical accuracy via correlated sampling in auxiliary-field quantum monte carlo. *J. Chem. Theory Comput.*, 13(6):2667–2680, 2017.

[63] Yuan Liu, Tong Shen, Hang Zhang, and Brenda Rubenstein. Unveiling the finite temperature physics of hydrogen chains via auxiliary field quantum monte carlo. *Journal of Chemical Theory and Computation*, 16(7):4298–4314, 2020.

[64] Fengjie Ma, Wirawan Purwanto, Shiwei Zhang, and Henry Krakauer. Quantum monte carlo calculations in solids with downfolded hamiltonians. *Phys. Rev. Lett.*, 114:226401, 2015.

[65] Wirawan Purwanto, Shiwei Zhang, and Henry Krakauer. Frozen-orbital and down-folding calculations with auxiliary-field quantum monte carlo. *J. Chem. Theory Comput.*, 9(11):4825–4833, 2013.

[66] Shuai Zhang, Fionn D. Malone, and Miguel A. Morales. Auxiliary-field quantum monte carlo calculations of the structural properties of nickel oxide. *J. Chem. Phys.*, 149(16):164102, 2018.

[67] D.A. McQuarrie. *Statistical Mechanics*. University Science Books, 2000. ISBN 9781891389153.

[68] Biswaroop Mukherjee, Zhenjie Yan, Parth B Patel, Zoran Hadzibabic, Tarik Yefsah, Julian Struck, and Martin W Zwierlein. Homogeneous atomic fermi gases. *Physical review letters*, 118(12):123401, 2017.

[69] Klaus Hueck, Niclas Luick, Lennart Sobirey, Jonas Siegl, Thomas Lompe, and Henning Moritz. Two-dimensional homogeneous fermi gases. *Physical Review Letters*, 120(6):060402, 2018.

[70] Nir Navon, Robert P Smith, and Zoran Hadzibabic. Quantum gases in optical boxes. *Nature Physics*, 17(12):1334–1341, 2021.

[71] Yoram Alhassid. Auxiliary-field quantum monte carlo methods in nuclei. In *Emergent Phenomena in Atomic Nuclei from Large-Scale Modeling: a Symmetry-Guided Perspective*, pages 267–298. World Scientific, 2017.

[72] Hayley R Petras, Sai Kumar Ramadugu, Fionn D Malone, and James J Shepherd. Using density matrix quantum monte carlo for calculating exact-on-average energies for ab initio hamiltonians in a finite basis set. *Journal of chemical theory and computation*, 16(2):1029–1038, 2020.

[73] Fionn D Malone, NS Blunt, James J Shepherd, DKK Lee, JS Spencer, and WMC Foulkes. Interaction picture density matrix quantum monte carlo. *The Journal of chemical physics*, 143(4), 2015.

[74] Fionn D Malone, NS Blunt, Ethan W Brown, DKK Lee, JS Spencer, WMC Foulkes, and James J Shepherd. Accurate exchange-correlation energies for the warm dense electron gas. *Physical review letters*, 117(11):115701, 2016.

[75] Ethan W Brown, Bryan K Clark, Jonathan L DuBois, and David M Ceperley. Path-integral monte carlo simulation of the warm dense homogeneous electron gas. *Physical review letters*, 110(14):146405, 2013.

[76] H. M. Wiseman and John A. Vaccaro. Entanglement of indistinguishable particles shared between two parties. *Phys. Rev. Lett.*, 91:097902, 2003.

[77] Stephen D. Bartlett and H. M. Wiseman. Entanglement constrained by superselection rules. *Phys. Rev. Lett.*, 91:097903, 2003.

[78] Hatem Barghathi, C. M. Herdman, and Adrian Del Maestro. Rényi generalization of the accessible entanglement entropy. *Phys. Rev. Lett.*, 121:150501, 2018.

[79] Thomas Rauscher, Friedrich-Karl Thielemann, and Karl-Ludwig Kratz. Nuclear level density and the determination of thermonuclear rates for astrophysics. *Phys. Rev. C*, 56:1613–1625, 1997.

[80] Joonho Lee, Miguel A Morales, and Fionn D Malone. A phaseless auxiliary-field quantum monte carlo perspective on the uniform electron gas at finite temperatures: Issues, observations, and benchmark study. *The Journal of Chemical Physics*, 154 (6), 2021.

[81] Hatem Barghathi, Jiangyong Yu, and Adrian Del Maestro. Theory of noninteracting fermions and bosons in the canonical ensemble. *Physical Review Research*, 2(4): 043206, 2020.

[82] Peter Borrmann and Gert Franke. Recursion formulas for quantum statistical partition functions. *The Journal of chemical physics*, 98(3):2484, 1993.

[83] W. E. Ormand, D. J. Dean, C. W. Johnson, G. H. Lang, and S. E. Koonin. Demonstration of the auxiliary-field monte carlo approach for sd-shell nuclei. *Phys. Rev. C*, 49:1422–1427, 1994.

[84] CN Gilbreth and Y Alhassid. Stabilizing canonical-ensemble calculations in the auxiliary-field monte carlo method. *Computer Physics Communications*, 188:1–6, 2015.

[85] Cole Miles, Benjamin Cohen-Stead, Owen Bradley, Steven Johnston, Richard Scalettar, and Kipton Barros. Dynamical tuning of the chemical potential to achieve a target particle number in grand canonical Monte Carlo simulations. *Phys. Rev. E*, 105(4):045311, 2022.

[86] G. H. Lang, C. W. Johnson, S. E. Koonin, and W. E. Ormand. Monte carlo evaluation of path integrals for the nuclear shell model. *Phys. Rev. C*, 48:1518–1545, 1993.

[87] C. N. Gilbreth and Y. Alhassid. Pair condensation in a finite trapped fermi gas. *Phys. Rev. A*, 88:063643, 2013.

[88] S. Jensen, C. N. Gilbreth, and Y. Alhassid. Pairing correlations across the superfluid phase transition in the unitary fermi gas. *Phys. Rev. Lett.*, 124:090604, 2020.

[89] C. M. Herdman, A. Rommal, and A. Del Maestro. Quantum monte carlo measurement of the chemical potential of ^{4}He. *Phys. Rev. B*, 89:224502, 2014.

[90] Zhenjiu Wang, Fakher F. Assaad, and Francesco Parisen Toldin. Finite-size effects in canonical and grand-canonical quantum monte carlo simulations for fermions. *Phys. Rev. E*, 96:042131, 2017.

[91] R. D. Sedgewick, D. J. Scalapino, R. L. Sugar, and L. Capriotti. Canonical and grand canonical ensemble expectation values from quantum monte carlo simulations. *Phys. Rev. B*, 68:045120, 2003.

[92] J. E. Hirsch. Discrete hubbard-stratonovich transformation for fermion lattice models. *Phys. Rev. B*, 28(7):4059–4061, 1983.

[93] RL Stratonovich. On a method of calculating quantum distribution functions. In *Soviet Physics Doklady*, volume 2, page 416, 1957.

[94] J. Hubbard. Calculation of partition functions. *Phys. Rev. Lett.*, 3:77–78, 1959.

[95] Mario Motta and Shiwei Zhang. Ab initio computations of molecular systems by the auxiliary-field quantum Monte Carlo method. *WIREs Comp. Mol. Sci.*, 8(5): 1364, 2018.

[96] Tong Shen, Yuan Liu, Yang Yu, and Brenda M. Rubenstein. Finite temperature auxiliary field quantum monte carlo in the canonical ensemble. *J. Chem. Phys.*, 153 (20):204108, 2020.

[97] Lars Bonnes, Hannes Pichler, and Andreas M. Läuchli. Entropy perspective on the thermal crossover in a fermionic hubbard chain. *Phys. Rev. B*, 88:155103, 2013.

[98] Gilles Parez. Symmetry-resolved rényi fidelities and quantum phase transitions. *Phys. Rev. B*, 106:235101, 2022.

[99] Jonathan Goodman and Jonathan Weare. Ensemble samplers with affine invariance. *Communications in applied mathematics and computational science*, 5(1):65–80, 2010.

[100] Wirawan Purwanto, Henry Krakauer, Yudistira Virgus, and Shiwei Zhang. Assessing weak hydrogen binding on ca+ centers: An accurate many-body study with large basis sets. *The Journal of chemical physics*, 135(16), 2011.

[101] Thomas Barthel and Yikang Zhang. Optimized lie–trotter–suzuki decompositions for two and three non-commuting terms. *Annals of Physics*, 418:168165, 2020.

[102] Zi-Xiang Li and Hong Yao. Sign-problem-free fermionic quantum monte carlo: Developments and applications. *Annual Review of Condensed Matter Physics*, 10: 337–356, 2019.

[103] MA Martin-Delgado, Marco Roncaglia, and G Sierra. Stripe ansätze from exactly solved models. *Physical Review B*, 64(7):075117, 2001.

[104] Frank Verstraete, Michael M Wolf, David Perez-Garcia, and J Ignacio Cirac. Criticality, the area law, and the computational power of projected entangled pair states. *Physical review letters*, 96(22):220601, 2006.

[105] Seth Lloyd. Universal quantum simulators. *Science*, 273(5278):1073–1078, 1996.

[106] Ben P Lanyon, Cornelius Hempel, Daniel Nigg, Markus Müller, Rene Gerritsma, F Zähringer, Philipp Schindler, Julio T Barreiro, Markus Rambach, Gerhard Kirchmair, et al. Universal digital quantum simulation with trapped ions. *Science*, 334 (6052):57–61, 2011.

[107] DR Hamann and SB Fahy. Energy measurement in auxiliary-field many-electron calculations. *Physical Review B*, 41(16):11352, 1990.

[108] Brenda M Rubenstein, Shiwei Zhang, and David R Reichman. Finite-temperature auxiliary-field quantum monte carlo technique for bose-fermi mixtures. *Physical Review A*, 86(5):053606, 2012.

[109] Tong Shen, Yuan Liu, Yang Yu, and Brenda M Rubenstein. Finite temperature auxiliary field quantum monte carlo in the canonical ensemble. *The Journal of Chemical Physics*, 153(20), 2020.

[110] GM Buendia. Comparative study of the discrete and the continuous hubbard-stratonovich transformation for a one-dimensional spinless fermion model. *Physical Review B*, 33(5):3519, 1986.

[111] Jorge E Hirsch. Discrete hubbard-stratonovich transformation for fermion lattice models. *Physical Review B*, 28(7):4059, 1983.

[112] Jorge E Hirsch. Two-dimensional hubbard model: Numerical simulation study. *Physical Review B*, 31(7):4403, 1985.

[113] Peter Broecker and Simon Trebst. Numerical stabilization of entanglement computation in auxiliary-field quantum monte carlo simulations of interacting many-fermion systems. *Physical Review E*, 94(6):063306, 2016.

[114] Fakher Assaad, Martin Bercx, Florian Goth, Anika Götz, Johannes Hofmann, Emilie Huffman, Zihong Liu, Francesco Parisen Toldin, Jefferson Portela, and Jonas Schwab. The alf (algorithms for lattice fermions) project release 2.0. documentation for the auxiliary-field quantum monte carlo code. *SciPost Physics Codebases*, page 001, 2022.

[115] Martin Bercx, Florian Goth, Johannes Stephan Hofmann, and Fakher Assaad. The alf (algorithms for lattice fermions) project release 1.0. documentation for the auxiliary field quantum monte carlo code. *SciPost Physics*, 3(2):013, 2017.

[116] Stefan Rombouts, Kristiaan Heyde, and Natalie Jachowicz. A discrete hubbard-stratonovich decomposition for general, fermionic two-body interactions. *Physics Letters A*, 242(4-5):271–276, 1998.

[117] Fakher F Assaad, Masatoshi Imada, and Douglas J Scalapino. Charge and spin structures of a d x 2- y 2 superconductor in the proximity of an antiferromagnetic mott insulator. *Physical Review B*, 56(23):15001, 1997.

[118] Zhou-Quan Wan, Shi-Xin Zhang, and Hong Yao. Mitigating sign problem by automatic differentiation. *arXiv preprint arXiv:2010.01141*, 2020.

[119] Richard Blankenbecler, DJ Scalapino, and RL Sugar. Monte carlo calculations of coupled boson-fermion systems. i. *Physical Review D*, 24(8):2278, 1981.

[120] Steven R White, Douglas J Scalapino, Robert L Sugar, EY Loh, James E Gubernatis, and Richard T Scalettar. Numerical study of the two-dimensional hubbard model. *Physical Review B*, 40(1):506, 1989.

[121] EY Loh Jr, JE Gubernatis, RT Scalettar, SR White, DJ Scalapino, and RL Sugar. Sign problem in the numerical simulation of many-electron systems. *Physical Review B*, 41(13):9301, 1990.

[122] Matthias Troyer and Uwe-Jens Wiese. Computational complexity and fundamental limitations to fermionic quantum monte carlo simulations. *Physical review letters*, 94(17):170201, 2005.

[123] Congjun Wu and Shou-Cheng Zhang. Sufficient condition for absence of the sign problem in the fermionic quantum monte carlo algorithm. *Physical Review B*, 71 (15):155115, 2005.

[124] Shiwei Zhang, Joseph Carlson, and James E Gubernatis. Constrained path monte carlo method for fermion ground states. *Physical Review B*, 55(12):7464, 1997.

[125] Shiwei Zhang. Finite-temperature monte carlo calculations for systems with fermions. *Physical review letters*, 83(14):2777, 1999.

[126] Mingpu Qin, Hao Shi, and Shiwei Zhang. Coupling quantum monte carlo and independent-particle calculations: Self-consistent constraint for the sign problem based on the density or the density matrix. *Physical Review B*, 94(23):235119, 2016.

[127] Mohammad-Sadegh Vaezi, Amir-Reza Negari, Amin Moharramipour, and Abolhassan Vaezi. Amelioration for the sign problem: An adiabatic quantum monte carlo algorithm. *Physical Review Letters*, 127(21):217003, 2021.

[128] Zi-Xiang Li, Yi-Fan Jiang, and Hong Yao. Solving the fermion sign problem in quantum monte carlo simulations by majorana representation. *Physical Review B*, 91(24):241117, 2015.

[129] Ryan Levy and Bryan K Clark. Mitigating the sign problem through basis rotations. *Physical review letters*, 126(21):216401, 2021.

[130] Maksim Ulybyshev, Christopher Winterowd, and Savvas Zafeiropoulos. Lefschetz thimbles decomposition for the hubbard model on the hexagonal lattice. *Physical Review D*, 101(1):014508, 2020.

[131] Peter Borrmann, Jens Harting, Oliver Mülken, and Eberhard R Hilf. Calculation of thermodynamic properties of finite bose-einstein systems. *Physical Review A*, 60(2): 1519, 1999.

[132] Siegfried Grossmann and Martin Holthaus. Fluctuations of the particle number in a trapped bose-einstein condensate. *Physical review letters*, 79(19):3557, 1997.

[133] Peter Borrmann, Oliver Mülken, and Jens Harting. Classification of phase transitions in small systems. *Physical Review Letters*, 84(16):3511, 2000.

[134] K Schönhammer. Thermodynamics and occupation numbers of a fermi gas in the canonical ensemble. *American Journal of Physics*, 68(11):1032–1037, 2000.

[135] K Schönhammer. Deviations from wick's theorem in the canonical ensemble. *Physical Review A*, 96(1):012102, 2017.

[136] Wim Magnus and Fons Brosens. Occupation numbers in a quantum canonical ensemble: A projection operator approach. *Physica A: Statistical Mechanics and its Applications*, 518:253–264, 2019.

[137] Aurélien Grabsch, Satya Majumdar, Grégory Schehr, and Christophe Texier. Fluctuations of observables for free fermions in a harmonic trap at finite temperature. *SciPost Physics*, 4(3):014, 2018.

[138] Yili Hong. On computing the distribution function for the poisson binomial distribution. *Computational Statistics & Data Analysis*, 59:41–51, 2013.

[139] A.L. Fetter and J.D. Walecka. *Quantum Theory of Many-Particle Systems*. Dover Books on Physics. Dover Publications, 2012.

[140] Helmut Schmidt. A simple derivation of distribution functions for bose and fermi statistics. *Am. J. Phys.*, 57(12):1150–1151, 1989.

[141] Tong Shen, Hatem Barghathi, Jiangyong Yu, Adrian Del Maestro, and Brenda M Rubenstein. Stable recursive auxiliary field quantum monte carlo algorithm in the canonical ensemble: Applications to thermometry and the hubbard model. *Physical Review E*, 107(5):055302, 2023.

[142] Olivier Giraud, Aurélien Grabsch, and Christophe Texier. Correlations of occupation numbers in the canonical ensemble and application to a bose-einstein condensate in a one-dimensional harmonic trap. *Physical Review A*, 97(5):053615, 2018.

[143] Gian-Carlo Wick. The evaluation of the collision matrix. *Physical review*, 80(2):268, 1950.

[144] C.N. Gilbreth, S. Jensen, and Y. Alhassid. Reducing the complexity of finite-temperature auxiliary-field quantum monte carlo. *Computer Physics Communications*, 264:107952, 2021.

[145] Pasquale Calabrese and John Cardy. Entanglement entropy and quantum field theory. *J. Stat. Mech.: Theor. Exp.*, 2004(06):06002, 2004.

[146] A. J. Daley, H. Pichler, J. Schachenmayer, and P. Zoller. Measuring entanglement growth in quench dynamics of bosons in an optical lattice. *Phys. Rev. Lett.*, 109: 020505, 2012.

[147] Peter Broecker and Simon Trebst. Rényi entropies of interacting fermions from determinantal quantum monte carlo simulations. *Journal of Statistical Mechanics: Theory and Experiment*, 2014(8):P08015, 2014.

[148] Fakher F Assaad. Stable quantum monte carlo simulations for entanglement spectra of interacting fermions. *Phys. Rev. B*, 91(12):125146, 2015.

[149] Xiaoguang Wang, Chang-Shui Yu, and X.X. Yi. An alternative quantum fidelity for mixed states of qudits. *Phys. Lett. A*, 373(1):58–60, 2008.

[150] Roberto Onofrio. Physics of our days: Cooling and thermometry of atomic fermi gases. *Physics-Uspekhi*, 59(11):1129, 2016.

[151] Ehud Altman, Eugene Demler, and Mikhail D. Lukin. Probing many-body states of ultracold atoms via noise correlations. *Phys. Rev. A*, 70(1):013603, 2004.

[152] E. D. Kuhnle, H. Hu, X.-J. Liu, P. Dyke, M. Mark, P. D. Drummond, P. Hannaford, and C. J. Vale. Universal Behavior of Pair Correlations in a Strongly Interacting Fermi Gas. *Phys. Rev. Lett.*, 105(7):070402, 2010.

[153] M. Boll, T. A. Hilker, G. Salomon, A. Omran, J. Nespolo, L. Pollet, I. Bloch, and C. Gross. Spin-and density-resolved microscopy of antiferromagnetic correlations in Fermi-Hubbard chains. *Science*, 353(6305):1257, 2016.

[154] T. L. Yang, P. Grišins, Y.T. Chang, Z.H. Zhao, C.Y. Shih, T. Giamarchi, and R.G. Hulet. Measurement of the Dynamical Structure Factor of a 1D interacting Fermi Gas. *Phys. Rev. Lett.*, 121(10):103001, 2018.

[155] Marc Andrew Valdez, Daniel Jaschke, David L Vargas, and Lincoln D Carr. Quantifying complexity in quantum phase transitions via mutual information complex networks. *Physical review letters*, 119(22):225301, 2017.

[156] C Walsh, P Sémon, D Poulin, G Sordi, and A-MS Tremblay. Local entanglement entropy and mutual information across the mott transition in the two-dimensional hubbard model. *Physical Review Letters*, 122(6):067203, 2019.

[157] Karyn Le Hur. Entanglement entropy, decoherence, and quantum phase transitions of a dissipative two-level system. *Annals of Physics*, 323(9):2208–2240, 2008.

[158] Elena Canovi, Elisa Ercolessi, Piero Naldesi, Luca Taddia, and Davide Vodola. Dynamics of entanglement entropy and entanglement spectrum crossing a quantum phase transition. *Physical Review B*, 89(10):104303, 2014.

[159] Katharina Boguslawski and Paweł Tecmer. Orbital entanglement in quantum chemistry. *International Journal of Quantum Chemistry*, 115(19):1289–1295, 2015.

[160] Felix Plasser. Entanglement entropy of electronic excitations. *The Journal of Chemical Physics*, 144(19), 2016.

[161] Lei Wang, Ye-Hua Liu, Jakub Imriška, Ping Nang Ma, and Matthias Troyer. Fidelity susceptibility made simple: A unified quantum monte carlo approach. *Physical Review X*, 5(3):031007, 2015.

[162] Shi-Jian Gu, Ho-Man Kwok, Wen-Qiang Ning, Hai-Qing Lin, et al. Fidelity susceptibility, scaling, and universality in quantum critical phenomena. *Physical Review B*, 77(24):245109, 2008.

[163] Katharina Boguslawski, Pawel Tecmer, Ors Legeza, and Markus Reiher. Entanglement measures for single-and multireference correlation effects. *The journal of physical chemistry letters*, 3(21):3129–3135, 2012.

[164] Katharina Boguslawski, Pawel Tecmer, Gergely Barcza, Ors Legeza, and Markus Reiher. Orbital entanglement in bond-formation processes. *Journal of Chemical Theory and Computation*, 9(7):2959–2973, 2013.

[165] Christopher J Stein and Markus Reiher. Automated selection of active orbital spaces. *Journal of chemical theory and computation*, 12(4):1760–1771, 2016.

[166] Alexei Kitaev and John Preskill. Topological entanglement entropy. *Physical review letters*, 96(11):110404, 2006.

[167] Michael Levin and Xiao-Gang Wen. Detecting topological order in a ground state wave function. *Physical review letters*, 96(11):110405, 2006.

[168] Hong-Chen Jiang, Zhenghan Wang, and Leon Balents. Identifying topological order by entanglement entropy. *Nature Physics*, 8(12):902–905, 2012.

[169] Guifré Vidal and Reinhard F Werner. Computable measure of entanglement. *Physical Review A*, 65(3):032314, 2002.

[170] Pasquale Calabrese and John Cardy. Entanglement entropy and quantum field theory. *Journal of statistical mechanics: theory and experiment*, 2004(06):P06002, 2004.

[171] Jens Eisert, Marcus Cramer, and Martin B Plenio. Colloquium: Area laws for the entanglement entropy. *Reviews of modern physics*, 82(1):277, 2010.

[172] Ryszard Horodecki, Paweł Horodecki, Michał Horodecki, and Karol Horodecki. Quantum entanglement. *Reviews of modern physics*, 81(2):865, 2009.

[173] Tatsuma Nishioka. Entanglement entropy: holography and renormalization group. *Reviews of Modern Physics*, 90(3):035007, 2018.

[174] Michael A Nielsen and Isaac L Chuang. Quantum computation and quantum information. *Phys. Today*, 54(2):60, 2001.

[175] CF Roos, GPT Lancaster, M Riebe, H Häffner, W Hänsel, S Gulde, C Becher, J Eschner, F Schmidt-Kaler, and R Blatt. Bell states of atoms with ultralong lifetimes and their tomographic state analysis. *Physical review letters*, 92(22):220402, 2004.

[176] Hartmut Häffner, Wolfgang Hänsel, CF Roos, Jan Benhelm, D Chek-al Kar, M Chwalla, T Körber, UD Rapol, M Riebe, PO Schmidt, et al. Scalable multiparticle entanglement of trapped ions. *Nature*, 438(7068):643–646, 2005.

[177] Stephan Humeniuk. Quantum state tomography on a plaquette in the two-dimensional hubbard model. *Physical Review B*, 100(11):115121, 2019.

[178] Stephan Humeniuk and Yuan Wan. Numerically exact mimicking of quantum gas microscopy for interacting lattice fermions. *Physical Review B*, 104(7):075155, 2021.

[179] Alfréd Rényi. On measures of entropy and information. In *Proceedings of the Fourth Berkeley Symposium on Mathematical Statistics and Probability, Volume 1: Contributions to the Theory of Statistics*, volume 4, pages 547–562. University of California Press, 1961.

[180] AJ Daley, H Pichler, J Schachenmayer, and P Zoller. Measuring entanglement growth in quench dynamics of bosons in an optical lattice. *Physical review letters*, 109(2):020505, 2012.

[181] Rajibul Islam, Ruichao Ma, Philipp M Preiss, M Eric Tai, Alexander Lukin, Matthew Rispoli, and Markus Greiner. Measuring entanglement entropy in a quantum many-body system. *Nature*, 528(7580):77–83, 2015.

[182] Adam M Kaufman, M Eric Tai, Alexander Lukin, Matthew Rispoli, Robert Schittko, Philipp M Preiss, and Markus Greiner. Quantum thermalization through entanglement in an isolated many-body system. *Science*, 353(6301):794–800, 2016.

[183] Alexander Lukin, Matthew Rispoli, Robert Schittko, M Eric Tai, Adam M Kaufman, Soonwon Choi, Vedika Khemani, Julian Léonard, and Markus Greiner. Probing entanglement in a many-body–localized system. *Science*, 364(6437):256–260, 2019.

[184] Matthew B Hastings, Iván González, Ann B Kallin, and Roger G Melko. Measuring renyi entanglement entropy in quantum monte carlo simulations. *Physical review letters*, 104(15):157201, 2010.

[185] Stephan Humeniuk and Tommaso Roscilde. Quantum monte carlo calculation of entanglement rényi entropies for generic quantum systems. *Physical Review B*, 86 (23):235116, 2012.

[186] Noah Linden, Milán Mosonyi, and Andreas Winter. The structure of rényi entropic inequalities. *Proceedings of the Royal Society A: Mathematical, Physical and Engineering Sciences*, 469(2158):20120737, 2013.

[187] Wim Van Dam and Patrick Hayden. Renyi-entropic bounds on quantum communication. *arXiv preprint quant-ph/0204093*, 2002.

[188] Guifré Vidal. Efficient classical simulation of slightly entangled quantum computations. *Physical review letters*, 91(14):147902, 2003.

[189] L Campos Venuti, SM Giampaolo, F Illuminati, and P Zanardi. Long-distance entanglement and quantum teleportation in x x spin chains. *Physical Review A*, 76 (5):052328, 2007.

[190] Norman Ying Yao, Liang Jiang, Alexey Vyacheslavovich Gorshkov, Z-X Gong, Alex Zhai, L-M Duan, and Mikhail D Lukin. Robust quantum state transfer in random unpolarized spin chains. *Physical Review Letters*, 106(4):040505, 2011.

[191] RG Melko, CM Herdman, Dmitri Iouchtchenko, P-N Roy, and Adrian Del Maestro. Entangling qubit registers via many-body states of ultracold atoms. *Physical Review A*, 93(4):042336, 2016.

[192] Howard M Wiseman, Stephen D Bartlett, and John A Vaccaro. Ferreting out the fluffy bunnies: Entanglement constrained by generalized superselection rules. In *Laser Spectroscopy*, pages 307–314. World Scientific, 2004.

[193] Hatem Barghathi, Emanuel Casiano-Diaz, and Adrian Del Maestro. Operationally accessible entanglement of one-dimensional spinless fermions. *Physical Review A*, 100(2):022324, 2019.

[194] Sara Murciano, Giuseppe Di Giulio, and Pasquale Calabrese. Entanglement and symmetry resolution in two dimensional free quantum field theories. *Journal of High Energy Physics*, 2020(8):1–42, 2020.

[195] Tarun Grover. Entanglement of interacting fermions in quantum monte carlo calculations. *Phys. Rev. Letters*, 111(13), 2013.

[196] Lov K Grover. A fast quantum mechanical algorithm for database search. In *Proceedings of the twenty-eighth annual ACM symposium on Theory of computing*, pages 212–219, 1996.

[197] FF Assaad and HG Evertz. World-line and determinantal quantum monte carlo methods for spins, phonons and electrons. In *Computational Many-Particle Physics*, pages 277–356. Springer, 2008.

[198] Ingo Peschel, Matthias Kaulke, and Örs Legeza. Density-matrix spectra for integrable models. *Annalen der Physik*, 511(2):153–164, 1999.

[199] Ingo Peschel and Ming-Chiang Chung. Density matrices for a chain of oscillators. *Journal of Physics A: Mathematical and General*, 32(48):8419, 1999.

[200] Ming-Chiang Chung and Ingo Peschel. Density-matrix spectra of solvable fermionic systems. *Physical Review B*, 64(6):064412, 2001.

[201] Siew-Ann Cheong and Christopher L Henley. Many-body density matrices for free fermions. *Physical Review B*, 69(7):075111, 2004.

[202] Ingo Peschel. Calculation of reduced density matrices from correlation functions. *Journal of Physics A: Mathematical and General*, 36(14):L205, 2003.

[203] Fakher F Assaad, Thomas C Lang, and Francesco Parisen Toldin. Entanglement spectra of interacting fermions in quantum monte carlo simulations. *Physical Review B*, 89(12):125121, 2014.

[204] Lei Wang and Matthias Troyer. Renyi entanglement entropy of interacting fermions calculated using the continuous-time quantum monte carlo method. *Physical Review Letters*, 113(11):110401, 2014.

[205] Joaquín E Drut and William J Porter. Hybrid monte carlo approach to the entanglement entropy of interacting fermions. *Physical Review B*, 92(12):125126, 2015.

[206] Jonathan d'Emidio, Roman Orus, Nicolas Laflorencie, and Fernando De Juan. Universal features of entanglement entropy in the honeycomb hubbard model. *arXiv preprint arXiv:2211.04334*, 2022.

[207] Bradley Efron. *The jackknife, the bootstrap and other resampling plans*. SIAM, 1982.

[208] Michael Golor, Timo Reckling, Laura Classen, Michael M Scherer, and Stefan Wessel. Ground-state phase diagram of the half-filled bilayer hubbard model. *Physical Review B*, 90(19):195131, 2014.

[209] AJ Millis and H Monien. Spin gaps and spin dynamics in la 2- x sr x cu o 4 and y ba 2 cu 3 o 7- δ. *Physical review letters*, 70(18):2810, 1993.

[210] Ling Wang, KSD Beach, and Anders W Sandvik. High-precision finite-size scaling analysis of the quantum-critical point of s= 1/ 2 heisenberg antiferromagnetic bilayers. *Physical Review B*, 73(1):014431, 2006.

[211] Wu-Pei Su, John Robert Schrieffer, and Alan J Heeger. Solitons in polyacetylene. *Physical review letters*, 42(25):1698, 1979.

[212] Oliver Gröning, Shiyong Wang, Xuelin Yao, Carlo A Pignedoli, Gabriela Borin Barin, Colin Daniels, Andrew Cupo, Vincent Meunier, Xinliang Feng, Akimitsu Narita, et al. Engineering of robust topological quantum phases in graphene nanoribbons. *Nature*, 560(7717):209–213, 2018.

[213] Xueda Wen, Shunji Matsuura, and Shinsei Ryu. Edge theory approach to topological entanglement entropy, mutual information, and entanglement negativity in chern-simons theories. *Physical Review B*, 93(24):245140, 2016.

[214] Da Wang, Shenglong Xu, Yu Wang, and Congjun Wu. Detecting edge degeneracy in interacting topological insulators through entanglement entropy. *Physical Review B*, 91(11):115118, 2015.

[215] Mark Srednicki. Entropy and area. *Physical Review Letters*, 71(5):666, 1993.

[216] Helmut Schmidt. Eine einfache herleitung der verteilungsfunktionen für bose-und fermi-statistik. *Zeitschrift für Physik*, 134(4):430–431, 1953.

[217] A. Uhlmann. The "transition probability" in the state space of a $*$-algebra. *Rep. Math. Phys.*, 9(2):273–279, 1976.

[218] Richard Jozsa. Fidelity for Mixed Quantum States. *J. Mod. Opt.*, 41(12):2315, 1994.